J.A.M. Sondag-Huethorst

Electrochemical and Structural Characterization
of Self-Assembled Thiol Monolayers on Gold

STELLINGEN

behorende bij het proefschrift

Electrochemical and Structural Characterization
of Self–Assembled Thiol Monolayers on Gold

door

J.A.M. Sondag–Huethorst

-1-

De depressies in thiolmonolagen op goud die worden waargenomen met STM zijn gaten in het onderliggende goud gevuld met geordende thiolmoleculen.

Edinger, K.; Gölzhäuser, A.; Demota, K.; Wöll, CH.; Grunze, M *Langmuir* **1993**, *9*, 4–8.
Schönenberger, C.; Sondag–Huethorst, J.A.M.; Jorritsma, J.; Fokkink, L.G.J. *Langmuir* **1994**, *10*, 611–614.
Dit proefschrift, hoofdstuk 3.

-2-

Uit het feit dat bij AFM–metingen aan thiolmonolagen op goud altijd dezelfde hexagonale struktuur valt waar te nemen, onafhankelijk van de diameter van het molecuul en de struktuur van het onderliggende goud, valt te betwijfelen of AFM een geschikte methode is om de struktuur van een monolaag te bestuderen.

E.U. Thoden van Velzen, proefschrift TUT 1994
Butt, H.J.; Seifert, K.; Bamberg, E. *J. Phys. Chem.* **1993**, *97*, 7316–7320.

-3-

Ondanks het feit dat in de begin jaren 80 al is aangetoond dat schoon goud hydrofiel is, zijn er nog steeds mensen die beweren dat goud hydrofoob is.

Murphy, O.J.; Wainright, J.S. *Langmuir* **1989**, *5*, 519–523.
Delamarche, E.; Michel, B.; Kang, H.; Gerber, Ch. submitted to Langmuir 1994.

-4-

Galvanische metaalafzetting op thiol–bedekte goudelektroden is een gevoelige en eenvoudige methode om de kwaliteit van de monolaag te testen.

Dit proefschrift, hoofdstuk 8

-5-

Het gebruik van di–joodmethaan en 1–broomnaftaleen voor de bepaling van de dispersieve component van de oppervlakte vrije energie van vast stoffen is niet zinvol.

Good, R.J. *J. Adhesion Sci. Technol.* **1992**, *6*, 1269–1302.

-6-

Het met grote zelfverzekerdheid publiceren van ondermaatse karakteristieken van lithium–polymeer batterijen resulteert nog niet in een batterij die geschikt is voor de consumentenmarkt.

Croce, F.; Passerini, S.; Scrosati, B. *J. Electrochem. Soc.* **1994**, *141*, 1405–1408.
Passerini, S.; Loutzky, S.; Scrosati, B. *J. Electrochem. Soc.* **1994**, *141*, L80–L81.

-7-

Naast de moderne baby is de moderne promovendus een grootverbruiker van papier.

-8-

Om de objektiviteit van een "reviewer" van een manuscript te waarborgen is het verstandig om de naam van de auteur van het artikel weg te laten.

-9-

Boerenverstand komt ook in de fysische chemie van pas.

-10-

De enige drijfveer voor de industrie om spontaan iets aan milieuaktiviteiten te doen is een economische.

-11-

Het feit dat de Nederlandse radio een handtekeningenaktie organiseert tegen racisme en nationalisme in Duitsland, doet een onderschatting van deze verschijnselen in Nederland vermoeden.

-12-

Het aantal files neemt niet af door het aanleggen van meer wegen.

Aan Fons
Aan mijn ouders

Table of Contents

List of symbols

Symbol	Description	Unit
C_d	Electrical double layer capacitance	F m^{-2}
C_i	Capacitance of thiol layer	F m^{-2}
C_t	Overall differential capacitance	F m^{-2}
C_X	C_t of thiol layer with terminal group X	F m^{-2}
d	Thickness of Wilhelmy plate working electrode	m
E	Electrode potential	V
E_e	Potential at electrocapillary maximum	V
F	Force acting on Wilhelmy plate	N
F_d	Helmholtz energy	J m^{-2}
g	Standard acceleration of free fall	m s^{-2}
h	Height of Wilhelmy plate working electrode	m
I	Current density	A m^{-2}
I_t	STM tunnel current	A
l	Length of Wilhelmy plate working electrode	m
k	Boltzmann constant	
Δm	Change in mass associated with meniscus rise	kg
m_{Au}	Amount gold in thiol solution after adsorption	kg
n_j^0	Numbers of ions of type j per volume	m^{-3}
n	Number of carbon atoms of a thiol molecule	
Q	Charge transferred during oxidation/reduction	C m^{-2}
Q_d	Charge density involved in metal deposition	C m^{-2}
Q_s	Charge density involved in metal stripping	C m^{-2}
R_t	STM tunnel resistance	Ω
t	Immersion time of gold in thiol solution	min
T	Temperature	K
V_b	STM tip potential	V
x_{Fc}	Fraction ferrocenethiol in thiol solution	
X	Terminal group of the alkanethiol molecule	
z	Valence number	

z_0	Depth of immersion of Wilhelmy plate in liquid	m
Γ_{Fc}	Number of adsorbed ferrocenethiol molecules	m^{-2}
$\gamma_{12}, \gamma_{23}, \gamma_{13}$	Interfacial tension of the 1/2, 2/3, 1/3 interface	$N\ m^{-1}$
γ_{LV}	Liquid/Vapour interfacial tension	$N\ m^{-1}$
γ_{SL}	Solid/Liquid interfacial tension	$N\ m^{-1}$
$\gamma_{SL}^{\ el}$	Electrostatic contribution to γ_{SL}	$N\ m^{-1}$
$\gamma_{SL}^{\ 0}$	Chemical contribution to γ_{SL}	$N\ m^{-1}$
γ_{SV}	Solid/Vapour interfacial tension	$N\ m^{-1}$
δ	Thickness of thiol layer	m
ε_0	Dielectric permittivity of vacuum	$Cm^{-1}\ V^{-1}$
ε_r	Relative dielectric constant	
η	Overpotential with respect to Nerst potential	V
$\eta_d^{\ c}$	Overpotential at thiol/electrolyte interface necessary for galvanic metal deposition	V
θ	Contact angle	deg
θ_a	Advancing contact angle measured with water	deg
θ_r	Receding contact angle measured with water	deg
$\theta_a^{\ HD}$	Advancing contact angle measured with hexadecane	deg
$\theta_a^{\ ox}, \theta_a^{\ red}$	θ_a of oxidized or reduced ferrocene thiol, respectively	deg
$\theta_r^{\ ox}, \theta_r^{\ red}$	θ_r of oxidized or reduced ferrocene thiol, respectively	deg
μ_i	Chemical potential of species i	$J\ mol^{-1}$
ρ	Density	$kg\ m^{-3}$
σ_0	Surface charge density	$C\ m^{-2}$
σ_d	Charge density in diffuse double layer	$C\ m^{-2}$
ψ_0	Electric potential at gold/thiol interface	V
ψ_d	Electric potential at thiol/electrolyte interface	V
ϑ	Frequency	Hz

Chapter 1

Introduction

1.1. General introduction

Electrochemistry is widely used in many areas of technology. Typical examples in daily life are big batteries for starting one's car or small ones for portable radios. Rusting is a result of electrochemical processes. Steel of lampposts and crash barriers is often protected from corrosion by a zinc coating. This protection is also based on an electrochemical mechanism: the iron can be saved by sacrificing the less noble metal zinc. Clothing may be made of nylon, a substance produced by an electrochemical process.

The interest of the electronic industry in electrochemistry concentrates mainly on metal deposition and etching processes. In the case of metal deposition, usually flat and homogeneous films or patterns are required. Hence, understanding of the factors governing the morphology (i.e., the structure) of the deposit is very important. One of these factors may be the surface properties of the substrate. In this thesis we systematically study the influence of the surface tension of the substrate on the morphology of galvanically deposited metal.

A measure of the surface tension is the degree to which the surface is wetted by a liquid. This degree of wetting is termed the wettability. A surface is completely wetted by water if the surface tension is high enough. Then water will cover the surface and form a thin homogeneous film. Such a surface is called hydrophilic. Low surface tensions result in a poor wettability by water. On substrates with a low surface tension, also called hydrophobic, the water forms drops.

Similar with liquids, the surface tension of the substrate also influences the morphology of galvanically deposited metal: both flat and homogeneous metal

films or metal "drops" can be formed. Galvanic metal deposition onto a substrate is only possible if that substrate is a conductor. In order to test the influence of the surface tension on the morphology of the metal deposit, conducting substrates with a variety of surface tensions are required. The choice of suitable substrates is not very wide: the surface tension of most metal substrates is very high. Substrates with lower surface tensions, like various plastics, are not suitable because they are non–conducting and can therefore not be used in galvanic deposition studies.

In this thesis we use a metal surface to have a conducting material, but we apply an organic coating to lower the surface tension. We chose gold electrodes modified with a film of alkanethiol molecules. These molecules contain a sulphur group that forms a chemical bond with gold. In order to be more flexible, we used functionalized alkanethiols. Their molecular formula is $HS(CH_2)_{n-1}X$. The number of carbon atoms and the type of terminal group X of the molecule can be varied. Such molecules form spontaneously an ordered and densely packed monomolecular layer or, for short, a monolayer on gold. This spontaneous process of ordering is called self-assembly. By covering the gold with a monolayer, the "face" of the electrode changes from metallic to plastic. This layer is thin enough to transport electrons through the organic layer, yet it is thick enough to form an inert and stable layer. By variation of the terminal group X the surface tension of the substrate can be changed and the influence of the surface tension on the morphology of the metal deposit can be studied systematically. By manipulating the surface in this way, we open up a new area of interfacial electrochemistry.

As a basis for the electrodeposition study, we first investigated the influence of the state of electrification of thiol-modified gold on its wettability by an electrolyte solution. This may be called potential-dependent wetting or electrowetting. So far, most electrowetting studies focused on mercury [1]. This (liquid) metal is hydrophobic. Most of the other (solid) metals do not exhibit such electrowettability because they are hydrophilic. Changing the potential will then not result in a measurable change in wettability; the substrate remains hydrophilic. By applying a monolayer of thiol molecules, gold becomes

hydrophobic and the electrowetting effect, so far primarily observed with liquid mercury, becomes relevant for a solid metal.

In order to successfully use these thiol monolayers in controlled electrochemical studies, the molecular structure of the layer should be known. In this work, we show that Scanning Tunneling Microscopy (STM) can, under certain experimental conditions, provide a rather complete molecular (i.e., microscopic) picture of thiol monolayers adsorbed on gold. Additional information on the monolayer on a more macroscopic scale is obtained from electrochemical measurements, like cyclovoltammetry and capacitance measurements.

Before discussing in detail the outline of this thesis, an overview of the literature on (thiol) monolayers will be given. Hereby we use the title of this thesis *"electrochemical and structural characterization of self-assembled thiol monolayers on gold"* as a guide line. First, an overview of the development of the research on *self-assembled monolayers* is presented, followed by the *structural characteristics of self-assembled thiol monolayers on gold*. Subsequently, the state of the art of the *electrochemistry* of such monolayers is discussed. In the final section of this introduction the outline and aim of this thesis are given.

1.2. Self-assembled monolayers

Self-assembled monolayers are molecular assemblies that are formed spontaneously by immersion of an appropriate substrate into a solution of an active surfactant in a solvent [2,3]. There are two important requirements to obtain a self-assembled monolayer. First, the headgroups of the molecules should form a strong chemical bond with the substrate. Second, the lateral van der Waals interactions between the alkyl chains should be high enough to overcome the free energy loss due to a reduced entropy.

About 50 years ago, self-assembled monolayers were introduced in a paper by

Bigelow et al. [4]. These authors showed that a carboxylic acid dissolved in a non–polar solvent adsorbs onto a hydrophilic surface immersed in this solvent. When this surface is withdrawn from the solvent, it retains an adsorbed and ordered layer. In the last two decades many other self-assembling systems have been studied. These include carboxylic acids on oxidized metal surfaces and glass [5–8], organosilicon compounds on hydroxylated surfaces such as glass, quartz, aluminium and silicon [9–12], phosphonates on metallic surfaces [13], isonitriles on platinum [14], and thiols and disulfides on metal or semiconductor surfaces, like gold, silver, copper, and GaAs [15–20]. The common characteristic of all these layers is that the molecules form a chemical bond with the substrate. This may be a covalent Si–O or Au–S bond for alkyltrichlorosilanes on silicon oxide surfaces or thiols on gold, respectively, or an ionic $CO_2^-Ag^+$ bond in the case of carboxylic acids on silver. In order to obtain an ordered and stable monolayer the alkyl chains should be sufficiently long. It was found that both for carboxylic acids on aluminum [7] and for alkanethiol on gold [16,17] a chain containing more than about 10–12 carbon atoms is required.

1.2.1. Thiol monolayers on gold

Alkanethiol ($HS(CH_2)_{n-1}CH_3$) monolayers on gold are among the most popular self–assembling monolayers. Such monolayers can also be formed on other metal or semiconductor substrates, like Ag, Hg, W and GaAs [18–21]. On gold, a covalent Au–S bond is formed. Various methods like ellipsometry, infrared spectroscopy, X–ray photoelectron spectroscopy, electron and helium scattering, contact angle measurements, STM, and electrochemical methods have been used to study self-assembled monolayers. It has been established that long enough alkanethiol molecules on Au(111) form densely packed, crystalline–like assemblies with fully extended alkyl chains, which are tilted from the surface normal by about 30° [16,22]. A schematic representation of such a monolayer is given in Figure 1.1. Self-assembly occurs when the number n of carbon atoms in the alkane chain becomes larger than about 10-12 [16,17]. Due to the strong sulphur–gold interaction, the structure of the monolayer is not affected when the
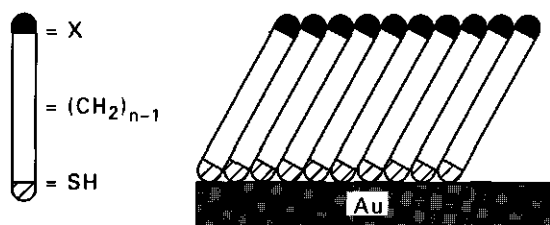
Figure 1.1: Schematic representation of a self-assembled thiol monolayer on gold.

alkanethiol molecules are substituted with a terminal group X, as long as this group is not larger than the cross-sectional area of the alkane tail [23]. By changing the terminal group the surface properties of the thiol-modified gold can thus be varied. The terminal group may even be electrochemically active (or, for short, "electroactive") so that it is possible to reduce or oxidize it without affecting the structure of the thiol layer [24].

A variety of techniques such as helium diffraction [25], electron and X–ray diffraction [26,27] and STM [28] have been used to determine the structure of the monolayer. The sulphur head groups of the molecules were found to bind to the Au(111) surface in a structure commensurate with the Au(111) structure. The sulphur moieties rest in the threefold hollow sites of the Au(111) [27,29] (see Figure 1.2). The nearest-neighbour distance between the sulphur atoms is 0.5 nm, corresponding to a surface density of 4.6 10^{14} molecules cm^{-2}.

Employing thiol monolayers as model systems in electrowetting and electrodeposition studies requires that these layers are not permeable to electrolyte though electrons should be able to penetrate. Hence, the number of defects in the monolayer should be largely reduced. Several factors influence the structure and quality of thiol monolayers on gold. These factors are, for example, the preparation of the gold substrate [30–35], the type of solvent from which the thiol is deposited [17,36,37], and annealing of the modified gold electrode after deposition [30,38,39].
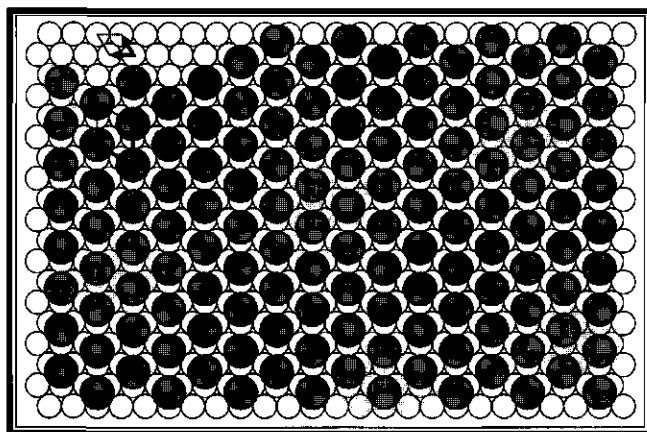
Figure 1.2: Coverage scheme for alkanethiols on Au(111). Small circles represent Au surface atoms and the larger dark ones chemisorbed sulphur head-groups of thiol molecules.

1.2.2. Electrochemistry of self-assembled thiol monolayers on gold

Electrochemistry is often used as a characterization technique to obtain information about the quality of thiol monolayers. When defects, like small holes in the monolayer ("pinholes") or disordered areas of molecules, are present, water or ions may penetrate into the monolayer. In such cases, electrochemical reactions will take place at the gold/thiol interface. By using redox couples (like Fe^{2+}/Fe^{3+}) in solution, it has been checked whether or not the monolayer is densely packed and prevents ion penetration [16,40–46]. If penetration is blocked, electrochemical reactions can only take place at the thiol/electrolyte interface. Because electron transport through the aliphatic monolayer is strongly hindered, the electrochemical reactions will also be strongly reduced. Hence, the rate of charge transfer is a measure for quality of the monolayer. Therefore, redox couples can be used to determine the order/disorder transition of self-assembled monolayers [16]. It was found that for about $n>10$ the reduction current strongly decreased. Monolayers of shorter chains are disordered. This has been corroborated by other types of measurements.

Besides the electrochemistry of the redox couples, also oxidation of gold has been used for determining the passivating properties of the monolayer [40,41]. When water penetrates the monolayer and contacts the gold, the gold may be oxidized to give gold–oxide at the gold/thiol interface. Although this method is able to give information about the penetration of water, it is not very suitable to determine the exact number of defects, because the thiol layer becomes highly unstable upon oxidation. Due to the formation of gold–oxide, the monolayer may be disrupted.

Not only the penetration of ions, but also the transport of electrons through the monolayer is of fundamental interest. For monolayer films free of defects, the electron transport through the thiol layers has to occur by electron tunneling or hopping through the monolayer film. Miller et al. [43] suggested that for hydroxy thiol monolayers of varying chain lengths electron tunneling occurs. A problem with the interpretation of this type of studies is that rapid electron transport at a few defect sites can hardly be ruled out. By replacing the redox couples in the electrolyte by covalently attached electroactive groups [24,47–50], this problem is overcome: the electroactive groups can only exchange electrons with the electrode across the monolayer. For this purpose, mainly ferrocene(Fc)-terminated alkanethiol monolayers on gold have been applied [24,48]. Even for relatively long–chain ferrocenethiols, like Fc–terminated hexadecanethiol, it was found that the Fc group can be oxidized and reduced [50]. For such thick thiol layers electron tunneling is not likely to occur [43]. Hence, some other mechanism must be responsible for the transport of the electrons through the alkyl chain.

Both ion penetration and electron transport through the thiol layer are of interest in model studies of biological membranes [45]. An example of these studies are synthetic layers of acidic phospholipids in aqueous solutions, investigated intensively in relationship to their membrane functions [51]. When these molecules contain a thiol group they can form self-assembled monolayers.

Electrochemical methods have also been used to determine the concentration of molecules at the surface by reductive desorption of the molecules [52,53]. In an

alkaline solution (pH>11) the gold–thiolate bond (Au–SR) can be reduced by the one–electron reaction $AuSR + e^- \rightleftharpoons Au(0) + {}^-SR$. From measuring the charge involved in this reaction, the thiol surface concentration can thus be derived.

1.3. Outline of this thesis

1.3.1. Aim

The principal aim of this thesis is to explore the possibility of applying "classical" electrochemical methods, like galvanic metal deposition and potential-dependent wetting, to a "new" (model) system: thiol monolayers on gold. The purpose of the electrodeposition study is to investigate the influence of the surface tension on the morphology of galvanically deposited metal. The surface tension can be easily changed by varying the terminal group of the monolayer. In addition, electrodeposition provides information about the presence of (microscopic) defects in the thiol monolayers.

Most of the classical electrowetting studies have been done on mercury. We apply electrowetting to self-assembled monolayers on gold. An intriguing aspect is to explore whether the electrowetting effects of the monolayer system can be described by traditional interfacial thermodynamics. From the thermodynamical description of this system the background of the electrowetting phenomena on both electroinactive and electroactive thiol monolayers can be better understood.

There are two requirements for the use of thiol monolayers as model system in electrochemical studies. First, the monolayers should be densely packed and defect–free, and second, electron transport through the alkyl chains must be possible. If this is the case, the electrochemical processes take place at the thiol/electrolyte interface and the influence of this interface on electrodeposition or electrowetting can be studied. To check whether or not the thiol monolayers are free of defects, we investigated the characteristics of the monolayers both on a macroscopic and microscopic scale. For the macroscopic characterization we

used cyclovoltammetry, differential capacitance measurements and contact angle measurements. For the microscopic characterization we employed atomically resolved STM measurements in air. By combining the results of these measurements we intend to find an answer to the question: are thiol monolayers suitable model systems?

1.3.2. Outline of the subsequent chapters

This thesis is organized as follows. Chapter 2 deals with most of the experimental techniques and materials used in chapters 3 to 9. First, the synthesis of the thiols that are not commercially available is given. Second, the preparation of the thiol monolayers on gold and the characterization of these monolayers with sessile drop measurements is described. The purpose of this separate experimental chapter is to prevent overlap between the individual chapters. Detailed information about the experiments are given in separate sections in the individual chapters.

Chapter 3 deals with the microscopic structure of alkanethiol monolayers on gold(111) in air as studied by STM with atomic scale. This technique revealed the nature of the mysterious "holes" in thiol layers as observed in previous STM studies. The holes appeared to be holes in the underlying gold resulting from an etching process during adsorption. This was confirmed by analysis of the thiol solution after adsorption with atomic absorption spectroscopy: small amounts of gold could be determined.

The technique used for measuring the potential-dependent wetting of alkanethiol monolayers on polycrystalline gold is presented in chapter 4. These measurements were carried out simultaneously with cyclovoltammetry and differential capacitance measurements. The (electrochemical) characteristics of bare and thiol-modified gold are compared. In chapter 5 the influence of the thiol chain length and electrolyte concentration on the potential-dependent wetting of alkanethiol-modified gold electrodes is investigated. The relationship

between the potential and the change in wettability could conveniently be described by interfacial thermodynamics. It is shown that the electrowetting effect is mainly caused by the formation of an electrical double layer. The same type of measurements were carried out for functionalized alkanethiol monolayers. These measurements are discussed in chapter 6. The (functionalized) alkanethiol monolayers appeared to be stable when applying an electric field across the thiol layer, independent of the thiol chain length (for $n>10$) and terminal group.

Electrowetting based on oxidation/reduction of the terminal group of a thiol monolayer on gold is described in chapter 7. For this purpose, gold was modified by an electroactive ferrocene-terminated alkanethiol monolayer. Compared to the electroinactive alkanethiol monolayers, the electrowetting effects obtained with ferrocene-terminated monolayers were reversible and much larger. The effect of mixing this ferrocene thiol with simple alkanethiols on the stability of the monolayer and the magnitude of the electrowetting phenomenon is studied.

Galvanic copper deposition on top of the thiol monolayers is the subject of study in chapter 8. The influence of the terminal group of a functionalized alkanethiol monolayer and of the chain length of an alkanethiol monolayer on the morphology is investigated. The morphology of the deposits is imaged with scanning electron microscopy. It appeared that the copper could be deposited on top of the thiol layer. It was deposited as hemispherical particles. The mechanism involved in electron transport through the thiol layer is discussed.

Chapter 9 presents an application of thiol monolayers in nanolithography. In this chapter the thiol monolayers were used as a resist. The resist is selectively removed with an *e*–beam and subsequently, copper is galvanically deposited in the openings in the resist layer.

Finally, in chapter 10 the results of the STM and the electrowetting measurements are compared with the current status of knowledge in the literature. Subsequently, results on the structure of the thiol monolayers obtained in the separate chapters are compared and discussed. Finally suggestions for

further study are made.

References

[1]   Lippmann, G. *Ann. Chim. Phys.* **1875**, *5*, 494.
[2]   For general review see: Ulman, A. *An Introduction to Ultrathin Organic Films from Langmuir–Blodgett to Self–assembly*; Academic Press Inc., San Diego, 1991.
[3]   For general review see: Tredgold, R.H. *Order in Thin Organic Films*; Cambridge University Press, 1994.
[4]   Bigelow, W.C.; Pickett, D.L.; Zisman, W.A. *J. Colloid Interface Sci.* **1946**, *1*, 513–518.
[5]   Sondag, A.H.M.; Raas, M.C. *J. Phys. Chem.* **1989**, *91*, 4926–4931.
[6]   Gun, J.; Iscovici, R.; Sagiv, J. *J. Colloid Interface Sci.* **1984**, *101*, 201–213.
[7]   Allara, D.L.; Nuzzo, R.G. *Langmuir* **1985**, *1*, 52–66.
[8]   Schlotter, N.E.; Porter, M.D.; Bright, T.B.; Allara, D.L. *Chem. Phys. Lett.* **1986**, *132*, 93–98.
[9]   Sagiv, J. *J. Am. Chem. Soc.* **1980**, *102*, 92–98.
[10]   Maoz, R.; Sagiv, J. *J. Colloid Interface Sci.* **1984**, *100*, 465–496.
[11]   Tillman, N.; Ulman, A.; Schildkraut, J.S.; Penner, T.L. *J. Am. Chem. Soc.* **1988**, *110*, 6136–6144.
[12]   Wasserman, S.R.; Whitesides, G.M.; Tidswell, I.M.; Ocko, B.M.; Pershan, P.S.; Axe, J.D. *J. Am. Chem. Soc.* **1989**, *111*, 5852–5861.
[13]   Lee, H.; Kepley, L.J.; Hong, H.–G.; Akhter, S.; Mallouk, T.E. *J. Phys. Chem.* **1988**, *92*, 2597–2601.
[14]   Hickman, J.J.; Zou, C.; Ofer, D.; Harvey, P.D.; Wrighton, M.S.; Laibinis; P.E.; Bain, C.D.; Whitesides, G.M. *J. Am. Chem. Soc.* **1989**, *111*, 7271–7272.
[15]   Nuzzo, R.G.; Allara, D.L. *J. Am. Chem. Soc.* **1983**, *105*, 4481–4483.
[16]   Porter, M.D.; Bright, T.B.; Allara, D.L.; Chidsey, C.E.D. *J. Am. Chem. Soc.* **1987**, *109*, 3559–3568.
[17]   Bain, C.D.; Throughton, E.B.; Tao, Y.–T.; Evall, J.; Whitesides, G.M.; Nuzzo, R.G. *J. Am. Chem. Soc.* **1989**, *111*, 321–335.
[18]   Mullins, D.R.; Lyman, P.F. *J. Phys. Chem.* **1993**, *97*, 9226–9232.
[19]   Laibinis, P.E.; Whitesides, G.M.; Allara, D.L.; Tao, Y.–T.; Parikh, A.N.; Nuzzo, R.G. *J. Am. Chem. Soc.* **1991**, *113*, 7152–7167.
[20]   Sheen, C.W.; Shi, J.–X.; Mårtensson, J.; Parikh, A.N.; Allara, D.L. *J. Am. Chem. Soc.* **1992**, *114*, 1514–1515.
[21]   Matsushita, F.; Miyaoka, S.; Ikeda, T.; Senda, M. *Anal. Sci.* **1991**, *7*, 1685–1688.
[22]   Nuzzo, R.G.; Korenic, E.M.; Dubois, L.H. *J. Chem. Phys.* **1990**, *93*, 767–778.
[23]   Chidsey, C.E.D.; Loiacono, D.N. *Langmuir* **1990**, *6*, 682–691.

[24]   Chidsey, C.E.D.; Bertozzi, C.R.; Putvinski, T.M.; Mujsce, A.M. *J. Am. Chem. Soc.* **1990**, *112*, 4301–4306.

[25]   Camillone III, N.; Chidsey, C.E.D.; Liu, G.-Y.; Scoles, G. *J. Chem. Phys.* **1993**, 98, 3503–3511.

[26]   Nuzzo, R.G.; Zegarski, B.R.; Dubois, L.H. *J. Am. Chem. Soc.* **1987**, *109*, 733–740.

[27]   Chidsey, C.E.D.; Loiacono, D.N. *Langmuir* **1990**, *6*, 682–691.

[28]   Alves, C.A.; Smith, E.L.; Widrig, C.A.; Porter, M.D. *SPIE Appl. Spectr. Mat. Sci. II* **1992**, *1636*, 125–128.

[29]   Strong, L.; Whitesides, G.M. *Langmuir* **1988**, *4*, 546–558.

[30]   Delamarche, E.; Michel, B.; Kang, H.; Gerber, Ch. submitted *Langmuir* (1994).

[31]   Smith, T. *J. Colloid Interface Sci.* **1980**, *75*, 51–55.

[32]   Schneegans, M.; Menzel, E. *J. Colloid Interface Sci.* **1982**, *88*, 97–99.

[33]   *Handbook of Chemistry and Physics (71st ed.)*; Lide, D.R., Ed., CRC Press, 1990.

[34]   Reference [2], page 109.

[35]   Creager, S.E.; Hockett, L.A.; Rowe, G.K. *Langmuir* **1992**, *8*, 854–861.

[36]   Ulman, A.; Evans, S.D.; Shnidman, Y.; Sharma, R.; Eilers, J.E.; Chang, J.C. *J. Am. Chem. Soc.* **1991**, *113*, 1499–1506.

[37]   Offord, D.A.; John, C.M.; Linford, M.R.; Griffin, J.H. *Langmuir* **1994**, *10*, 883–889.

[38]   Bucher, J.P.; Santesson, L.; Kern, K. *Langmuir* **1994**, *10*, 979–983.

[39]   McCarley, R.L.; Dunaway, D.J.; Willicut, R.J. *Langmuir* **1993**, *9*, 2775–2777.

[40]   Bilewicz, R.; Majda, M. *Langmuir* **1991**, *7*, 2794–2802.

[41]   Sabatini, E.; Cohen–Boulakia, J.; Bruening, M.; Rubinstein, I. *Langmuir* **1993**, *9*, 2974–2981.

[42]   Finklea, H.O.; Avery, S.; Lynch, M.; Furtsch, T. *Langmuir* **1987**, *3*, 409–413.

[43]   Miller, C.; Cuendet, D.; Grätzel, M. *J. Phys. Chem.* **1991**, *95*, 877–886.

[44]   Takehara, K.; Takemura, H.; Ide, Y. *Electrochim. Acta* **1994**, *39*, 817–822.

[45]   Takehara, K.; Ide, Y. *J. Electroanal. Chem. Bioelectrochem.* **1992**, *27*, 207–219.

[46]   Thoden van Velzen, E.U. *Ph. D. thesis*, U. Twente (NL), 1994.

[47]   Finklea, H.O.; Hanshew, D.D. *J. Am. Chem. Soc.* **1992**, *114*, 3173–3181.

[48]   Creager, S.E.; Rowe, G.K. *J. Electroanal. Chem.* **1994**, *370*, 203–211.

[49]   Finklea, H.O.; Ravenscroft, M.S.; Snider, D.A. *Langmuir* **1993**, *9*, 223–227.

[50]   Collard, D.M.; Fox, M.A. *Langmuir* **1991**, *7*, 1192–1197.

[51]   Nakahima, N.; Taguchi, T.; Takada, Y.; Fuyo, K.; Kunitake, M.; Manabe, O. *J. Chem. Soc., Chem. Comm.* **1991**, 232–233.

[52]   Widrig, C.A.; Chung, C.; Porter, M.D. *J. Electroanal. Chem.* **1991**, *310*, 335–359.

[53]   Walczak, M.M.; Popenoe, D.D.; Deinhammer, R.S.; Lamp, B.D.; Chung, C.; Porter, M.D. *Langmuir* **1991**, *7*, 2687–2693.

Chapter 2

Materials and experimental methods

Abstract: In this chapter we describe the materials and several methods that are generally used in most of the chapters. The materials and methods that are specific for one chapter are described in a separate experimental section in that chapter.

2.1. Materials

2.1.1. Gold electrodes

Gold electrodes used for the electrowetting measurements were prepared by cutting a polycrystalline gold plate (99.99%) with a thickness of 0.5 mm into pieces of 4.00 cm × 3.00 cm. The pieces were mechanically polished with silver polish (Racket) and then thoroughly rinsed with deionized water and hexane. In order to remove organic contaminants, the electrodes were subsequently treated in a UV/ozone reactor (UVP Inc.; PR-100) for 15 min. Immediately after this treatment, 200 nm of gold (99.999%, Williams Gold Ref.) was evaporated onto both sides of the electrode. The pressure during evaporation in the cryopumped Edwards E306 coating system was less than 9×10^{-5} Pa. After deposition the system was refilled with prepurified argon.

The surface crystallinity of the gold electrodes was investigated by X-ray diffraction (Philips IPD PW1800). It was found that the crystal structure of the gold is predominantly of the types (111), (220), and (311).

2.1.2. Thiols

1–Propanethiol (HS(CH$_2$)$_2$CH$_3$), 1–decanethiol (HS(CH$_2$)$_9$CH$_3$), and 1–dodecanethiol (HS(CH$_2$)$_{11}$CH$_3$) were obtained from Fluka, 1–octanethiol (HS(CH$_2$)$_7$CH$_3$) from Aldrich, and octadecanethiol (HS(CH$_2$)$_{17}$CH$_3$) from Janssen Chimica. These chemicals were used as received. 1–Docosanethiol (HS(CH$_2$)$_{21}$CH$_3$), 11–mercapto-1–undecanol (HS(CH$_2$)$_{11}$OH) and 11–mercaptoundecanoic acid (HS(CH$_2$)$_{10}$COOH) were prepared according to liturature procedures given in references 1, 2 and 3, respectively. 11–Chloro-1–undecanethiol (HS(CH$_2$)$_{11}$Cl) and 12–mercapto-1–dodecanenitrile (HS(CH$_2$)$_{11}$CN) were prepared according to the synthesis given below.

Synthesis of 11–chloro–1–undecanethiol
11–Chloro–1–undecanethiol (HS(CH$_2$)$_{11}$Cl) was prepared in a three–step synthesis from 10–undecen-1–ol by chlorination, photocatalyzed thioacetylation, and base–catalyzed thioester cleavage. The 10–undecen-1–ol (HO(CH$_2$)$_9$CH=CH$_2$) was chlorinated [4] to give 11–chloro-1–undecene (Cl(CH$_2$)$_9$CH=CH$_2$). A solution of this compound (10.0 g, 53 mmole), thiolacetic acid (10.0 g, 132 mmole), and a catalytic amount of AIBN (α,α'–azobis(2–methylpropionitril)) in toluene (200 cm^3) was exposed to unfiltered UV–radiation of a mercury lamp for 6 h. The reaction mixture was washed with a saturated sodium bicarbonate solution (3×) and water (2×). The organic layer was dried over magnesium sulphate and concentrated under reduced pressure. The yellow oil was subjected to column chromatography (SiO$_2$, hexane ethyl acetate 9:1 v/v), yielding 12.57 g (90%) of a yellowish oil (11–chloro-1–undecylthiolacetate, Cl(CH$_2$)$_{11}$SC(O)CH$_3$). ^{1}H NMR (CDCl$_3$) δ_H 3.41 (t, 2H, RCH_2Cl, J = 6.8 Hz), 2.75 (t, 2H, RCH_2SAc, J = 7.0 Hz), 2.21 (s, 3H, RSC(O)CH_3), 1.60–1.71 (m, 2H, ClCH$_2$CH_2R), 1.40–1.51 (m, 2H, RCH_2CH$_2$SAc), 1.17–1.34 (m, 14H, CH_2).

To a solution of 11–chloro-1–undecylthioacetate (0.95 g, 3.6 mmole) in degassed methanol (150 cm^3) potassium carbonate (0.5 g, 3.62 mmole) was added. The suspension was refluxed for 30 min, and subsequently quenched with acetic acid

(1.05 g, 4.37 mmole). The suspension was filtered, and concentrated under reduced pressure. The resulting yellow oil was subjected to flash chromatography (SiO$_2$, hexane dichloromethane 3:1 v/v) and yielded 0.6 g (74%) or a colourless oil (11–chloro-1–undecanethiol, HS(CH$_2$)$_{11}$Cl). ^{1}H NMR (CDCl$_3$) δ_H 3.52 (t, 2H, RCH_2Cl, J = 6.7 Hz), 2.47–2.56 (m, 2H, RCH_2SH), 1.71–1.84 (m, 2H, ClCH$_2$CH_2R), 1.52–1.66 (m, 2H, RCH_2CH$_2$S), 1.00–1.49 (m, 14H, CH_2): Anal Calcd for C$_{11}$H$_{23}$ClS: C, 59.30, H, 10.40; found C, 59.39, H, 10.32.

Synthesis of 12–mercapto–1–dodecanenitrile

12–Mercapto-1–dodecanenitrile (HS(CH$_2$)$_{11}$CN) was prepared in a three–step reaction from 11–chloro-1–undecene by cyanation, addition of thiolacetic acid over the double bond and thioester cleavage. A solution of 11–chloro-1–undecene (8.00 g, 42.5 mmole) and potassium cyanide (3.0 g, 45 mmole) in DMF (200 cm^3) was heated at 60°C for 24 h. The reddish solution was concentrated under pressure, diluted with diethyl ether and washed with water (3×). The organic layer was dried over magnesium sulphate, and concentrated under reduced pressure, yielding 6.7 g (88%) of a yellowish oil (11–dodecenitrile, CN(CH$_2$)$_9$CH=CH$_2$). ^{1}H NMR (CDCl$_3$) δ_H 5.88–5.73 (m, 1H, RCH=CH$_2$), 5.02 and 4.91 (both d, both 1H, RCH=CH_2, J_1 = 17 Hz, J_2 = 10 Hz), 2.74 (t, 1H, RCH_2CN, J = 7.4 Hz), 2.12–2.01 (m, 1H, RCH_2CH=CH$_2$), 1.69–1.85 (m, 1H, RCH_2CH$_2$CN), 1.52–1.24 (m, 7H, CH_2).

A solution of 11–dodecenitrile (5.0 g, 28 mmole), thiolacetic acid (8 g, 106 mmole), and a catalytic amount of AIBN in toluene (200 cm^3) was irradiated with the unfiltered UV–radiation of a mercury lamp for 12 h. The product was washed with a saturated potassium bicarbonate solution (3×). The organic layer was dried over magnesium sulphate, and concentrated under reduced pressure. The yellow oil was subjected to column chromatography (SiO$_2$, hexane ethyl acetate 4:1 v/v), giving 5.7 g (80%) of a yellowish oil (12–thioacetyl-1–dodecanitrile, CN(CH$_2$)$_{11}$SC(O)CH$_3$). ^{1}H NMR (CDCl$_3$) δ_H 2.88 (t, 2H, RCH_2CN, J = 7.5 Hz), 2.37–2.28 (m, 5H, RCH_2SC(O)CH_3), 1.75–1.48 (m, 4H, RCH_2CH$_2$CN and RCH_2CH$_2$SAc), 1.48–1.22 (m, 14H, CH_2).

To a solution of 12–thiolacetyl-1–dodecanitrile (2.5 g, 10 mmole) in degassed

methanol (150 cm^3) potassium carbonate (1.5 g, 11 mmole) was added. The suspension was refluxed for 30 min, and subsequently quenched with acetic acid (0.1 g, 1.6 mmole). The suspension was filtered, and concentrated under pressure. The resulting yellow oil was subjected to flash chromatography (SiO$_2$, hexane dichloromethane 2:1 v/v), yielding 1.7 g (85%) of a colourless oil (12–mercapto-1–dodecanenitrile, HS(CH$_2$)$_{11}$CN). ^{1}H NMR (CDCl$_3$) δ_H 2.63 (t, 1H, RC*H$_2$*CN, J = 7.4 Hz), 2.35 (t, 1H, RC*H$_2$*SH), 1.73–1.56 (m, 2H, RC*H$_2$*CH$_2$CN and RC*H$_2$*CH$_2$SH), 1.50–1.22 (m, 7H, C*H$_2$*).

2.2. Preparation of the monolayers

Prior to adsorption, each gold electrode was treated in the UV/ozone reactor, each side for 15 min, resulting in hydrophilic gold substrates. This treatment was immediately followed by immersion into a freshly prepared solution of 3.5 mM thiol in methanol. Because some of the solid long chain alkanethiols are poorly soluble in methanol, these thiols were first melted at about 35°C just before being added to methanol. The thiol spontaneously adsorbed onto gold. The adsorption time varied between 3 h and a few days. In this time period no differences in quality of the monolayers were observed. After adsorption, the electrode was rinsed in methanol, followed by rinsing in 2–propanol and subsequently in hexane in order to remove any physisorbed thiol.

2.3. Contact angle measurements (sessile drop)

The contact angles of sessile drops were determined with a video camera system: a video camera was connected to a U-matic video recorder, a TV monitor, and a video printer. Advancing (θ_a) and receding (θ_r) contact angles were determined by depositing a water (or hexadecane) drop onto a surface through a syringe without removing the syringe tip. By very slowly adding or removing water, the drops were made to grow or shrink. The contact angles were measured just prior to movement of the three phase line as judged from the video image.

References

[1]   Bain, C.D.; Troughton, E.B.; Tao, Y.–T.; Evall, J.; Whitesides, G.M.; Nuzzo, R.G. *J. Am. Chem. Soc.* **1989**, *111*, 321–335 (supplementary material).
[2]   Miller, C.; Cuendet, P.; Grätzel, M. *J. Phys. Chem.* **1991**, *95*, 877–886.
[3]   Throughton, E.B.; Bain, C.D.; Whitesides, G.M.; Nuzzo, R.G.; Allara, D.L.; Porter, M.D. *Langmuir* **1988**, *4*, 365–385.
[4]   Hsu, G.S.; Percec, V. *J. Poly. Sci. Polym. Chem. Ed.* **1987**, *25*, 2909–2923.

Chapter 3

Formation of holes in alkanethiol monolayers on gold[1]

Abstract: Self-assembled monolayers of alkanethiols ($C_nH_{2n+1}SH$; n = 3, 8, 12, 18, and 22) adsorbed on gold(111) are investigated with (atomically resolved) scanning tunneling microscopy (STM) and wetting measurements. The characteristic depressions observed in these monolayers with STM are proven to be holes in the underlying top gold surface layer rather than defects in the thiol monolayer itself. The holes originate from an etching process of the gold during adsorption of the thiol molecules: a correlation is obtained between the number of holes observed with STM and the amount of gold measured with atomic absorption spectroscopy in the thiol solution after adsorption. The erosion process is found to vanish as soon as complete self-assembly is observed in STM and wetting. For a dodecanethiol monolayer on gold adsorbed from a diluted methanoic thiol solution, self-assembly is observed within 10 min adsorption time. The average amount of gold in the thiol solution after 10 min corresponds to dissolution of 2% of a monolayer Au(111). The erosion strongly increases when the dodecanethiol adsorbs from undiluted thiol. The amount of holes also increases with decreasing thiol chain length as a result of a lower degree of self-assembly. The surface gold atoms underneath the thiol layer are highly mobile, which is manifest in STM tip-induced reorganization of the thiol layer and in penetration of evaporated gold through the thiol layer. This mobility is believed to be crucial in the etching process. Due to the mobility of thiol molecules during the adsorption process prior to acquiring a complete self-assembled structure, gold dissolves, probably in the form of a gold thiolate complex.

.

3.1. Introduction

Alkanethiols ($C_nH_{2n+1}SH$) are known to form densely packed self-assembled monolayers on gold [1]. Several characterization techniques, like infrared spectroscopy [2], wetting measurements [3–5], and electron diffraction [6,7], show the structure of the longer chain ($n \geq 9$) thiol monolayers on gold to be highly ordered.

Recently, we used STM in an ultrahigh tunnel resistance (R_t) regime for the characterization of the ordering of dodecanethiol adsorbed on gold on a molecular scale [8]. Tunneling under these conditions enables imaging of individual sulphur atoms of the thiol molecules in the self-assembled structure and was found to be truly nondestructive. Under these operating conditions, the distance between the tip and the substrate is large enough to result in a negligible tip/surface interaction. In this work [8] it was found that after a minimum adsorption time of about 10 min, a highly ordered structure of the thiol molecules on the gold is obtained. The molecules adopt a hexagonal and commensurate ($\sqrt{3}\times\sqrt{3}$)R30° overlayer structure on the Au(111) surface. The high degree of ordering of the thiol layers makes them suitable as molecular model systems for studying e.g. the mechanical and interfacial properties of modified metal surfaces. Our interest in self-assembled thiol monolayers is mainly aimed at using them as model systems to study the interaction between (electrochemically deposited) metals and organic surfaces like polymers. The advantage of using self-assembled monolayers in these studies is the controllability of the identity and the concentration of surface functional groups. These ordered molecular assemblies are also of technical relevance for example in the fabrication of (nano)-patterned structures [9,10].

STM measurements indicate the presence of defects in the ordered structure. In our high R_t STM images (Figure 3.1a) they show up in the form of dark lines which could be identified as different types of missing row structures [8,11]. Two other types of defects can be clearly visualized by operating the STM in the usually employed low R_t (<100 GΩ) tunneling regime (Figure 3.1b). One of the
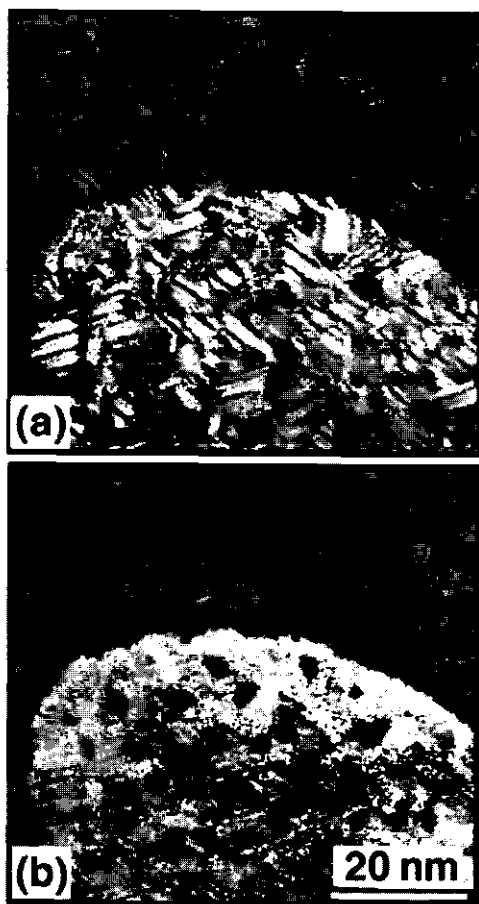
Figure 3.1: STM images of an Au(111) surface with an adsorbed self–assembled monolayer of dodecanethiol measured on the same $60{\times}60$ nm^2 area for two different tunneling resistances: $R_t = 660$ GΩ for (a) and $R_t = 25$ GΩ for (b). Three types of defects can be observed: missing thiol rows (dark lines in (a)), monatomic Au step edges (visible in image (a) and (b)), and depressions (in (b)). The images are obtained in the constant–current mode (1.5 pA).

defects are monatomic steps and can be observed as the border line between two different terraces. These steps are steps in the underlying gold and are also observed on clean gold samples. However, the most prominent defects observed

are depressions (holes) which can be most clearly seen in Figure 3.1b. These depressions have been observed by many other research groups [12–16]. The holes are of a roughly circular shape and about 2–6 nm in diameter and cover about 5–30% of the surface. The depth has been reported to vary between 0.2 and 1.1 nm [12–16]. These depressions are observed for all thiol chain lengths studied. The depressions are not observed on bare gold.

In ref 8 we have presented evidence that these depressions are holes in the underlying Au surface layer. The purpose of this study is to further elucidate the origin and the formation mechanism of the holes. In this chapter we will first present evidence that the observed depressions are indeed holes in the gold. The second part of the chapter concerns the origin of these holes. Aspects like adsorption time and thiol chain length will be discussed. In the third part we will speculate on the mechanism involved in the generation of these holes.

3.2. Experimental

Materials. Information about the thiols is given in chapter 2. In this chapter the alkanethiol will be incidently abbreviated as RSH. The gold(111) samples were prepared by evaporation of a gold layer of 100 nm (99.999%) onto a freshly cleaved mica (Muscovite mica, Goodfellow) sheet at 250°C. Gold samples of 5–cm^2 geometrical area were used. All reagents were analytical grade (Merck).

Preparation of the monolayers. Detailed preparation procedures are given in chapter 2. A thiol monolayer was formed on the gold surface by immersion of the UV/ozone cleaned gold in a glass Petri dish filled with 8 cm^3 of 3.5 mM thiol solution in methanol. The temperature of the thiol solution was kept at 20°C. Occasionally, a dodecanethiol monolayer was deposited from undiluted liquid dodecanethiol. After an adsorption time of t minutes, the sample was removed from the thiol solution and carefully rinsed with 2–propanol and hexane. The monolayers were characterized by advancing (θ_a) and receding (θ_r) sessile drop contact angle measurements with water and hexadecane (HD) [17].

Determination of gold in the thiol solutions. In cases where the gold concentration of the supernatant thiol solution had to be determined, the supernatant (8 cm^3) was decanted into a 10–cm^3 beaker. The gold substrate was subsequently rinsed with 0.25 cm^3 of 2–propanol and 0.5 cm^3 of hexane, respectively. The rinsing liquid was combined with the supernatant. The glass Petri dish was carefully rinsed with 0.5 cm^3 of concentrated (65%) HNO$_3$ in order to remove any adsorbed gold on the glass tray, if present. The HNO$_3$ was collected in the beaker. *Caution: HNO$_3$ reacts violently with most organic materials and must be handled with extreme care.* The total volume of the sample was adjusted to 10 cm^3 with 2–propanol. Due to the nitrous vapours that develop after the mixing of the organic liquids with the concentrated HNO$_3$, the solutions acquired a slightly brown colour.

The total amount of gold in the thiol solution was analyzed with atomic absorption spectroscopy (AAS). For this purpose 0.04 cm^3 of the thiol solution was mixed with 0.01 cm^3 of palladium nitrate (10 mg cm^{-3}) solution. The mixture was injected in a pyrolytically coated carbon oven and heated from 120 to 2700°C. The amount of gold was analyzed with a Perkin Elmer 5000 graphite furnace absorption spectrophotometer with Zeeman background correction for matrix interferences. Gold concentrations of 5 ng or more (in 10 cm^3 of solution) can be determined following this procedure.

STM. STM is done with an instrument operating under ambient conditions using commercial STM electronics (RHK system STM2000 from RHK Technologies, Michigan). Typically, samples were imaged within 1 h after monolayer deposition, though no characteristic changes have been observed over periods of at least 1 week. For imaging, mechanically cut PtPd wires were used and the tip potential V_b was typically biased negatively (–0.1, –1 V) with respect to the sample. All images were obtained at constant tunneling current I_t in the 1–100 pA domain.

3.3. Results and interpretation

3.3.1. Nature of the depressions

Here, we will shortly review the arguments that convinced us of the fact that the depressions observed with STM are holes in the top gold layer. Most arguments are derived from STM measurements.

Depressions are filled with molecules. Figure 3.1a, b shows STM images of a dodecanethiol ("C_{12}–thiol") layer adsorbed on gold. The STM images show the same part of the surface, obtained under different tunneling conditions. The image in Figure 3.1a is measured with R_t = 660 GΩ and in Figure 3.1b with R_t = 25 GΩ. Due to the high tunnel resistance in Figure 3.1a (with a relatively large distance between tip and gold substrate) it is possible to image the individual sulphur atoms of the thiolate [8]. Comparing parts a and b of Figure 3.1, it is noticeable that most of the depressions in Figure 3.1b are filled with ordered thiol. The ($\sqrt{3}\times\sqrt{3}$)R30° structure of the thiol molecules continues in the holes [8]. This excludes the possibility that the depressions are empty regions or regions of disordered thiol embedded in an ordered assembly as had been suggested before [13–16].

Depth of the holes. The depth of the holes is found to be about 0.29 nm and is independent of the chain length of the adsorbed thiol. This depth equals the height of step edges in the thiol-modified gold surface (Figure 3.2) and corresponds to the height of Au–Au steps on the bare gold samples. Only occasionally a hole was found with a deviating depth (sometimes the depth equalled two or three Au–Au steps). In the literature values between 0.2 and 1.1 nm have been reported for the depth of the holes [12–16,24]. The more recent papers, however, consistently report a depth of about 0.2–0.3 nm [12,16b,24].

Tip–induced erosion. Under "normal" tunneling conditions (where $R_t \approx 1$ GΩ), the tip–substrate distance is of the order of 0.5–1 nm [8]. The thickness of the ordered self–assembled thiol monolayer varies between about 1 nm (for
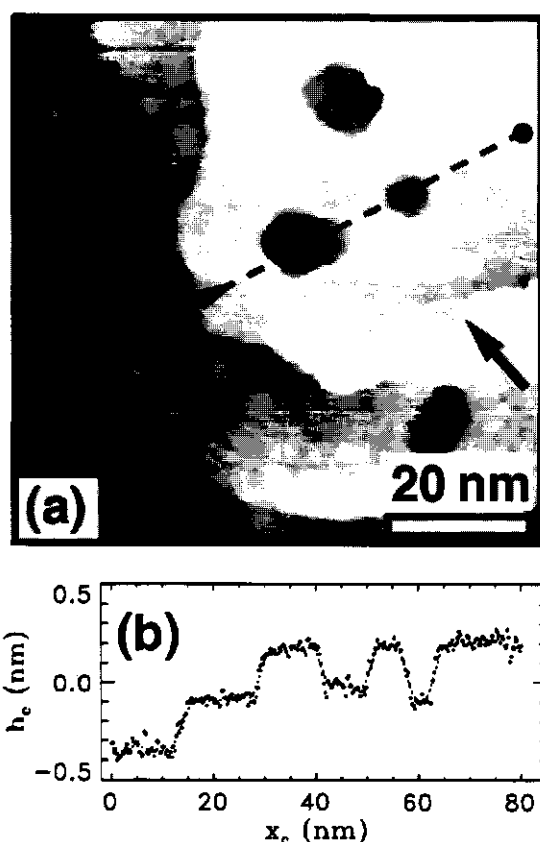
Figure 3.2: STM image (80×80 nm^2) of an Au(111) surface with a monolayer of dodecanethiol. Image (b) shows the profile of the dashed line in (a). Tunnel parameters: $V_b = 1$ V and $I_t = 1.5$ pA.

$C_{10}H_{21}SH$) and 3 nm (for $C_{22}H_{45}SH$) [3] and the tip will thus penetrate the layer. The resulting interaction forces can become so strong that the scanning tip mechanically disrupts the assembly as can be observed in Figure 3.3 ($V_b = 100$ mV, $I_t = 0.1$ nA). This erosion process has also been observed by other research groups [12–14,24].

Figure 3.3 shows a dodecanethiol monolayer through a series of several successive scans. During scanning expansion of the depressions occurs. The
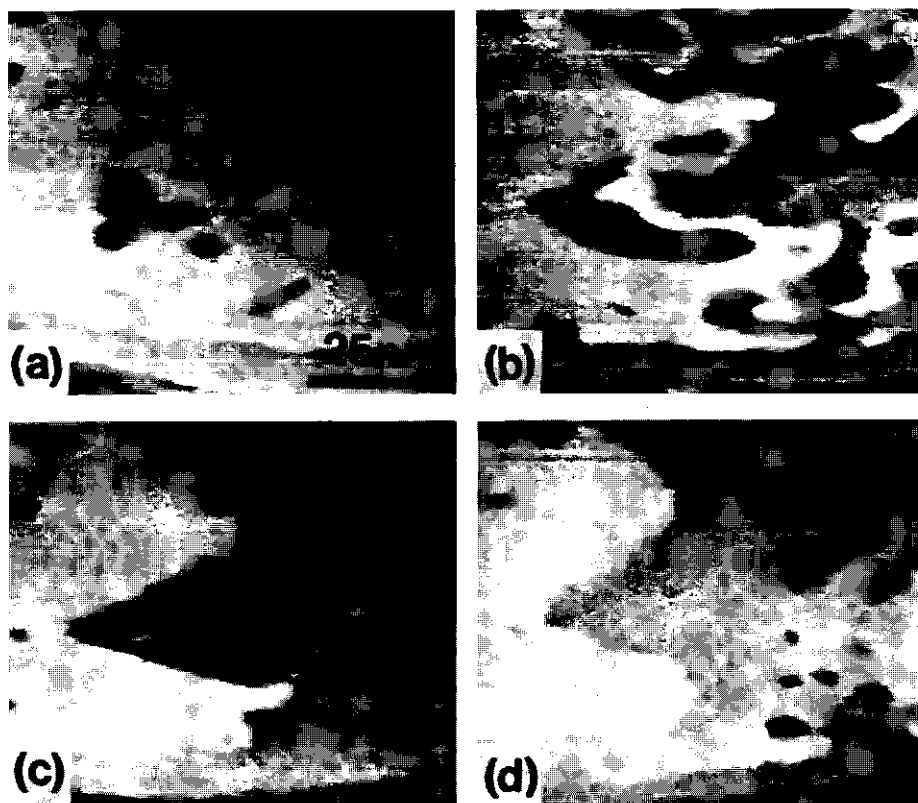
Figure 3.3: Successive scans (70×80 nm^2) of an Au(111) surface with an adsorbed monolayer of dodecanethiol. Tunnel parameters: $V_b = 0.1$ V and $I_t = 0.1$ nA. Under these tunnel conditions the tip disrupts the monolayer: the holes become larger and new holes and step edges appear.

expanding areas connect to other depressions to form larger depressions (Figure 3.3b) and eventually connect to step boundaries (Figure 3.3c). On continuing the scanning we finally see new depressions appearing within the larger depressions that were formed during earlier scans (Figure 3.3d). The depth of both the existing and newly formed depressions is found to be indistinguishable from the

step edge height.

Figure 3.4 shows images of the same sample as in Figure 3.3 but on a larger scale (300×300 nm²), before (Figure 3.4a) and after (Figure 3.4b, c) erosive
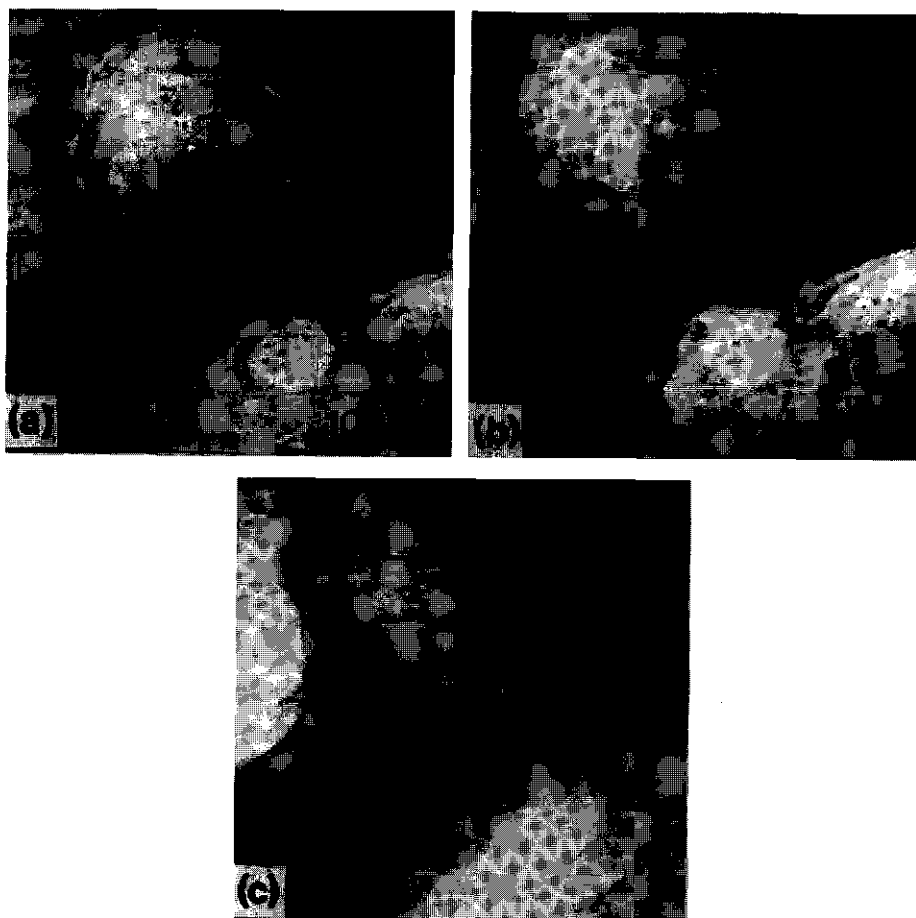
Figure 3.4: STM images (323×323 nm²) of the dodecanethiol monolayer before and after measuring Figures 3.3a–d. The area outlined in (a) represents the scanning area of Figure 3 before imaging. Image (b) is measured directly after measuring Figure 3. Image (c) is measured 60 min (without scanning) after (b). Tunnel parameters: $V_b = 0.1$ V and $I_t = 0.1$ nA.

scanning. The original scanning area of Figure 3.3 (70×80 nm^2) is indicated by the rectangle. Figure 3.4 shows that erosion takes place mainly within the scanning area. The surroundings of this area are hardly affected. Comparing the situation before and after scanning, we see that the number of depressions has decreased after scanning. Only a few large depressions remain. Two new height levels appear: one is a single step height lower than the lowest terrace, the other is one step higher than the originally highest terrace.

After a period of 45 min without scanning, the disrupted structure in Figure 3.4b has relaxed (Figure 3.4c): the highest step has disappeared, and the curvature of the step edges becomes smoother. Apparently, the tip-induced reorganized surface is not stable. This relaxation is possibly driven by a relaxation of stress induced in the thiol/gold layer upon scanning.

Despite the fact that the penetration depth of the tip into the thiol layer is effectively larger for longer chains, the etching behaviour is found to be less pronounced in that case. This is probably due to the mechanical stiffness and the intrinsic stability of the layer, due to the increased lateral van der Waals interactions between the long thiol chains. Gold substrates covered with shorter chains (C_3H_7SH or $C_{10}H_{21}SH$) were not affected during scanning. In these cases the penetration of the tip in the monolayer seems to be too low to cause erosion.

The merging of the holes with step edges during erosive scanning indicates that holes are in fact small terraces, and therefore, the depressions must be one atom deep holes in the top Au surface filled with thiol molecules. At present, a mechanism explaining the (dis)appearance of holes and the appearance of new steps is unknown. However, we speculate that the holes appear as a result of a reorganization of gold atoms immediately underneath the thiol. Due to mechanically induced stress in the thiol layers during scanning, atoms or molecules may reorganize. The weakest bond will be broken first. Apparently, this is not the bond between the gold and the sulphur of the alkanethiolate (Au–SR bond), but the gold–gold bond between the interfacial gold atoms (with chemisorbed thiol) and those in the second layer underneath the adsorbed alkanethiolate (Au–AuSR bond) leading to an enhanced mobility of the

interfacial gold atoms. The Au–AuSR bond breaking may be facilitated by the presence of the chemisorbed thiolate and by the large number of holes (i.e., a large number of step edges) in the top Au surface layer. For example, Holland–Moritz et al. [18] found a statistical trend that the surface of bare gold (evaporated on mica) with the highest density of gold steps is least stable during scanning.
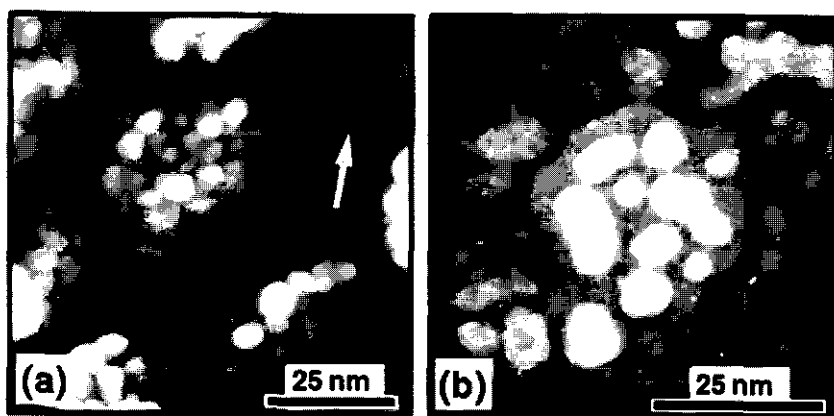
Figure 3.5: STM images of an Au(111) surface with an adsorbed dodecanethiol monolayer after evaporation of a small amount of gold (±1 nm). Image (a) (80×80 nm^2) is measured directly after evaporation. The black arrow points to the evaporated clustered gold, and the white arrow points to the gold that has already penetrated the thiol layer. Image (b) (60×60 nm^2) is measured 3 days after evaporation: the evaporated gold has penetrated the thiol layer. Tunnel parameters: $V_b = 0.2$ V and $I_t = 2$ pA.

The mobility of gold underneath an adsorbed thiol layer can also be clearly visualized by vapour deposition of a small amount of gold (±1 equiv nm) on top of a C_{12}–thiol layer. Directly after deposition of the gold, gold clusters can be observed (indicated by the black arrow in the STM image in Figure 3.5a). The gold atoms tend to cluster because the adhesion between the hydrophobic hydrocarbon layer and the evaporated gold is small. In addition to the clusters, we also observed some white islands as indicated by the white arrow in Figure 3.5a. After a few days all the gold clusters have disappeared. Eventually, the gold is found at the thiol/gold interface where it can be observed as white

islands (Figure 3.5b). The characteristic holes have disappeared. The height of the white islands is equal to a step edge which indicates that the newly formed terraces are covered with thiol. This is confirmed by contact angle measurements with water and hexadecane as the wetting liquids. The contact angles are comparable to those of the sample before evaporation. These observations indicate that there has been transport of gold through the thiol layer (probably through defect sites). Subsequently, the gold diffuses underneath the thiol layer, resulting in surface reconstructions. The amount of gold involved in the transport through and the diffusion underneath the thiol layer is equivalent to about 3 monolayers of Au(111). The gold diffusion experiment proves that gold is mobile underneath the thiol layer. The diffusion process is similar to that observed by Tarlov [19] for evaporated silver on an octadecanethiol ("C_{18}–thiol") monolayer on gold.

No metallization inside the depressions. Sun and Crooks [15] used thiol-modified gold electrodes in their study on electrochemical copper deposition as a function of the thiol coverage. No copper deposition was observed inside the depressions, when the thiol coverage was at a maximum. To us this indicates that the holes are not empty; otherwise metal ions would, due to electrical field effects, have preferentially penetrated the holes, resulting in localized metal deposition.

In summary, the above-mentioned arguments all indicate that the depressions observed with STM are neither pinholes nor defects in the thiol monolayer, but holes in the outermost layer of the underlying gold substrate. Both during nondestructive and erosive scanning, the bottom of the holes is indistinguishable from a lower terrace. The holes are filled with ordered thiol molecules as could be proven with high tunnel resistance STM [8]. Because these holes are filled with ordered thiol molecules, it is not surprising that the electrochemical metal deposition in the holes is blocked and that the holes will hardly influence the properties of the adsorbed layer. This is in agreement with other macroscopic characterization techniques like electrochemical measurements. For example, cyclovoltammetry with hydrophobic thiol-modified gold electrodes in aqueous electrolytes with redox couples in solution showed strong blocking of the electron transfer compared to the case of clean gold [20,21]. From differential

capacitance measurements we know that the dielectric constant of the thiol layer is very low (≈ 2) [17b]. This value is comparable with dielectric constants for solid polymers like polyethylene and suggests a very dense and ordered monolayer. Other defects observed with STM, such as step edges and missing rows in the self-assembly, apparently do not influence the macroscopic properties of the thiol layer. These defects are small enough to prevent ions or molecules to penetrate the monolayer.

In conclusion, the alkanethiol adsorbed on gold behave as rather ideal model system. The gold surface is modified in such a manner that the entire gold interface is covered by a dense packed layer of thiols, without any significant "bare" gold. The surface properties are solely determined by the surface functional groups of the thiol. Defects like holes in the top gold layer do not influence these properties because they are filled with thiol. An important remaining topic is the origin of the holes. This will be discussed below.

3.3.2. Origin of the holes in gold

The presence of holes in the surface Au layer after adsorption of the thiol suggests a mass transport process of Au atoms initiated by the adsorption process. Detection of gold in the thiol solution by Grunze and co–workers [12] led to the conclusion that the holes are a result of a yet unknown etching process. We systematically studied this erosive behaviour of the thiols with a combination of wetting, direct gold determination in thiol solution, and STM measurements, in order to confirm the above conclusion and to elucidate the etching mechanism. The following aspects will be discussed: influence of adsorption time, thiol chain length, and thiol concentration in solution on the degree of extent of gold erosion. The etching mechanism will be discussed in the next section.

Influence of adsorption time. The influence of time of immersion of the gold substrate into a thiol solution on the erosion process was studied using a 3.5 mM
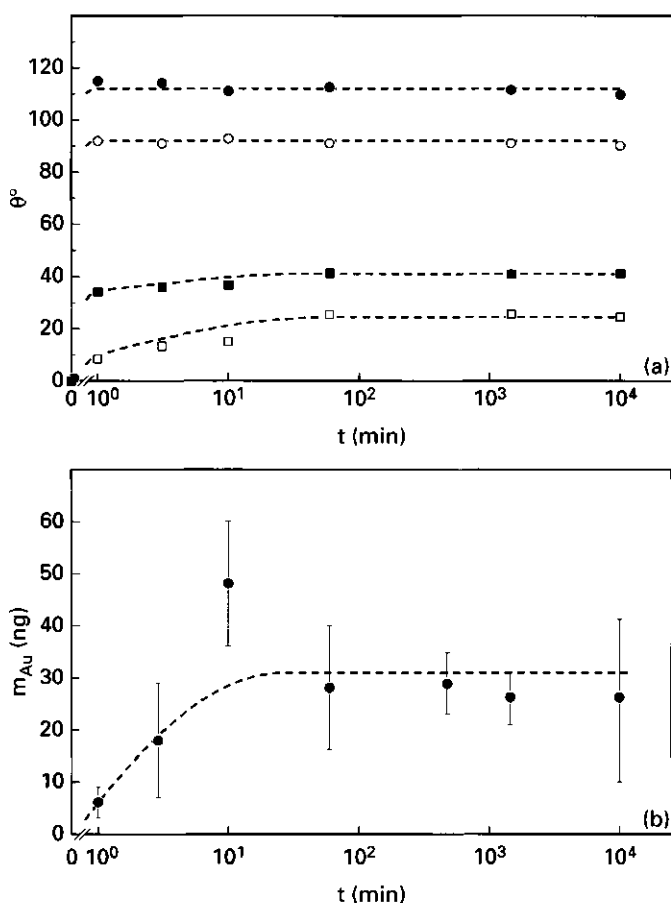
Figure 3.6a,b: Characteristics of a dodecanethiol layer after *t* min adsorption from a 3.5 mM thiol solution in methanol. (a) Advancing (filled symbols) and receding (open symbols) contact angles measured with water (circles) and hexadecane (squares). (b) Amount of gold (m_{Au}) dissolved in the thiol solution (surface Au area in contact with the thiol solution was 5 cm^2).

dodecanethiol solution in methanol. The results for the wetting behaviour are given in Figure 3.6a and are similar to those obtained by other research groups [3]. The wetting is expressed in terms of advancing and receding contact angles with water or hexadecane. The standard deviation of the results is relatively large for deposition times between 1 and 10 min (±7°) and much lower for longer adsorption times (±2°). The influence of adsorption time on the contact angle at
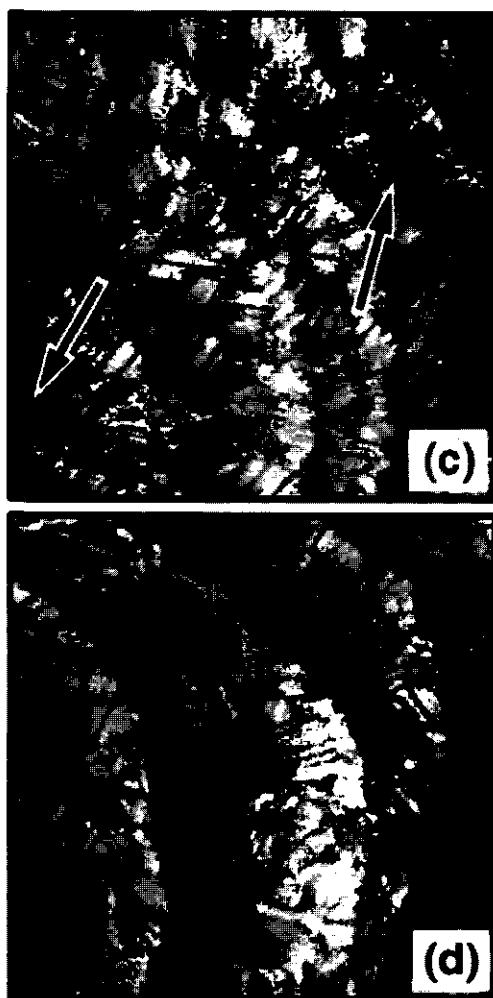
Figure 3.6c,d: Characteristics of a dodecanethiol layer after t min adsorption from a 3.5 mM thiol solution in methanol. (c) and (d) STM images (60×60 nm^2) measured after 1 min and after more than 10 min, respectively. The black arrows in (c) point to the small holes appearing between individual areas of ordered $(\sqrt{3} \times \sqrt{3})R30°$ molecules. Tunnel conditions: $V_b = 1$ V and $I_t = 1.5$ pA.

this thiol concentration is hardly noticeable. Only the receding contact angle with hexadecane (θ_r^{HD}) still increases between 1 and 10 min and stabilizes after 10 min.

The mass of gold determined (m_{Au}) with AAS due to erosion of the gold in the dodecanethiol/methanol solution is given in Figure 3.6b. The results are average values for independent observations on at least two different samples. In order to obtain reproducible results, we found that care has to be taken that all glassware is carefully cleaned, that the gold samples contain no macroscopic defects like those induced by imperfect cleavage of the mica, and that the time between sample preparation and the AAS measurements is short enough to prevent adsorption of the dissolved gold on the glass. Even after all these factors have been given ample consideration, the standard deviation of the results given in Figure 3.6b remains rather large (±10 ng). This can be only partly due to the scatter in the AAS measurements: the deviation is ±5 ng per individual sample. Control experiments were carried out where the gold had solely been in contact with the solvent methanol for 25 h. In that case the amount of gold in solution was below the detection limit (<5 ng).

Figure 3.6c,d shows two STM images obtained after different adsorption times. Figure 3.6c is representative for thiol adsorption during relatively short times (30 s–10 min) and Figure 3.6d shows the characteristic behaviour for longer adsorption times (> 10 min). After 10 min the ordered assembly with holes had always appeared. The number and size of the holes differ per individual sample: the diameter of the holes varied between 2 and 5 nm and the surface coverage of the holes ranged from 5 to 15%. No influence is found of the oxygen concentration in the thiol solution on the number and size of these holes. Bubbling oxygen (oxygen–rich solution) or nitrogen (oxygen–poor solution) through the thiol solution during adsorption had no significant effect on the appearance of the samples.

The exact moment at which the holes first appeared varied largely. During the formation of the ordered structure (between 10 s and 10 min), we first observe low-density structures and islands with the ($\sqrt{3}\times\sqrt{3}$)R30° structure. These islands become larger and finally coalesce. The space between the islands often becomes a small hole (indicated by black arrows in Figure 3.6c). Subsequently, these holes grow probably due to stress induced by the different orientation of the molecules in the individual islands. The time required to establish the final,

ordered, holes containing surface was found to vary largely between about 30 s and 7 min. Lowering the thiol concentration was not found to change this time significantly.

Comparing the results obtained from the three different techniques, some clear trends emerge. After 10 min of adsorption, a self-assembled ordered thiol layer is formed: the contact angle, the amount of dissolved gold, and the STM images become stable. Between 1 and 10 min the thiol film is being formed as observed with STM. The receding contact angle with hexadecane, which is sensitive for ordering effects [5], is somewhat lower than the receding contact angle after a longer adsorption time, indicating a lesser ordering. Also, the increasing amount of dissolved gold between 1 and 10 min indicates that the formation of the ordered layer has not yet been completed.

The average amount of gold dissolved after 10 min of immersion of the 5–cm^2 gold sample in the thiol solution is about 30 ng. Knowing the surface concentration of Au atoms, the amount of dissolved gold can be converted to the percentage of a monolayer which has been dissolved. From the interatomic separation distance between the Au atoms of the (111) plane (0.29 nm [27]) the surface concentration of Au atoms can be calculated: 1.4×10^{15} atoms cm^{-2}. Following this procedure, it is calculated that approximately 2% of a gold(111) monolayer is dissolved. This amount of gold does not completely account for the surface coverage of holes seen with STM. We observed a surface coverage of 5–15% of holes on flat parts of the surface. One should realize, however, that the holes observed with STM are mainly observed on large terraces. No holes were found very close to the step edges. Because our Au/mica samples contain large areas with only very small terraces, and consequently with a large amount of step edges (about 50% of the total sample), the surface coverage of holes with respect to the entire sample is lower ($\approx$2.5–7.5%). This is still somewhat larger than that corresponding to the amount of gold determined with AAS. Apparently, not all the holes result from dissolution of gold. It is likely that part of the holes are a result of reorganization or redeposition of gold atoms during the thiol adsorption process, probably driven by interfacial energy changes or internal stress gradients.

The numbers and sizes of the holes vary per sample. This accounts in part for the large scatter in the amount of dissolved gold (±10 ng) in the thiol solution. The variation in sizes and numbers of holes is also observable when comparing STM images of thiol layers obtained by other researchers [12–16], although the adsorption conditions (adsorption time, solvent, thiol concentration) are somewhat different. This variation suggests that the adsorption and ordering process is rather sensitive to the exact adsorption conditions. The moment for which the ordering becomes more or less complete will vary between different experiments as observed with STM and with receding contact angle measurements with hexadecane: a large variation in results occurs for samples obtained within the first 10 min.

Influence of chain length. Figure 3.7a shows the contact angles with water for alkanethiol-modified gold substrates of different chain lengths. The thiol concentration was 3.5 mM in methanol in all cases and the adsorption time was 25 h. The standard deviation was ±2°. The dashed lines between the data points have no physical meaning but merely serve as a guide to the eye. The contact angles become larger with increasing thiol ($C_nH_{2n+1}SH$) chain length due to the ordering effect [3,22] until a self-assembled structure is obtained ($n>8$). Once this self-assembled layer is obtained, the contact angles become independent of the chain length. However, as a trend, we observe that the receding contact angle with hexadecane decreases slightly with increasing chain length, indicating some disorder in the C_{18}– and C_{22}–thiol monolayers. This effect was not observed when C_{22}–thiol was deposited from hexane. The disorder may result from conformational entropy effects in the long chain thiol layer stimulated by the polar solvent methanol. In this solvent the apolar docosane chains will not be stretched but folded. Adsorption of the unstretched chains may, for entropical reasons, result in some disorder in the adsorbed layer.

In Figure 3.7b the amount of gold measured by AAS in the thiol solution is given. Although the scatter in the amount of dissolved gold in the thiol solutions is relatively large (±10 ng), a significant difference in amount between the different alkanethiol chains is found. The largest amounts of Au were obtained when short thiol molecules were adsorbed. The mass of dissolved gold in a
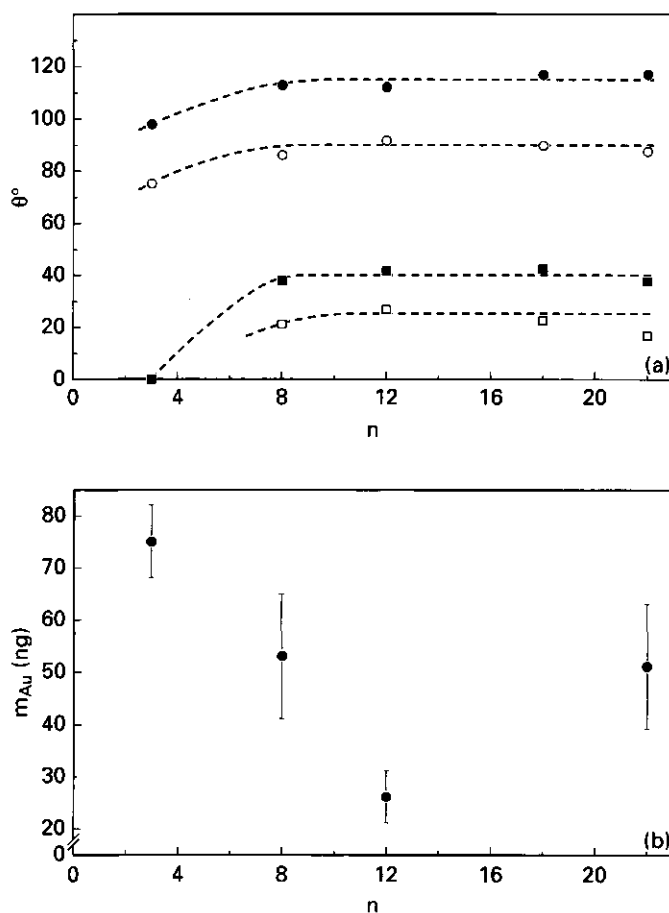
Figure 3.7a,b: Characteristics of an alkanethiol ($C_nH_{2n+1}SH$) layer after 25 h adsorption from a 3.5 mM thiol solution in methanol. (a) Advancing (filled symbols) and receding (open symbols) contact angles measured with water (circles) and hexadecane (squares). (b) Amount of gold (m_{Au}) dissolved in the thiol solution (surface area of gold 5 cm^2).

C_{22}–thiol solution corresponds to about 2.5% of a monolayer. Although Grunze and co-workers [12] found a comparable amount of gold in their thiol solutions (150 ng per 10 cm^2 gold), they erroneously calculated this to correspond to about 50% of a monolayer.
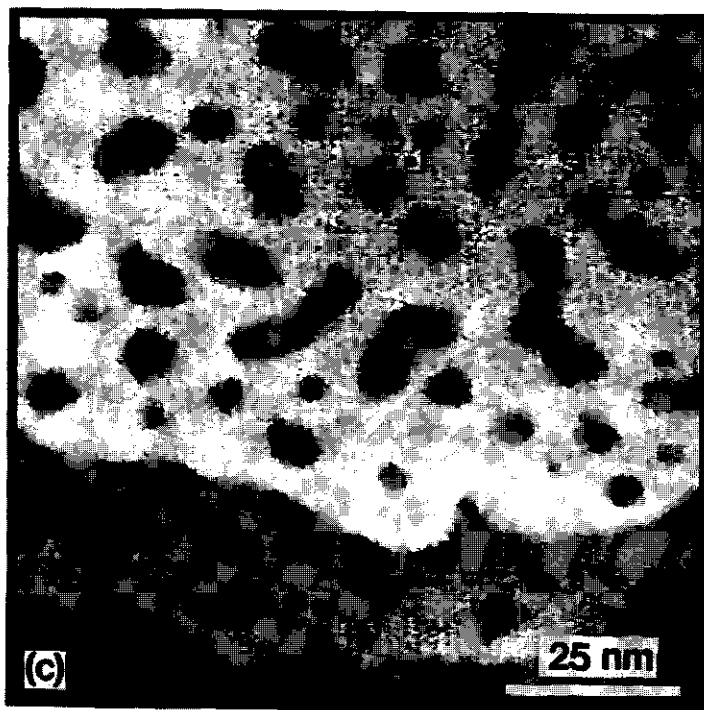
Figure 3.7c: Characteristics of an alkanethiol ($C_nH_{2n+1}SH$) layer after 25 h adsorption from a 3.5 mM thiol solution in methanol. STM image (100×100 nm^2) of a propanethiol monolayer on gold. Tunnel conditions: $V_b = 0.1$ V and $I_t = 0.1$ nA.

Figure 3.7c shows a typical STM image of a C_3–thiol monolayer adsorbed on gold. The sample deviates significantly from the C_{12}–thiol sample (see for example Figure 3.1b). The holes are larger (diameter $\approx$6 nm), and the shape of the holes is less smooth. The coverage of holes is $\pm15\%$. The STM images of the C_{22}–thiol monolayer do not differ much from the C_{12}–thiol images.

Combining the STM images and the gold dissolution results obtained for the C_3– and the C_{12}–thiol, we see that qualitatively the number of holes is linked to the amount of dissolved gold. More gold is dissolved when larger or more holes are observed. This observation supports our hypothesis that holes are a result of an etching process. The etching is stronger when shorter chains are adsorbed.

Influence of thiol concentration. The influence of the thiol concentration on the erosion behaviour of gold was studied for C_{12}–thiol using two extreme conditions: a relatively low concentration (3.5 mM in methanol) and undiluted thiol. The adsorption time was 25 h in both cases. The results of the contact angle and the gold measurements are given in Table 3.1. The contact angles are similar, but the amount of gold dissolved in undiluted thiol is much larger. The amount of gold obtained after thiol adsorption from the undiluted thiol (≈ 105 ng) corresponds to about 5% of a Au monolayer.

Table 3.1: Influence of the C_{12}–thiol concentration on the properties of an adsorbed monolayer on gold after 25 h of adsorption.

concentration	θ_a^{H2O} (deg)	θ_r^{H2O} (deg)	θ_a^{HD} (deg)	θ_r^{HD} (deg)	Δm_{Au} (ng)
3.5 mM in methanol	112	91	41	26	26
pure (100%)	112	95	42	31	105

The STM image of the gold substrate after adsorption of the C_{12}–thiol from the undiluted liquid is given in Figure 3.8. The gold surface is strongly eroded. Even the step edges are not smooth: holes have formed in the step edges. The surface coverage of the holes is about 30%.

Comparing the STM and the gold erosion results for the two different concentrations, we observe, like for the propanethiol, a clear correlation between the amount of gold found in the thiol solution and the number of holes: the stronger the Au surface is eroded, the more gold is found in the thiol solution. The amount of gold in the thiol (solution), however, is less than the amount corresponding to the number of holes observed with STM. The relatively high contact angles with water and with hexadecane for a C_{12}–thiol-modified gold substrate adsorbed from the undiluted thiol indicate that erosion does not negatively affect the self-assembly process.
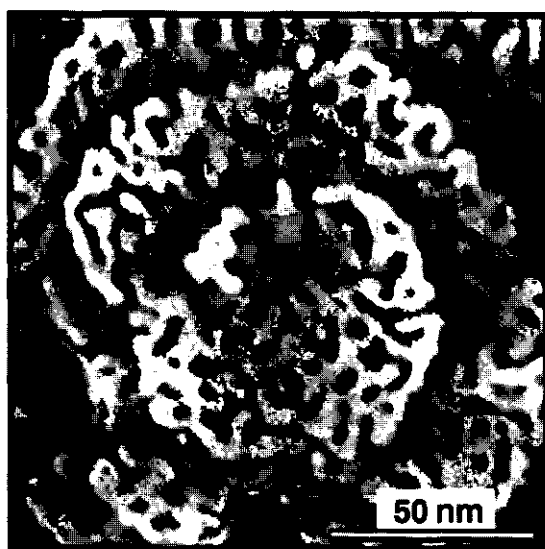
Figure 3.8: STM image (130×130 nm^2) of an Au(111) surface with a monolayer of dodecanethiol adsorbed from a 100% thiol solution. Tunnel parameters: $V_b = 0.075$ V and $I_t = 1.5$ pA.

In summary, it can be concluded that there is a definite and qualititative correlation between the number of holes observed with STM and the amount of gold found in the thiol solution. The cause of the occurrence of holes is likely to be some, yet unidentified, (electro)chemical etching process initiated by the adsorption of the thiol on which we will speculate in the following section.

3.3.3. Etching mechanism

Our present results clearly show that the depressions observed with STM are holes in the underlying gold layer due to etching during thiol adsorption. The remaining question is what mechanism causes this erosive process. A more systematic study is required to completely unravel the mechanism. For the time being, we restrict ourselves to discussing some of the aspects involved in the generation of holes and dissolution of the gold and the possible etching mechanism.

One aspect which is very important in the etching process is the mobility of the surface gold atoms. In several cases this mobility was manifested: STM tip-induced reorganization (Figure 3.4), transport of vacuum deposited gold through the thiol layer and incorporation in the underlying gold (Figure 3.5), and temperature-induced mobility [11,23]. In the latter two cases (nearly) all holes disappeared. The observed mobility indicates that the Au–AuSR bond is relatively weak compared to the Au–SR bond. Apparently, an interfacial Au–AuSR bond can easily be broken and re-formed.

This mobility may be crucial when the thiol molecules are adsorbing on the gold substrate. As a result of the exothermic headgroup-substrate (S–Au) interactions [1], thiol molecules will try to occupy every available binding site on the Au surface. In this process they push aside molecules that have already adsorbed [1]. Prior to final pinning there has to be some surface mobility to achieve a crystalline molecular assembly. As observed with STM during very short adsorption times, the assembling first occurs in ($\sqrt{3}\times\sqrt{3}$)R30° structured islands which partly cover the Au surface. These islands coalesce, and small holes appear between them. The holes become larger with time until a final ordered ($\sqrt{3}\times\sqrt{3}$)R30° structure is established. The stress in the Au–thiolate layer resulting from the random adsorption of the thiol molecules will induce breakage of the relatively weak interfacial Au–AuSR bonds and mobility of the Au–thiolate. Once a Au–AuSR bond is broken, the resulting Au–thiolate complex may dissolve in the thiol/methanol solution. Such complexes are known to be very stable [24,25]. However, not all the holes are caused by dissolution of the Au. The amount of gold determined in the thiol solution was always less than the amount of gold corresponding to the amount of holes observed with STM, pointing to the existence of a secondary effect: a reorganization of surface Au–atoms and/or redeposition of Au–thiolate complexes onto the surface.

We observed the strongest etching effect for the shortest chain (Figure 3.7b, c). From the wetting measurements (Figure 3.7a) and other techniques [3,20], it is known that monolayers of thiol molecules shorter than about 11 carbon atoms are not self-assembled although the surface coverage of the molecules is still of the ($\sqrt{3}\times\sqrt{3}$)R30° type [6,26]. Only the longer chains form a self-assembled

monolayer. Apparently, the lack of self-assembly of the adsorbed molecules stimulates the etching of the gold. This may be due to an exchange of already adsorbed thiol with the thiol molecules in solution: a Au–AuSR bond breakage instead of a breaking Au–SR bond. The shorter the alkanethiol chain, the better the solubility of the Au–thiolate complex in (polar) methanol. However, the etching of the gold in the short chain thiol solution is not a continuous process, even though no self-assembled structure is formed. It stops within 1 day: the amount of gold dissolved after 25 h did not differ significantly from the amount observed after 1 week. Apparently, the formation of an ordered $(\sqrt{3}\times\sqrt{3})R30°$ structure suffices to prevent further gold erosion.

The relatively large amount of gold dissolved in a C_{22}–thiol solution ($\approx$46 ng) seems to contradict the above conclusion (Figure 3.7b). However, the wetting measurements showed some disorder (Figure 3.7a) in the C_{22}–thiol monolayer as a result of the adsorption of the apolar thiol from a polar solution: the docosane chains in methanol will not be stretched but folded. Adsorption of the folded chains may induce some reorganization of the adsorbed chains before a stable structure is obtained. This reorganization process may increase the etching of gold.

The extent of gold erosion is also affected by the concentration of the thiol solution from which adsorption takes place: stronger erosion is observed when the thiol is adsorbed from undiluted thiol (Table 3.1, Figure 3.8). At present, it is not clear what causes the increased erosion. One aspect which probably plays an important role is the solubility of the thiol and of the Au–thiolate complexes in methanol compared to the solubility in undiluted thiol. The poor solubility of the Au–thiolate complex in methanol [24] may reduce the erosion process.

No influence was found of the oxygen concentration in the thiol solution on the number and size of the holes in the substrate. Apparently, the (electro)chemical reaction involved in the erosion process occurs in both oxygenated and deoxygenated adsorbate solutions.

Notwithstanding the uncertainties about the precise chemistry involved in the

gold erosion process, it is clear that the formation of holes is catalyzed by stress in the Au–thiolate layer: the random adsorption of thiols results in stress in the Au/thiol layer. The subsequent movement of the molecules results in reorganization of the gold surface and in gold dissolution, probably in the form of gold thiolate complexes.

3.4. Conclusions

In this chapter we have shown that the depressions or holes observed with STM in self-assembled thiol layers on a gold substrate are neither pinholes nor defects in the thiol layer, but holes in the outermost layer of the underlying gold substrate. The atomically resolved STM measurements showed that the holes are filled with thiol. The bottom of the holes is indistinguishable from a lower terrace. Because the holes are filled with thiol molecules, the thiol in the holes behaves similar to the thiol on the terraces. This makes the adsorbed thiol layers rather ideal model systems: the holes will hardly influence the properties of the adsorbed thiol layer such as the amount of blocking of electron transfer across the layer.

From the correlation between the amount of gold measured in the thiol solution after adsorption and the amount of gold corresponding to the total area of holes in STM images, we conclude that the holes result from etching during adsorption. However, the amount of gold in the thiol solution was less than the amount observed with STM. For a self-assembled dodecanethiol monolayer on gold, the amount of gold in the thiol solution is about 2% of a monolayer Au(111), whereas with STM a number of holes equivalent to 2.5–7.5% was found. We believe, that except for dissolution of Au atoms during adsorption of the thiols, reorganization of surface Au atoms also plays an important role in reaching the final surface morphology.

The erosion process stops as soon as an ordered structure (not necessarily self-assembled) is obtained. For dodecanethiol this situation is reached after about 10

min of adsorption. Due to a lack of self-assembly, the erosion is stronger for shorter thiol chains, like propanethiol.

Although the exact mechanism is not yet known, it is clear that the mobility of gold atoms underneath the thiol plays a very important role in the etching. The mobility was observed in STM tip-induced erosion, heating [11], and gold evaporation experiments. The mobility indicates weak Au–AuSR bonds that can easily be broken. Mobility may also occur during the random adsorption of the thiol molecules. The random adsorption results in a stressed gold–thiolate layer, and consequently the molecules move before attaining a crystalline molecular assembly. This interfacial stress probably catalyses the breaking of Au–AuSR bonds, leading to dissolution of Au, presumably in the form of gold–thiolate complexes.

References

[1]   Ulman, A. *An Introduction to Ultrathin Organic Films*; Academic Press: New York, 1991; pp 237–304 and references therein.

[2]   Nuzzo, R.G.; Dubois, L.H.; Allara, D.L. *J. Am. Chem. Soc.* **1990**, *112*, 558–569.

[3]   Bain, C.D.; Troughton, E.B.; Tao, Y.–T.; Evall, J.; Whitesides, G.M.; Nuzzo, R.G. *J. Am. Chem. Soc.* **1989**, *111*, 321–335.

[4]   Bain, C.D.; Evall, J.; Whitesides, G.M. *J. Am. Chem. Soc.* **1989**, *111*, 7155–7164.

[5]   Bain, C.D.; Whitesides, G.M. *J. Am. Chem. Soc.* **1989**, *111*, 7164–7175.

[6]   Dubois, L.H.; Zegarski, B.R.; Nuzzo, R.G. *J. Chem. Phys.* **1993**, *98*, 678–688.

[7]   Strong, L.; Whitesides, G.M. *Langmuir* **1988**, *4*, 546–558.

[8]   Schönenberger, C.; Sondag–Huethorst, J.A.M.; Jorritsma J.; Fokkink, L.G.J. *Langmuir* **1994**, *10*, 611–614.

[9]   Sondag–Huethorst, J.A.M.; van Helleputte, H.R.J.; Fokkink, L.G.J. *Appl. Phys. Lett.* **1994**, *64*, 1–3, and references therein; chapter 9, this thesis.

[10]   Abbott, N.L.; Folkers, J.P.; Whitesides, G.M. *Science* **1992**, *257*, 1380–1382.

[11]   Schönenberger, C.; Jorritsma, J.; Sondag–Huethorst, J.A.M.; Fokkink, L.G.J., submitted to *J. Phys. Chem.*

[12]   Edinger, K.; Gölzhäuser, A.; Demota, K.; Wöll, Ch.; Grunze, M. *Langmuir* **1993**, *9*, 4–8.

[13]   (a) Kim, Y.–T.; Bard, A.J. *Langmuir* **1992**, *8*, 1096–1102. (b) Kim, Y.–T.; McCarley, R.L.; Bard, A.J. *Langmuir* **1993**, *9*, 1941–1944.

[14]   Ross, C.B.; Sun, L.; Crooks, R.M. *Langmuir* **1993**, *9*, 632–636.

[15]   Sun, L.; Crooks, R.M. *J. Electrochem. Soc.* **1991**, *138*, L23–L25.

[16]   (a) Haüßling, L.; Michel, B.; Ringsdorf, H.; Rohrer, H. *Angew. Chem., Int. Ed. Engl.* **1991**, *30*, 569–572. (b) Dürig, U.; Züger, O.; Michel, B.; Häußling, L.; Ringsdorf, H. *Phys. Rev. B* **1993**, *48*, 1711–1717.

[17]   (a) Sondag–Huethorst, J.A.M.; Fokkink, L.G.J. *Langmuir* **1992**, *8*, 2560–2566, and chapter 4, this thesis. (b) Sondag–Huethorst, J.A.M.; Fokkink, L.G.J. *J. Electroanal. Chem.* **1994**, *367*, 49–57, and chapter 5, this thesis.

[18]   Holland–Moritz, E.; Gordon II, J.; Borges, G.; Sonnenfeld, R. *Langmuir* **1991**, *7*, 301–306.

[19]   Tarlov, M.J. *Langmuir* **1992**, *8*, 80–89.

[20]   Porter, M.D.; Bright, T.B.; Allara, D.L.; Chidsey, C.E.D. *J. Am. Chem. Soc.* **1987**, *109*, 3559–3568.

[21]   Chidsey, C.E.D.; Loicacono, D.N. *Langmuir* **1990**, *6*, 682–691.

[22]   Laibinis, P.E.; Whitesides, G.M.; Allara, D.L.; Tao, Y.–T.; Parikh, A.N.; Nuzzo, R.G. *J. Am. Chem. Soc.* **1991**, *113*, 7152–7167.

[23]   McCarley, R.L.; Dunaway, D.J.; Willicut, R.J. *Langmuir* **1993**, *9*, 2775–2777.

[24]   Al–Sa'ady, A.K.H.; Moss, K.; McAuliffe, C.A.; Parish, R.V. *J. Chem. Soc., Dalton Trans.* **1984**, *8*, 1609–1616.

[25]   Chadha, R.K.; Kumar, R.; Tuck, D.G. *Can. J. Chem.* **1987**, *65*, 1336–1342.

[26]   Widrig, C.A.; Alves, C.A.; Porter, M.D. *J. Am. Chem. Soc.* **1991**, *113*, 2805–2810.

Chapter 4

Potential-dependent wetting of octadecanethiol-modified polycrystalline gold electrodes[1]

Abstract: A Wilhelmy plate technique is used to characterize the potential-dependent wetting of octadecanethiol ($C_{18}H_{37}SH$)-modified polycrystalline gold electrodes in 10^{-2} M K_2SO_4. This technique is relatively simple and provides information on the electrostatic component of the solid electrode/solution interfacial tension ($\Delta\gamma_{SL}$ (E)) and the electrocapillary maximum (ecm). Wetting measurements are carried out simultaneously with differential capacitance measurements and cyclovoltammetry. In the potential range where only double layer charging occurs, the adsorbed, self-assembled $C_{18}H_{37}SH$ layer is found to be very stable. The extreme hydrophobicity, the low differential capacitance (~0.7 μF cm^{-2}) and the low double layer current (a factor of 100 less than for clean gold) are all indicative of the insulating dielectric character of these monolayers. By scanning from the ecm at about -0.45 V(SCE) to 0.8 V(SCE), the advancing contact angle decreases from 116° to 110°, corresponding to a decrease in γ_{SL} of 7 mN m^{-1}. The observed relationship between $\Delta\gamma_{SL}$ and E can be conveniently described by interfacial thermodynamics.

4.1. Introduction

In the past few years, an increasing number of studies have been devoted to alkanethiols adsorbed from organic solutions on solid surfaces like gold. Adsorbed alkanethiols, $CH_3(CH_2)_{n-1}SH$, easily form oriented, ordered structures (for $n>9$), often referred to as "self-assembled" monolayers. Frequent topics of study are (electrochemical) stability, structure, insulation properties, and wettability of these layers [1-15].

The long–chain thiols form monolayers that are quite stable as electrode coatings. These layers strongly block electrochemical oxidation of the underlying metal and also electron transfer with redox couples in solution [1,3-5,13]. In general, electrodesorption of the monolayer is not found in the region of the voltammogram where only double layer charging occurs. In this region no transfer of charge occurs across the solid/solution interface. Beyond this region, oxidation of the metal surface or hydrogen or oxygen evolution is observed to parallel the disruption of the monolayer integrity [3,5]. Oxidative and reductive desorption of the adsorbed alkanethiols is found in KOH and in H_2SO_4 solutions and occurs near the H_2O oxidation or reduction potentials. The desorption potential depends on the pH of the supporting electrolyte [2,14].

Wetting behaviour of thiol-modified surfaces has been frequently used to gain more information on the surface energetics of the interface [1,7-12]. In the present contribution, the dependence of the contact angle between an aqueous electrolyte and a thiol-modified gold electrode on the interfacial potential is for the first time reported. Measuring the wettability of thiol-modified electrodes at varying electrode potentials (in the double layer region) allows the electrostatic component of the interfacial energy to be determined. Together with capacitance measurements, the potential dependence of wetting helps to reveal the nature of thiol layers at the electrode/electrolyte interface, regarding such aspects as lateral homogeneity of the coating and dielectric properties.

For the determination of the wettability of these modified surfaces as a function

of the electrical potential, we used a recently proposed dynamic recording technique [16-19]. Basically, the method involves gravimetric measurement of the change in wetting characteristics associated with electrocapillary phenomena at partly immersed vertical solid electrodes subjected to a linear potential sweep. In this way the electrode simultaneously serves as the well-known Wilhelmy plate used in conventional surface tension studies.

In the present study, the tensiometric method is used to measure the change in interfacial tension of a gold electrode surface covered with an adsorbed mono-layer of octadecanethiol molecules. The tensiogram is measured simultaneously with the cyclic voltammogram and the differential capacitance.

It is shown by the use of basic interfacial thermodynamic relations that electrostatics consistently account for the change in wettability of the gold/thiol interface with potential.

4.2. Theoretical background

In recent attempts to study the interfacial tension of solid electrodes [16-19], a Wilhelmy plate electrode is used to determine the interfacial tension as a function of the potential. Figure 4.1 schematically depicts such an electrode (with mass m) partly immersed in electrolyte. A meniscus rise (or depression) generally occurs along the perimeter of the electrode. At equilibrium, the tared force F acting on the Wilhelmy plate is given by

$$F = 2(l + d)\gamma_{LV}\cos\theta - ldz_0(\Delta\rho)g \qquad (4.1)$$

where l and d are the width and thickness of the electrode, z_0 is the depth of immersion, $\Delta\rho$ is the difference in density between the liquid and the vapour, γ_{LV} is the surface tension of the electrolyte, and θ is the contact angle.

The contact angle is defined as the angle that is formed at the junction of three phases. At equilibrium the Young equation may be applied to the three–phase
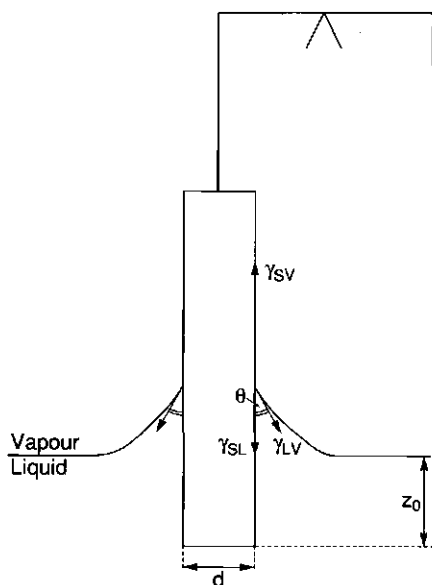
Figure 4.1: A Wilhelmy plate with thickness d, partly immersed (immersion depth is z_0) in liquid. The liquid has a surface tension γ_{LV} and makes a contact angle θ with the plate. The interfacial tensions with respect to the solid/vapour and solid/liquid interface are γ_{SV} and γ_{SL}, respectively.

line along the periphery:

$$\gamma_{LV} \cos\theta = \gamma_{SV} - \gamma_{SL} \qquad (4.2)$$

The symbols γ_{SL}, γ_{LV}, and γ_{SV} denote the surface tensions with respect to the boundaries between the solid (S), liquid (L), and vapour (V) phases, respectively. The electrode/solution interfacial energy γ_{SL} (and thus θ) is a function of the electrode potential E. Both γ_{LV} and γ_{SV} are unaffected by the electrode potential [21]. The derivative of equation 4.2 with respect to E becomes:

$$\gamma_{LV} \frac{\delta \cos\theta}{\delta E} = -\frac{\delta \gamma_{SL}}{\delta E} \qquad (4.3)$$

Taking the derivative of equation 4.1 with respect to E and combining this equation with equation 4.3, yields at constant z_0

$$-2(l + d)\frac{\delta\gamma_{SL}}{\delta E} = \frac{\delta F}{\delta E} \qquad (4.4)$$

Thus, the Wilhelmy plate technique allows γ_{SL} to be determined by measuring the change in the force F on the Wilhelmy plate electrode as a function of the potential E. Thus, ΔF is a result of change in γ_{SL} and a consequent meniscus rise (or depression). The change in F can be determined by measuring the change of mass associated with the meniscus rise, Δm ($\Delta F = \Delta m g$ where g is standard acceleration of free fall).

The interpretation of the interfacial tension of the solid electrode/electrolyte interface is complicated by several factors. In section 4.4 we will give a qualitative interpretation of the first results obtained for the $C_{18}H_{37}SH$/gold system.

4.3. Experimental

Details about materials and electrode preparation are given in chapter 2. A schematic diagram of the experimental apparatus is illustrated in Figure 4.2. The complete apparatus is placed on a vibration-isolated table. It consists of a Wilhelmy plate suspended with a nonconducting thread from a bottom-loading balance (Mettler PM2000 with a sensitivity of 1 mg). The Wilhelmy plate also constituted the gold working electrode of a standard three electrode cell. The cell rested on a micrometer-controllable lifting table. The cell was connected to a potentiostat (Schlumberger 1186 EI/Hi-Tek Instruments PP RI) and a frequency response analyzer (FRA, Schlumberger Solartron 1170). The setup enables a simultaneous measurement of the force on the Wilhelmy plate electrode by measurement of the change of mass associated with the electrolyte meniscus rise, the current and the differential capacitance as a function of the potential.

During experiments, the Wilhelmy plate was electrically connected to the potentiostat through a thin silver wire (100 µm in diameter). This arrangement
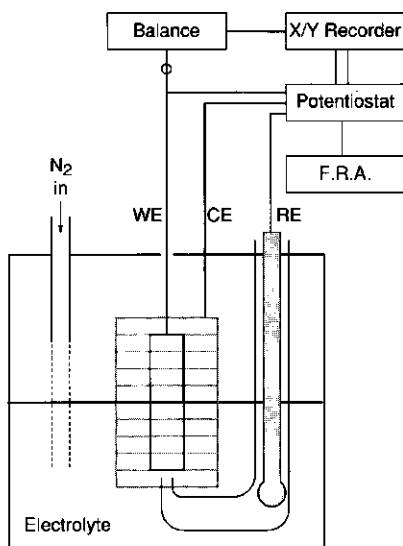
Figure 4.2: Experimental setup for simultaneously measuring current, differential capacitance and wetting as a function of the potential: CE, platinum gauze counter electrode; RE, saturated calomel reference electrode; WE, Wilhelmy plate working electrode partly immersed in electrolyte.

was found to have no effect on the mass-potential measurements. A high surface area platinum gauze was used as the counter electrode. The gauze was bent rectangularly such that the distance between the gold working electrode and the counter electrode was everywhere about 5 mm. The reference electrode was a saturated calomel electrode (SCE). The electrolyte within the cell was deaerated with deoxygenized nitrogen gas for at least 1 h prior to the measurement. As electrolyte, 10^{-2} M K_2SO_4 and 0.5 M H_2SO_4 were used. The surface tension of both electrolytes was 72 mN m^{-1}. During the measurement the cell was kept under a small nitrogen overpressure.

With the potentiostat switched on (often at -0.35 V (SCE)), the gold electrode was partly immersed into the electrolyte by slowly moving the cell upward with the micrometer, thus creating an advancing contact angle θ_a. After stabilizing the position of the electrode for 1 min, a potential scan was started either in cathodic

or anodic direction with a scan rate of 10 mV s^{-1}. Such a low scan rate was selected to be able to measure quasi equilibrium contact angles as a function of the (scanning) potential. The FRA supplied an ac signal with a frequency of 10 Hz and an amplitude of 10 mV to the working electrode. Data were recorded on a X-Y recorder.

Measurements were done on both clean and modified surfaces of the gold working electrode. For the measurements on clean gold, the substrates were cleaned for 15 min in the UV/ozone reactor (both sides) just prior to use. Experiments with the thiol/gold substrates were carried out on freshly deposited monolayers.

The experiments were carried out at 25°C. The reagents were analytical grade (Merck). All measurements were repeated at least three times. Results given in Figures 4.3–4.6 display the average values of these measurements.

4.4. Results and discussion

4.4.1. Static contact angles

The measured advancing contact angle θ_a on freshly deposited polycrystalline gold is about 60°. After cleaning the gold electrode with UV/ozone, the advancing contact angle θ_a reduces to less than 5°. The contact angle θ_a rises rapidly on electrodes exposed to laboratory air. Within 10 min, θ_a is about 40°, and after 1 day, it is between 50° and 80°. The receding contact angle θ_r always remains small (<10-20°), even after longer periods of time.

The increase in the contact angle results from adsorption of organic contamination on the high energy surface of the clean hydrophilic gold [7,23,24]. With UV/ozone, organic contaminants are removed, and a hydrophilic substrate remains [25]. Besides removing contaminants, UV/ozone may also oxidize the surface, inducing an oxide film on gold. This oxide film could also account for

the hydrophilicity of the surface. Characteristics of oxide films have been studied extensively. It was found that anhydrous or hydrated gold oxide species can electrochemically be reduced, as visualized by a reduction peak in the cyclic voltammogram [26-28]. The cyclovoltammogram of UV/ozone cleaned gold in 0.5 M sulphuric acid (Figure 4.3) shows the expected peak due to electrochemical reduction of gold oxide at 0.8 V(SCE). Any unexpected peaks were not found. Consecutive voltammograms in sulphuric acid were found to be reproducible. Since no indication is found for electrochemically active gold oxides, we conclude that UV/ozone cleaned gold is hydrophilic because the surface is free of organic contaminants.
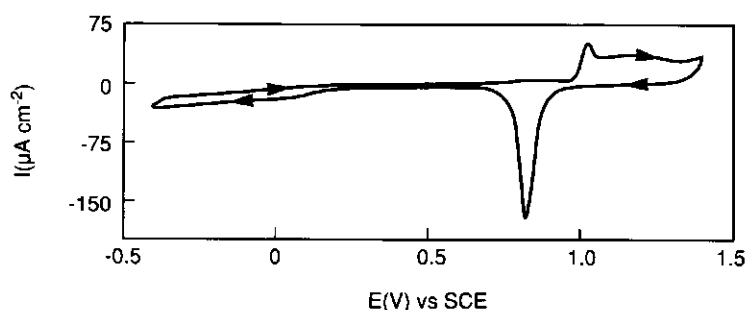
Figure 4.3: Cyclic voltammogram for a UV/ozone cleaned polycrystalline gold electrode in 0.5 M H_2SO_4. The sweep rate was 10 mV s^{-1}.

During the electrochemical measurements, θ_a remained less than 10°. Measurements were always carried out within 10 min after cleaning.

After adsorption of octadecanethiol on UV/ozone cleaned gold, the following contact angles are found: $\theta_a = 117° \pm 2°$ and $\theta_r = 90° \pm 2°$. These contact angles compare favourably with those found in the literature [1,7,9].

4.4.2. Cyclovoltammetry

Typical cyclovoltammograms for a bare gold electrode and a thiol-modified gold electrode in 10^{-2} M K_2SO_4 are shown in Figures 4.4a and 4.4b, respectively.

The cyclovoltammogram of clean gold shows the expected gold oxidation and reduction peaks at about 0.4 V(SCE) and 0.2 V(SCE), respectively. The hydrogen gas evolution on the clean gold starts at -0.5 V(SCE) and the oxygen gas evolution at 0.7 V(SCE).
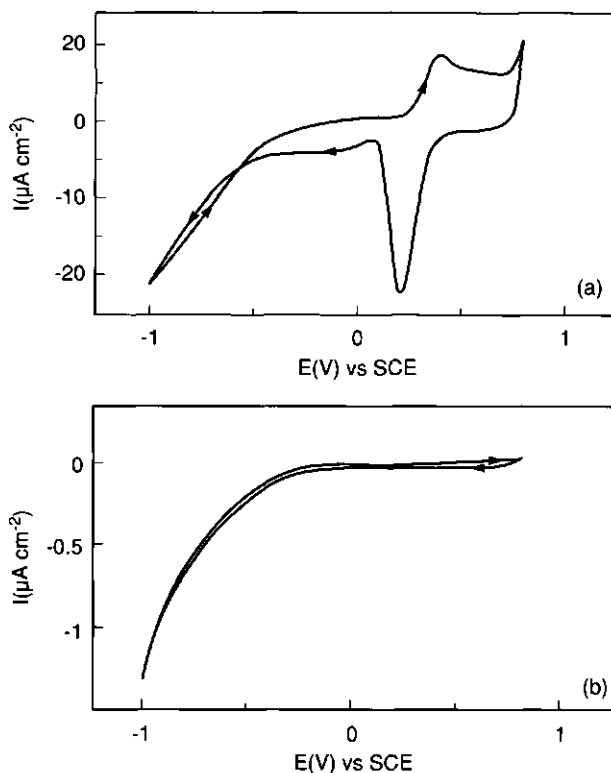
Figure 4.4: Cyclovoltammogram of (a) a UV/ozone cleaned gold electrode and (b) a $C_{18}H_{37}SH$-modified gold electrode in 10^{-2} M K_2SO_4. The starting potential of the sweep was -0.35 V(SCE). The sweep rate was 10 mV s^{-1}.

A comparison between parts a and b of Figure 4.4 demonstrates that the current for gold becomes strongly reduced after monolayer adsorption. Formation of gold oxide on the modified electrode within the chosen scanning area is suppressed. However, by scanning to more anodic potentials (to 0.9 or 1.0 V(SCE)), the onset of gold oxide formation was observed and a small reduction peak appeared at 0.3-0.6 V(SCE) on the backward scan.

In order to compare the passivation properties of our modified electrodes with those of other researchers [3,4,13-15], cyclic voltammograms were also measured in 0.5 M H_2SO_4. It turned out that the gold oxide reduction charge of the modified electrode was reduced to 0.1-0.2% of that for clean gold, which is of the same order of magnitude as found in the literature. The extent of suppression of gold oxidation implies that water penetration in the monolayer hardly occurs. The residual oxidation found at potentials higher than 0.8 V(SCE) may be a consequence of defect sites in the thiol monolayer.

4.4.3. Differential capacitance measurements

As is the case for the charging currents during cyclic voltammetry, the presence of a thiol monolayer causes a dramatic decrease in electrode/electrolyte differential capacitance (Figures 4.5a and 4.5b). The differential capacitance C in 10^{-2} M K_2SO_4 is typically about 0.7 μF cm^{-2}, as compared to capacitances greater than 50 μF cm^{-2} for clean gold measured at 10 Hz. The curves shown are the average of the cathodic and anodic scans for at least four measurements with a standard deviation of less than ± 5%.

For clean gold, C is a pronounced function of the potential. The shape of the differential capacitance curve depends on the surface structure [27,29,30]. The gold we are dealing with is polycrystalline: the X-ray diffraction analysis indicated that the gold surface is predominantly (111), (220), and (311) textured. Thus, the prominent crystal orientations on the surface are typical for our electrodes, and herewith the shape of the experimental differential capacitance curve. Generally speaking, the shape of the differential capacitance curve in Figure 4.5a compares with those obtained by others. The potential of zero charge (pzc), where the capacitance is a minimum, is situated at about 0 V(SCE). The absolute value of C for our bare electrodes, however, is about a factor of 2 larger than that found by, for example, Hamelin [29].

The factors that may account for our high C values obtained in 10^{-2} M K_2SO_4
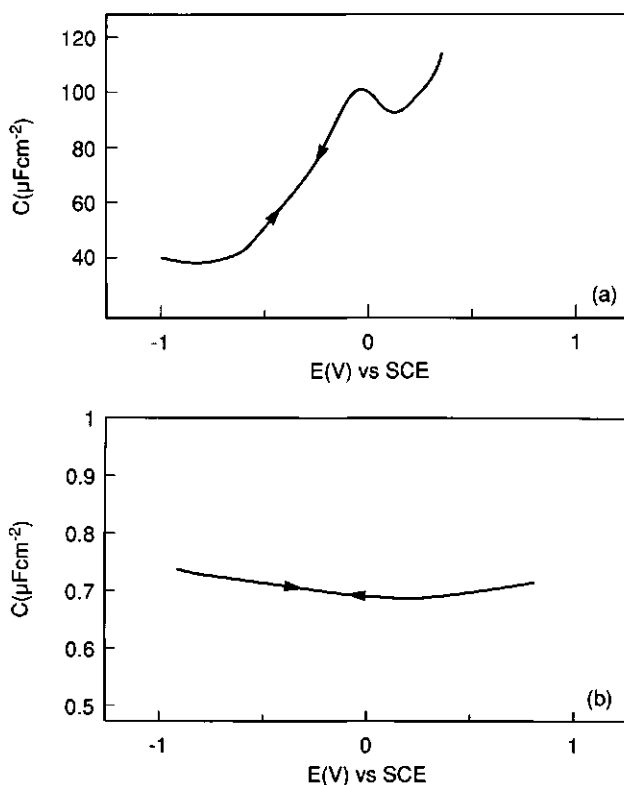
Figure 4.5. Differential capacitance curve for (a) a UV/ozone cleaned gold electrode, and (b) a $C_{18}H_{37}SH$-modified gold electrode in 10^{-2} M K_2SO_4. The starting potential of the sweep was -0.35 V(SCE). The sweep rate was 10 mV s^{-1}.

solution include: A) surface roughness and B) contamination.

Ad A) Surface roughness
Surface roughness effectively increases the surface area and thus decreases the capacitance per area. No estimates are made of the roughness factor. Because the electrodes are of polished polycrystalline gold, the surface is not perfectly smooth on a microscopic scale.

Metal crystals also exhibit a roughness dependence of the differential

capacitance-frequency relation [31-33]. For rough electrodes, the measured capacitance varies almost linearly with the reciprocal of the square root of the frequency υ: the higher the frequency, the lower the measured capacitance. Frequency dependence is considerably minimized for electrodes with a smooth surface. Although the $C \propto \upsilon^{-0.5}$ relationship was not found for our electrodes, we found C to decrease with υ ($C \propto \upsilon^{-0.2}$), suggesting that the surface of the electrodes is indeed not very smooth.

Ad B) Contamination

Continuous scanning of a clean electrode resulted in a decrease of C with time. This is likely due to adsorption of contaminants. For hydrophobic electrodes (i.e., electrodes cleaned with UV/ozone and subsequently exposed to laboratory air for 24 h) even 3 times smaller capacitances were measured. Adsorbed contaminants may partly block the surface, and therefore result in a smaller capacitance.

Because our electrodes were proven to be free of organics, it is expected that surface roughness causes the high capacitance. Hamelin et al. [29] payed due attention to polishing their electrodes. A difference of a factor of 2 in surface roughness seems therefore possible.

The measured capacitance for the modified surface is almost independent of potential. Although the way in which we obtained the capacitance (by impedance measurements) is quite different from that of other researchers [1-5], who measured the capacitive current, and from that calculated C, the order of magnitude for C is the same in both methods. Neglecting possible defect sites for the moment, the overall capacitance C_t of the present system depends on the capacitance of the thiol layer (C_i) and the electrical double layer capacitance (C_d). The two capacitors are connected in series and the overall capacitance is given by:

$$\frac{1}{C_t} = \frac{1}{C_i} + \frac{1}{C_d} \tag{4.5}$$

From the Gouy-Chapman theory it follows that, for electrolyte concentrations in

excess of about 10^{-4} M, C_d is much larger than C_i; hence, $C_t \approx C_i$ for these thiol modified electrodes.

The potential independence of the capacitance resembles the behaviour predicted by the Helmholtz theory of the electrical double layer which treats the interface as an ideal capacitor with two parallel plates, the medium between the plates being octadecanethiol in our case. For this system the capacitance can be described by

$$C_i = \frac{\varepsilon_0 \varepsilon_r}{\delta} \tag{4.6}$$

where ε_r is the relative dielectric constant of the adsorbed thiol layer in electrolyte and ε_0 is the permittivity in vacuum. In air, the thickness of the octadecanethiol layer δ was measured by ellipsometry [1-3,7] and was found to be between 2 and 3 nm. Taking $\delta = 2.5$ nm, we find that $\varepsilon_r = 2$ (compare $\varepsilon_r = 2.3$ for polyethylene). This low value demonstrates the dielectric character of the adsorbed layer. Following this procedure, defects, if any, have been smeared out in an average ε_r. If macroscopically large defects were present in the monolayer, the capacitance of the thiol layer would have to be taken in parallel with that of the uncoated part of the Au surface in order to obtain C_t.

4.4.4. Tensiometry

Measuring tensiograms on properly cleaned gold is not very informative because the advancing contact angle is initially ~0° and does not change with potential. This finding contrasts comparable measurements of Murphy and Wainright [17-19]. In for example, 0.1 M NaF, these researchers measured a tensiogram of gold with a pzc of 0.1 V(NHE). Their cleaning procedure [19], however, resulted in $\theta_a = 79°$ (at the pzc). On reproducing this cleaning method with our electrode, a similar contact angle was obtained. The hydrophobic character of these electrodes indicates that their cleaning procedure did not remove all contaminants from the surface.

Figure 4.6 gives the tensiogram of the thiol-modified gold (standard deviation maximally ±6%), where the variation of the mass of the electrolyte meniscus (Δm) with the electrode potential is given. Care was taken that never during measurements was gold oxide, oxygen, or hydrogen gas formed which would have interfered with the wetting measurements. In obtaining the tensiogram of the modified gold electrodes, we first determined empirically the minimum of the curve. This was situated somewhere between -0.6 V(SCE) and -0.2 V(SCE). A potential of -0.35 V(SCE) was chosen arbitrarily as the starting value for the dynamic measurements in either the cathodic or anodic direction, also defining the starting potential in the voltammogram and the capacitance measurements. At the minimum, the contact angle was identical to θ_a measured with the sessile
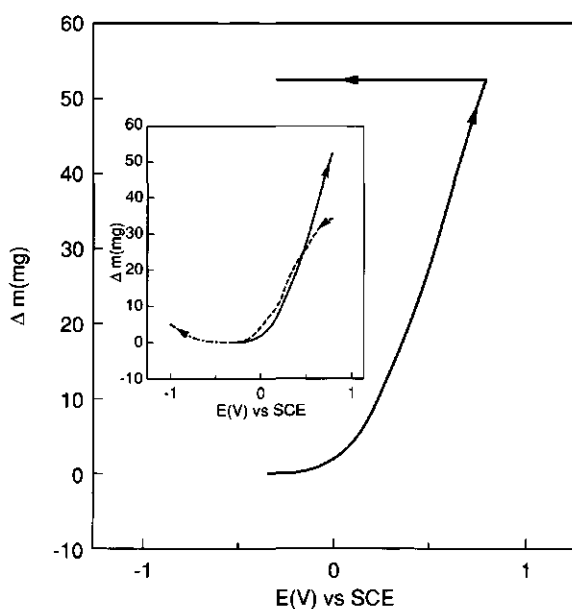
Figure 4.6. Variation of the mass of the electrolyte advancing meniscus with electrode potential of a $C_{18}H_{37}SH$-modified gold electrode in 10^{-2} M K_2SO_4. Starting potential of the sweep was -0.35 V(SCE). The sweep rate was 10 mV s^{-1}. The inset shows the tensiogram for advancing and receding menisci for a single scan: (———) anodic scan direction (advancing); (-·-·) cathodic direction (advancing); (----) cathodic direction (receding).

drop method (117°): when the potential was switched from open circuit to -0.35 V(SCE), no increase in Δm was found, whereas by switching from open circuit to a higher or lower potential, Δm always increased to the same value as found in the sweep tensiogram. An increase in mass results from a decrease in the contact angle. Using a discrete form of equations 4.3 and 4.4, θ can be calculated as a function of E. Although these equations are only applicable under thermodynamic equilibrium, the scan speed is low enough for equations 4.3 and 4.4 to be valid to calculate θ under scanning conditions. By scanning in the anodic direction from -0.35 V(SCE) to +0.8 V(SCE), Δm increases by 52 mg (Figure 4.6), implying a decrease in θ_a from 116° to 110°. A scan in the cathodic direction from -0.35 V(SCE) to -1.0 V(SCE) also resulted in an increase in Δm (see inset of Figure 4.6). On the backscan to -0.35 V(SCE), Δm did not decrease but remained constant. Consequently θ did not increase to its initial value. The irreversibility of the sweep tensiogram is a result of the existence of contact angle hysteresis.
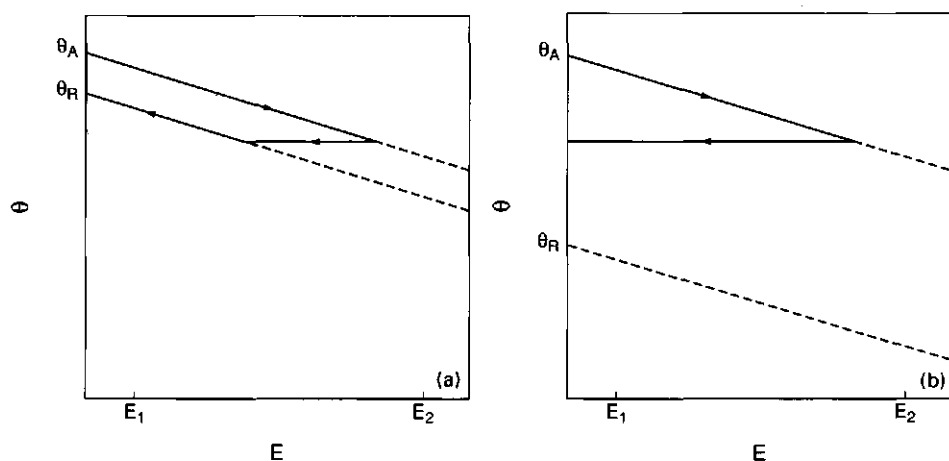
Figure 4.7: Schematic illustration of the influence of contact angle hysteresis on a tensiogram: (a) for small hysteresis; (b) for large hysteresis.

Figure 4.7 schematically shows the influence of contact angle hysteresis on the tensiogram. In the situation of Figure 4.7a, hysteresis is relatively small. When

the potential increases from E_1 to E_2, θ_a decreases. Scanning back to the starting E_1, θ is expected to increase and, consequently, the meniscus to recede. The meniscus starts to recede not until than the contact angle becomes smaller than the limiting θ_r-value (indicated by the dashed lines in Figure 4.7). For situation b, where the hysteresis is much larger, the meniscus will not recede because the contact angle remains larger than the limiting receding contact angle.

The practical situation for the thiol-modified gold, is like Figure 4.7b. At 0.8 V(SCE) θ_a is 110°, much higher than the maximum limiting value for θ_r (90°).

Although for the present system it is impossible to measure θ_r by continuous scanning, we used another way to determine θ_r as a function of E. This was achieved by stabilizing the immersed electrode at 0.8 V(SCE). Next, the electrode was partially emersed, thus creating a receding contact angle, followed by a potential scan in the cathodic direction. Indeed Δm started to decrease, pointing at an increase in θ_r (see the inset in Figure 4.6 and Figure 4.7b). A scan from +0.8 V(SCE) to -0.35 V(SCE) resulted in Δm = -34 mg, corresponding to an increase in θ_r from 86° to 90°.

With equation 4.4, $\Delta\gamma_{SL}$ (E) can now be calculated. The results are given in Figure 4.8. Only the curve for the advancing contact angle is shown (solid curve). The curve is parabolic in shape and yields a maximum at about -0.45 V(SCE). The exact value of the maximum is difficult to determine because the measured Δm and herewith $\Delta\gamma_{SL}$ are zero between -0.6 and -0.2 V(SCE). The decrease in γ_{SL} is about 7 mN m^{-1} in the potential range -0.35 to +0.8 V(SCE). Comparing this decrease with the absolute value for γ_{SL} for water wetted plastics, which is about 40-50 mN m^{-1} [34], this is a decrease of about 15-20%. Thus, a relatively small decrease in θ_a is a result of a relatively strong decrease in γ_{SL}.

4.4.5. Stability of the octadecanethiol layer

The self-assembled $C_{18}H_{37}SH$ monolayer on gold was stable in the potential
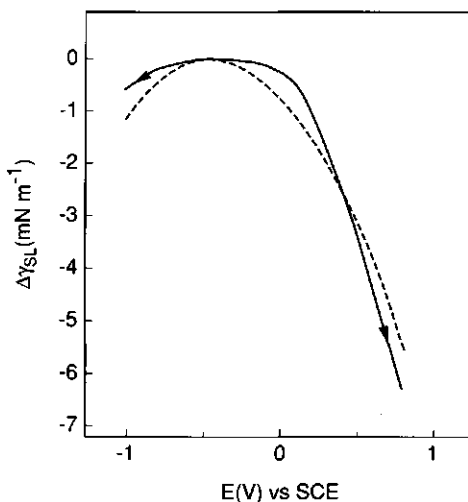
Figure 4.8: Potential dependent change of the surface tension of the gold/$C_{18}H_{37}$SH/ electrolyte phase in 10^{-2} M K_2SO_4. The dashed curve is fitted using equation 4.9, taking $C_t = 0.7$ μF cm^{-2} and ecm = -0.45 V(SCE).

range where only double layer charging occurred. Scanning to potentials corresponding to oxidation of gold and the evolution of hydrogen or oxygen damaged the monolayers. This resulted in an increase in both current and differential capacitance, and in a relatively strong increase of mass of the electrolyte meniscus caused by an increased hydrophilicity due to desorption of thiol. However, in the double layer range, desorption was never observed to occur, in contrast to the results of Widrig et al. [2]. These researchers found a reductive desorption of $C_{18}H_{37}$SH from a Au(111) electrode in 0.5 M KOH positive of the potential for the onset of hydrogen evolution (at -1.3 V (Ag/AgCl)). The charge involved was equal to the desorption of the complete monolayer. Repeating their experiment on our polycrystalline electrodes yielded only small double layer currents. The reason for these conflicting results is unclear, but is probably related to the fact that their layer was less close-packed than ours: their capacitance was larger (≈ 1.7 μF cm^{-2}) and θ_a lower (109°).

4.5. Interpretation of the tensiogram

The parabolic shape of the tensiogram (Figure 4.8) suggests a strong similarity to the electrocapillary curve of mercury [22]. For mercury, in the absence of specific adsorption, the derivative of this curve yields the surface charge and the maximum in the electrocapillary curve, the electrocapillary maximum (ecm), may be identified as the point of zero charge.

For the present system it is also observed that γ_{SL} depends on the electrode potential. From this experimental observation, we conclude that outside the ecm (at about -0.45 V(SCE)), a nonzero electrical potential in the wetting plane is felt by the solution. Specific adsorption of small hydrophilic ions like K^+ and SO_4^{2-} on a hydrophobic thiol surface is unlikely; therefore, a diffuse countercharge has to develop at the solution side of the interface. In the absence of ion penetration in the thiol layer [1], this charge is equal and opposite to the surface charge at the gold/thiol interface. If no transport of (ionic) charge occurs through the thiol layer and the amount of thiol in the interfacial region remains constant (as is the case for the potential region where our wetting experiments were performed), it follows from the Gibbs adsorption equation that

$$(\frac{\delta\gamma_{SL}}{\delta E})_{T,\mu_i} = -\sigma_0 \tag{4.7}$$

where σ_0 is the excess (electronic) surface charge density on the gold, E the potential difference between the bulk metal and the interior of the solution, μ_i the chemical potential of species i, and T the temperature. Equation 4.7 is the Lippmann equation for the thiol-solution interface and is valid if specific adsorption of any of the species i does not occur. Although the surface charge was not directly measured, it can be obtained from the differential capacitance measurements [20]:

$$C_t = (\frac{\delta\sigma_0}{\delta E})_{\mu_i} \tag{4.8}$$

For the present system, C_t is found to be nearly potential independent (Figure

4.5b), because $C_i \ll C_d$ (equation 4.5). Herewith, equations 4.7 and 4.8 may be combined followed by integration, resulting in

$$\gamma_{SL}(E) = \gamma_{SL}{}^0 - \tfrac{1}{2}C_i(E - E_e)^2 = \gamma_{SL}{}^0 + \gamma_{SL}{}^{el}(E) \qquad (4.9)$$

where $\gamma_{SL}{}^0$ is the potential-independent (i.e. "chemical") component of the interfacial energy and $\gamma_{SL}{}^{el}(E)$ (defined as $\tfrac{1}{2}C_i(E - E_e)^2$) is the potential-dependent, electrostatic contribution to γ_{SL} [35] and E_e denotes the potential at the electrocapillary maximum.

Using the above equation, the change in γ_{SL} with E can be calculated from the measured total capacitance. In Figure 4.8 it is shown that our results on thiol-modified electrodes in 10^{-2} M K_2SO_4 can be conveniently fitted by the approach given in this section. The similarity between the measured and calculated curves clearly indicates that the potential-induced change in interfacial tension is of an electrostatic nature. The small divergence between the calculated and measured curve may possibly be due to conformational changes in the thiol layer [36].

Before arriving at definitive conclusions, however, the effect of changing the thiol chain length, the indifferent electrolyte type and concentration on the γ_{SL} (E) curve needs to be investigated in detail. The results of this study are reported on, together with a detailed double layer model for the gold/thiol/electrolyte interface, in chapter 5.

4.6. Conclusions

Simultaneous measurement of the current, differential capacitance, and solid/liquid interfacial tension as a function of the electrode potential provides information on the double layer properties of modified electrode systems. For octadecanethiol-modified polycrystalline gold electrodes in 10^{-2} M K_2SO_4, the following is concluded.
1. Within the potential range where only double layer charging occurs, the self-

assembled $C_{18}H_{37}SH$ monolayer is stable and does not desorb to any measurable extent.

2. Both the low differential capacity ($\sim$0.7 μF cm^{-2}) and the low double layer current (a factor of 100 less than for clean gold) demonstrate that the adsorbed layer acts as a dielectric barrier.

3. The potential-dependent wettability can be conveniently determined using a Wilhelmy plate electrode. The technique is relatively simple and provides valuable thermodynamic information on the solid electrode/solution interfacial tension and the electrocapillary maximum.

4. Wetting properties of the modified gold electrode are strongly affected by the potential. The electrocapillary maximum is situated at about -0.45 V(SCE). By scanning the potential from the electrocapillary maximum to 0.8 V(SCE), the advancing contact angle decreases from 116° to 110°. This relatively small decrease in the contact angle is caused by a relatively strong decrease of the solid/solution interfacial tension by 7 mN m^{-1}, which is a decrease of about 15-20%. Potential-dependent wettability of clean gold can not be measured because properly cleaned gold is hydrophilic over the entire potential range.

5. Both receding and advancing contact angles are measured as a function of the potential and show a similar dependency of the potential. In the electrocapillary maximum, the advancing contact angle is 116° and the receding angle is 90°.

6. The tensiogram, giving solid/solution interfacial tension as a function of the potential, is of parabolic shape. It can be conveniently described by a "Lippmann" approach; the dominating effect for such a potential-dependency is the electrostatic effect.

References

[1]   Porter, M.D.; Bright, T.B.; Allara, D.L.; Chidsey, C.E.D. *J. Am. Chem. Soc.* **1987**, *109*, 3559-3568.
[2]   Widrig, C.A.; Chung, C.; Porter, M.D. *J. Electroanal. Chem.* **1991**, *310*, 335-359.
[3]   Finklea, H.O.; Lynch, M. *Langmuir* **1987**, *3*, 409-413.

[4]   Sabatini, E.; Rubinstein, I.; Maoz, R.; Sagiv, J. *J. Electroanal. Chem.* **1987**, *219*, 365-371.
[5]   Miller, C.; Cuendet, P.; Graetzel, M. *J. Phys. Chem.* **1991**, *95*, 877-886.
[6]   Walczak, M.M.; Popenoe, D.D; Deinhammer, R.S.; Lamp, B.D.; Chung, C.; Porter, M.D. *Langmuir* **1991**, *7*, 2687-2693.
[7]   Bain, C.D.; Troughton, E.B.; Tao, Y-T.; Evall, J.; Whitesides, G.M.; Nuzzo, R.G. *J. Am. Chem. Soc.* **1989**, *111*, 321-335.
[8]   Bain, C.D.; Evall, J.; Whitesides, G.M. *J. Am. Chem. Soc.* **1989**, *111*, 7155-7164.
[9]   Laibinis, P.E.; Whitesides, G.M.; Allara, D.L.; Tao, Y-T.; Parikh, A.N.; Nuzzo, R.G. *J. Am. Chem. Soc.* **1991**, *113*, 7152-7167.
[10]   Bain, C.D.; Whitesides, G.M. *J. Am. Chem. Soc.* **1989**, *111*, 7164-7175.
[11]   Laibinis, P.E.; Fox, M.A.; Folkers, J.P.; Whitesides, G.M. *Langmuir* **1991**, *7*, 3167-3173.
[12]   Thomas, R.C.; Sun, L.; Crooks, R.M. *Langmuir* **1991**, *7*, 620-622.
[13]   Bilewicz, R.; Majda M. *Langmuir*, **1991** *7*, 2794-2802.
[14]   Michelhaugh, S.L.; Bhardwaj, C.; Cali, G.J.; Bravo, B.G.; Bothwell, M.E.; Berry, G.M.; Soriaga, M.P. *Corrosion* **1991**, *47*, 322-328.
[15]   Chidsey, C.E.D.; Loiacono, D.N. *Langmuir* **1990**, *6*, 682-691.
[16]   Hato, M. *J. Colloid Interface Sci.* **1989**, *30*, 130-136.
[17]   Murphy, O.J.; Wainright, J.S. *J. Electrochem. Soc.* **1987**, *134*, 267-268.
[18]   Murphy, O.J.; Wainright, J.S. *J. Electrochem. Soc.* **1988**, *135*, 138-143.
[19]   Murphy, O.J.; Wainright, J.S. *Langmuir* **1989**, *5*, 519-523.
[20]   Hunter, R.J. *Foundations of Colloid Science*; Oxford Science Press: New York, 1987, pp. 345-348.
[21]   Kabanov, B.N. *Electrochemistry of metals and adsorption*; Freud Publishing House: Holon (Isreal), 1969; pp. 18-23.
[22]   Grahame, D.C. *Chem. Rev.* **1947**, *41*, 441-501.
[23]   Schneegans, M.; Menzel, E. *J. Colloid Interface Sci.* **1982**, *88*, 97-99.
[24]   Smith, T. *J. Colloid Interface Sci.* **1980**, *75*, 51-55.
[25]   van der Wel, H.; Lub, J.; van Velzen, P.N.T.; Benninghoven, A. *Mikrochim. Acta (Wien)* **1990**, *II*, 3-18.
[26]   Oesch, U.; Janata J. *Electrochem. Acta* **1983**, *28*, 1237-1246.
[27]   Parsons, R. *Croatica Chemica Acta* **1980**, *53*, 133-146.
[28]   Burke, L.D.; Hopkins, G.P. *J. Appl. Electrochem.* **1984**, *14*, 679-686.
[29]   Hamelin, A.; Sotto, M.; Valette, G. *Compt. Rend. Acad. Sci.* **1969**, *268C*, 213-216.
[30]   Valette, G.; Hamelin, A. *J. Electroanal. Chem.* **1973**, *45*, 301-319.
[31]   Carr, J.P.; Hampson, N.A. *J. Electrochem. Soc.* **1972**, *119*, 325-331.
[32]   Delahay, P. *Double layer and electrode kinetics*; John Wiley, 1965; pp. 129-134.
[33]   Sekine, I. *Denki Kagaku Oyobi Kogyo Butsuri Kagaku* **1975**, *43*, 313-317.
[34]   Extrand, C.W.; Gent, A.N. *J. Colloid Interface Sci.* **1990**, *138*, 431-442.
[35]   Fokkink, L.G.J.; Ralston, J. *Colloids and Surfaces* **1989**, *36*, 69-76.
[36]   Evans, S.D.; Sharma, R.; Ulman, A. *Langmuir* **1991**, *7*, 156-161.

Chapter 5

Electrical double layers on thiol-modified gold electrodes[1]

Abstract: The solid/liquid interfacial tension, capacitive current, and differential capacitance of alkanethiol-modified gold electrodes in K_2SO_4 are measured simultaneously as a function of the electrode potential. The chain length of the thiols is varied between $C_{10}H_{21}SH$ and $C_{22}H_{45}SH$ and the ion concentrations range from 10^{-4} to 10^{-2} M K_2SO_4. It is found that these alkanethiols form extremely dense-packed self-assembled layers. The potential-dependent wetting of the thiol-modified electrodes depends strongly on the chain length of the thiol: the shorter the chain, the stronger the influence. From the potential dependence of the contact angle, the Helmholtz energy of the electric double layer is derived. It is found that measured double layer capacitances are consistent with the model derived from the wetting method: a large and linear potential decay takes place within the thiol layer and a diffuse charge develops at the electrolyte side of the interface. The relative permittivity of the thiol layer is independent of the chain length and is about 2. The K_2SO_4 concentration affects the measured double layer capacitance in a consistent manner, but it does not influence the wettability significantly. It is concluded that the dependence of the wettability on the electrode potential finds its origin in the formation of an electrical double layer and that potential-induced conformational changes within the thiol layer are insignificant.

5.1. Introduction

Long chain alkanethiols, $HS(CH_2)_{n-1}CH_3$, adsorb from solution and form densely packed self-assembled monolayer films on various metals [1,2]. The self-assembled monolayers may have important applications in the engineering of surface properties, like corrosion inhibition, wetting, adhesion promotion and lubrication. A substantial volume of recently published papers on self-assembled layers is concerned with the understanding of the factors that govern the formation of stable layers. Methods used to study these layers are for example ellipsometry, infrared spectroscopy, electrochemical measurements, and wetting. These techniques show that self-assembled monolayers are formed when the alkanethiol chain is larger than about $C_{10}H_{21}SH$ [3–5].

In the present chapter in situ (potential-dependent) wetting measurements [1] in combination with more classical electrochemical measurements are used to characterize the electrical double layer on thiol-modified gold electrodes. Potential-dependent wettability may offer interesting technological applications like (local) manipulation of the surface Helmholtz energy and herewith for example the local wettability. Another application may be in so–called "electrowetting", a phenomenon thus far practically only observed with mercury [6]. Furthermore, thiol-modified hydrophobic metal electrodes may serve as a well–suited model system in studies concerning the fundamentals of the metallization of e.g. plastics [7].

This chapter is the second in a series describing the potential-dependent wetting of monoalkyl thiol films on polycrystalline gold. In chapter 4, we discussed a Wilhelmy plate technique for the measurement of the potential-dependent wettability of solid electrodes. Basically, the wetting characteristics of the solid electrodes associated with the electrocapillary effect are measured while changing the potential. This relatively simple technique provides information about the electrostatic component of the solid electrode/solution interfacial tension and on the electrocapillary maximum (ecm), when used in combination with capacitance measurements and cyclic voltammetry.

The change in wetting properties of the electrode/solution phase boundary is caused by a potential-dependent change in surface tension of the solid/solution interface ($\Delta\gamma_{SL}$) resulting in a change in contact angle ($\Delta\theta$). This $\Delta\gamma_{SL}$ is indirectly measured by recording the change in the force acting on a partly immersed Wilhelmy plate electrode which arises from the change in mass (Δm) due to meniscus rise. The potential-dependent part of the interfacial tension can be calculated using the equation

$$\Delta mg = 2(l+d)\gamma_{LV} \ \Delta\cos\theta = -2(l+d)\Delta\gamma_{SL} \tag{5.1}$$

with l and d being the length and the thickness of the gold electrode, respectively, g the standard acceleration of free fall, and γ_{LV} the liquid surface tension.

To a first approximation the interfacial energy γ_{SL} may be taken to be composed of an electrical (potential-dependent) component γ_{SL}^{el} and a chemical (potential-independent) component γ_{SL}^0 [8]:

$$\gamma_{SL}(E) = \gamma_{SL}^0 + \gamma_{SL}^{el} \tag{5.2}$$

The electrical part is due to the presence of an electrical double layer at the interface.

The double layer of the gold–thiol–electrolyte system is schematically represented in Figure 5.1. This figure shows the electrical potential ψ as a function of the distance from the gold surface. The potential at the gold/thiol interface ψ_0 drops across the thiol layer (with thickness δ). The thiol region is assumed to be free of any charges and, therefore, the potential decays linearly within this layer. The thiol layer has a relative dielectric constant ε_r. The surface potential ψ_0 is equal to the applied electrode potential E minus the electrode potential in the point of zero charge. The potential remaining at the thiol/electrolyte interface is ψ_d. In the electrolyte a diffuse double layer forms. The diffuse double layer is taken to begin at the thiol/electrolyte interface.

The change in the electrostatic contribution to the interfacial tension of the
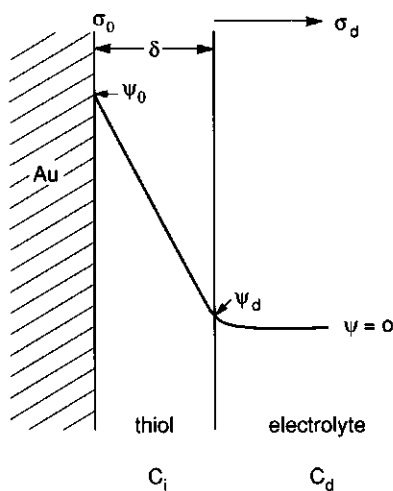
Figure 5.1: Schematic representation of a gold/thiol/electrolyte interface showing the potential ψ as a function of the distance from the gold surface. The charge density in the diffuse double layer is σ_d and is equal but opposite to the surface charge density σ_0.

solid/liquid interface ($\Delta\gamma_{SL}^{el}$) equals the change in double layer Helmholtz energy, ΔF_d.

$$\Delta F_d = \Delta\gamma_{SL}^{el} \tag{5.3}$$

The change in Helmholtz energy of the double layer results from a change in distribution of ions in the electrolyte with changing potential.

Since an experimental method of determining the Helmholtz energy of double layer formation at self-assembled monolayer-modified electrodes is available, such double layers are conveniently analyzed along these lines. As derived by Verwey and Overbeek [9], the total Helmholtz energy of the solid/liquid interface involved in establishing the double layer at constant temperature (T) and constant chemical potential (μ_i) is given by:

$$\Delta F_d = -\int_0^{\psi_0} \sigma_0 d\psi_0 \qquad (5.4)$$

with σ_0 the excess surface charge density on the gold and ψ_0 the electric potential at the gold/thiol interface. Combination of equation 5.3 and 5.4 yields the well-known Lippmann equation.

The surface charge density in equation 5.4 follows from the differential capacitance measurements (for constant T and μ_i)

$$\sigma_0 = \int_{E_e}^{E} C_t d(E - E_e) \qquad (5.5)$$

where C_t is the total capacitance, E is the applied electrode potential and E_e is the potential at the electrocapillary maximum.

The charge per unit area of surface in the diffuse double layer is σ_d (Figure 5.1). Because the charge balance requires that the total charge of this system is zero, excluding specific adsorption, it follows that

$$\sigma_0 = -\sigma_d \qquad (5.6)$$

The charge of the double layer follows from the Poisson–Boltzmann equation. For an electrolyte with n_j^0 ions of type j per volume in the bulk, σ_d is given by

$$\sigma_d = (-sgn\psi_d)(2\varepsilon kT \ \Sigma n_j^0[\exp(\frac{-z_j e\psi_d}{kT})-1])^{1/2} \qquad (5.7)$$

with $(sgn \ \psi_d)$ the sign of the potential, ε the permittivity of the electrolyte, and k the Boltzmann constant. The valence number z_j is either a positive or negative integer.

The system behaves as a pair of capacitors in series (Figure 5.1). The total

capacitance C_t is given by

$$\frac{1}{C_t} = \frac{1}{C_i} + \frac{1}{C_d} \tag{5.8}$$

where C_i is the capacitance of the thiol layer and C_d the capacitance of the diffuse part of the double layer.

In first approximation, C_d is calculated using the Gouy–Chapman model [10,11]:

$$C_d = -\frac{d\sigma_d}{d\psi_d} = (-sgn\psi_d)(\frac{e^2\varepsilon}{2kT})^{1/2}\frac{\sum n_j^0 z_j \exp(\dfrac{-z_j e \psi_d}{kT})}{(\sum_j n_j^0 [\exp(\dfrac{-z_j e \psi_d}{kT})-1])^{1/2}} \tag{5.9}$$

Combining equation 5.5–5.9, C_i can be calculated according to the following procedure. From equation 5.5 σ_0 is obtained by integration of C_t with respect to E and subsequently equation 5.6 gives σ_d. From equation 5.7 $\psi_d(\sigma_d)$ and subsequently $C_d(\psi_d)$ can be calculated (equation 5.9). Having both C_t and C_d available, C_i can be calculated as a function of ψ_0 with equation 5.8.

Assuming the chemical (self-assembled) structure of the thiol layer to be potential independent, the capacitance of the thiol layer can be considered as the capacitance of a parallel flat plate capacitor with the medium between the "plates" being the thiol. The capacitance for the parallel plate system is:

$$C_i = \frac{\varepsilon_0\varepsilon_r}{\delta} \tag{5.10}$$

where ε_0 is the permittivity of vacuum, ε_r is the relative permittivity of the thiol layer and δ the thickness of the thiol layer. Since C_i is known for different thiol chain lengths (and thus different δ), ε_r can be calculated. The value of ε_r contains information on the degree of packing and on possible defects in the thiol layer.

The interplay between wetting and electrochemical parameters follows most clearly from a combination of equations 5.3, 5.4 and 5.5:

$$\Delta\gamma_{SL}^{el} = \Delta F_d = -\int\int C_t[d(E-E_e)]^2 \tag{5.11}$$

Thus measuring C_t followed by a double integration of C_t with respect to the potential, provides the electrostatic contribution to γ_{SL}.

One should be aware that possible potential-induced conformational changes of the thiol layer may complicate the interpretation. As a first order effect, a change in conformation may result in a variation of the capacitance of the thiol layer, for example by a change in the permittivity of the layer. Such a variation has a direct effect on C_t and thus on γ_{SL}^{el} (equation 5.11). Except for the potential-induced conformation effect on γ_{SL}^{el}, the change in conformation of the thiol molecules may also affect γ_{SL}^0. In the case of self-assembled alkanethiol monolayers it is known that they consists of differently ordered overlayers [12] and that the molecules exhibit an average tilt of about 30° on Au(111) and of about 14° on Au(100) with respect to the normal [12]. For the polycrystalline gold electrodes we are using, different domains with different average tilt angles may be present [15]. From STM work it is known that many defects are present [13,14]. Due to the applied potential the overall structure of the thiol layer may change, for example by affecting the tilt angle of the individual domains or by reorganisation or disordering of the molecules. If this were the case, the chemical composition of the interfacial region would change, for instance in terms of the ratio of exposed CH_2/CH_3 groups in the interface [16], thus changing the chemical component of the interfacial tension (i.e. the intrinsic hydrophobicity of the surface). Strictly speaking, potential induced conformational changes may change γ_{SL}^0 without changing the capacitance of the thiol layer, thus leaving γ_{SL}^{el} unaffected. We consider it an important issue of the present study to investigate whether the electrical potential influences the overall structure of self-assembled thiol layers.

The potential-induced change of γ_{SL}^0 as a result of a change in composition of

the thiol/electrolyte interface can only be measured with a method where $\Delta\gamma_{SL}$ is directly measured, such as our Wilhelmy plate wetting method. From the capacitance measurements only the change in electrostatic contribution to γ_{SL} is obtained. Comparison of $\Delta\gamma_{SL}$ measured with the wetting method to that found indirectly via the capacitance measurements provides an indication whether potential-induced chemical changes do indeed occur.

In this chapter we investigate the influence of the thiol chain length and the electrolyte concentration on the potential-dependent wetting of thiol-modified gold electrodes.

5.2. Experimental

The used materials and preparation of the monolayers are described in chapter 2. The experimental apparatus consists of a thiol-modified (Wilhelmy) gold plate suspended with a thread from a bottom loading balance (Mettler PM2000). The Wilhelmy plate was used as the working electrode in a three–electrode configuration to allow potentiostatic control (with a Schlumberger 1186 EI/Hi–Tek Instruments PP RI potentiostat). The scan rate was 10 mV s^{-1}. The potentiostat was coupled to a frequency response analyzer (FRA; Schlumberger Solartron 1170). The FRA supplied an ac signal with a frequency of 10 Hz and an amplitude of 10 mV to the Wilhelmy plate working electrode which was partly immersed in an aqueous solution of K_2SO_4. The concentrations were 10^{-4}, 10^{-3} or 10^{-2} M. The setup enables simultaneous measurement of the change in mass associated with the electrolyte meniscus rise, the capacitive current and the differential capacitance as a function of potential. The change in mass is a result of the change in γ_{SL} as calculated with from equation 5.1. In section 5.3 only the results of the advancing meniscus are presented. The receding meniscus showed similar dependence on the potential [1].

The experiments were carried out at 25°C. The surface tension of the electrolyte solutions (γ_{LV}) was 72 mN m^{-1}. The reagents were analytical grade (Merck). The

results given in Figures 5.2–5.4, 5.8 and 5.9 display the average values of at least four measurements.

5.3. Results and discussion

5.3.1. Tensiometry

The tensiograms for the different thiol chain lengths ($C_{12}H_{25}SH$, $C_{18}H_{37}SH$ and $C_{22}H_{45}SH$) are shown in Figure 5.2. The procedure to obtain these tensiograms from the measured force acting on the Wilhelmy plate electrode is given chapter 4. The standard deviation is maximally ±5%.
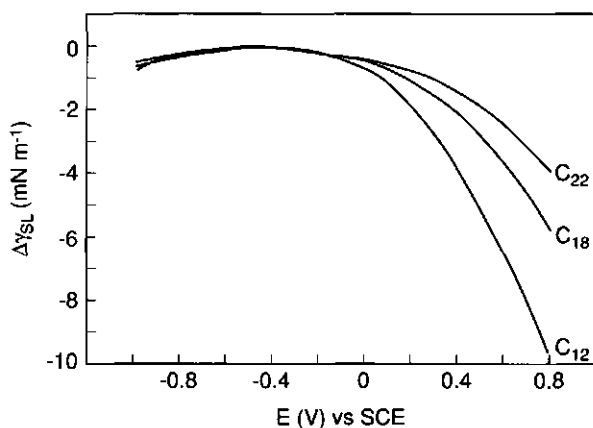
Figure 5.2: Potential-dependent change of the surface tension of the gold/thiol($C_nH_{2n+1}SH$)/electrolyte interface in 10^{-2} M K_2SO_4, measured with the Wilhelmy plate method (n = 12,18,22). The scan rate was 10 mV s^{-1}

All tensiograms are parabolic in shape and have a maximum at a potential of about −0.45 V(SCE), identified as the electrocapillary maximum (ecm). The advancing contact angie θ_a in this maximum is θ_a for water using the sessile drop method. The values for the advancing and receding contact angles (θ_a) of water and hexadecane measured with the sessile drop method are given in Table 5.1 (typical standard deviation ±3°).

The data presented here were measured in aqueous solutions of K_2SO_4 because the use of this indifferent electrolyte enables the maximum (at $\sim$−0.45 V(SCE)) of $\gamma_{SL}(E)$ to be determined: in K_2SO_4 the adsorbed thiol monolayers are stable between −1.0 and 0.8 V(SCE). Voltage excursions beyond these limits were observed to damage the monolayers due to hydrogen evolution or to oxide formation. The 'stable' region is pH–dependent, and shifts in parallel with the oxygen/hydrogen evolution potential on clean gold. For solutions of pH=1, the limits shift about 0.4 V in the positive direction. For this situation the ecm (assuming specific adsorption, which may change the ecm, to be absent) almost coincides with the lower limit for stability, and only one branch of the tensiogram could be measured.

Table 5.1: Characteristics of an alkanethiol layer adsorbed on gold in 10^{-2} M K_2SO_4.

	C_i ($\mu F\ cm^{-2}$)	δ^* (nm)	ε_r	$\theta_a^{\dagger}$ (deg)	$\theta_r^{\dagger}$ (deg)	$\theta_a^{\ddagger}$ (deg)	$\theta_r^{\ddagger}$ (deg)
C_{12}	1.12	1.6	2.0	112	88	43	28
C_{18}	0.76	2.4	2.0	117	90	42	22
C_{22}	0.61	2.9	2.0	117	88	38	17

*from ref 4
†with water
‡with hexadecane

The influence of the chain length on the potential dependence of the solid/liquid surface tension is considerable: the shorter the chain length, the more strongly γ_{SL} decreases with E. For the dodecanethiol (or for short C_{12}–thiol) a decrease of 10 mN m^{-1} is found for a positive scan from −0.45 V(SCE) to 0.8 V(SCE). This corresponds to a decrease in contact angle from 112° to 104° (equation 5.1). Although the decrease in contact angle seems small, the decrease in surface tension is relatively high: Bain et al. [4] found the critical surface tension of the solid/vapour interfacial tension of a C_{22}–thiol layer to be 19 mN m^{-1}. From

Young's law, γ_{SL} can now be calculated for the thiol/electrolyte interface. For θ in the range of 112°–117°, γ_{SL} is about 50 mN m^{-1}. Thus for C_{12}-thiol, γ_{SL} decreases by 20% on scanning from the ecm to 0.8 V(SCE).

5.3.2. Electrochemical measurements

Simultaneously with the tensiograms, the capacitive current and the differential capacitance were measured as a function of potential. The results are shown in Figures 5.3 and 5.4, respectively. The standard deviation of the current measurements is within ±20% and of the capacitance measurements within ±5%. The presence of the thiol layer causes a dramatic decrease in current and in electrode/electrolyte differential capacitance compared to clean gold [1]. The capacitance is given at a frequency (ν) of 10 Hz and is almost frequency independent. For the thiol layers in 10^{-2} M K_2SO_4 a $C \propto \nu^{-0.01}$–relationship was found in the range 0.5 Hz$<\nu<$1000 Hz.

When a shorter chain length is used (for example C_{10}–thiol), the layers become unstable: both current and capacitance increase during continuous cycling presumably due to desorption of the thiol layer. This finding is in agreement
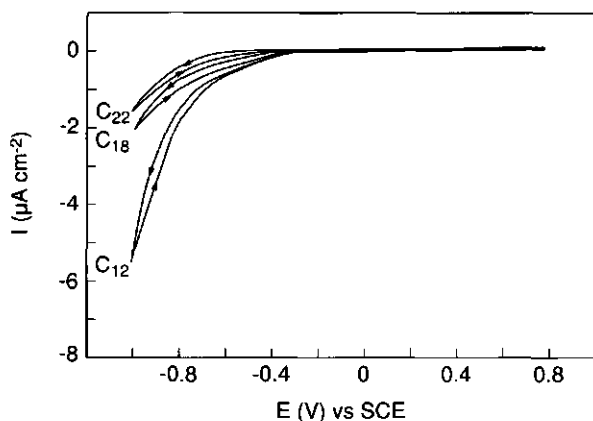
Figure 5.3: Cyclovoltammograms for a thiol ($C_nH_{2n+1}SH$)–modified gold electrode in 10^{-2} M K_2SO_4 ($n = 12,18,22$). The scan rate was 10 mV s^{-1}.

with results of others [3–5] and is probably a result of penetration of electrolyte into the less ordered structure of these monolayers.
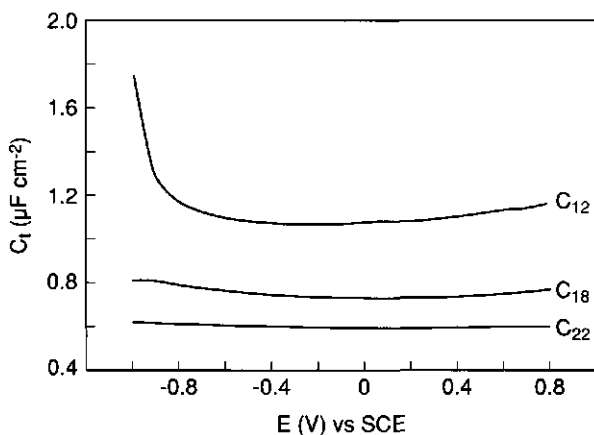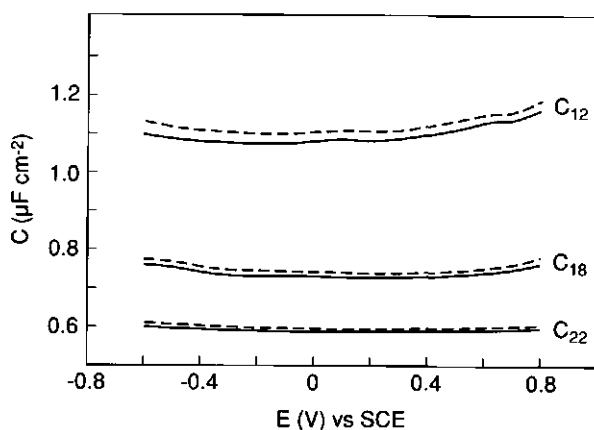

Figure 5.4: Total differential capacitance of a thiol ($C_nH_{2n+1}SH$)–modified gold electrode in 10^{-2} M K_2SO_4 ($n = 12,18,22$). The scan rate was 10 mV s^{-1}.

Both the cathodic current and the capacitance increase in value when the potential goes negative beyond about –0.6 V(SCE). The effect becomes more pronounced with decreasing chain length. The increasing current and hence the increasing capacitance for potentials below –0.6 V(SCE), is probably caused by faradaic currents due to the reduction of hydrogen. As can be seen in Figures 5.3 and 5.4, the reduction kinetics of the H^+/H_2 couple depend strongly on the length of the thiol. The dielectric barrier becomes more effective as the number of methylene groups increases.

In the region where no faradaic current flows (between about –0.6 and 0.8 V(SCE); the double layer region), the measured capacitance is almost independent of the potential. The capacitance depends strongly on the chain length: the longer the chain, the lower the capacitance. The value of the capacitance of the thiol layers with varying chain length is similar to that from other impedance measurements [16,17]. When C_t is determined from capacitive currents, a somewhat higher value was found [3,5,18–20]. The latter method is probably more sensitive to small faradaic currents, resulting in a higher apparent

capacitance.

With the procedure given in the theoretical section, the capacitance of the thiol layer C_i was calculated from C_t as a function of the electrode potential. The results, together with the measured capacitance C_t are given in Figure 5.5. The C_i and C_t values are shown for the double layer region only. Outside this region, faradaic currents prohibit proper calculation of C_i. Due to the relatively high diffuse double layer capacitance, C_i is only slightly larger than C_t. When calculated with the Poisson–Boltzmann equation [10,11], C_d has a minimum value of 35.5 μF cm^{-2} in 10^{-2} M K$_2$SO$_4$.

Figure 5.5. The measured total differential capacitance C_t (———) and the derived capacitance of the thiol layer C_i (---) of a thiol (C$_n$H$_{2n+1}$SH)–modified gold electrode in 10^{-2} M K$_2$SO$_4$ (n = 12,18,22).

Within experimental error C_i is potential-independent and is a function of the thickness of the thiol layer only (equation 5.10). This indicates that potential-induced conformational changes of the thiol layer do not seem to occur. It should be noted that the C_i values given in Figure 5.5 include the capacitance of the Stern layer at the thiol/electrolyte interface. Therefore the true value of the capacitance of the thiol layer may be slightly higher. From ellipsometry in air, the thickness of these thiol layers is known [4]. These values are given in Table 5.1. The values of ε_r can be calculated from equation 5.10, using the values for

C_i from Figure 5.5 and the literature values for δ. The value for δ in our electrochemical system, where the thiols are in an aqueous environment, may differ from the thickness in air. For example, penetration of electrolyte in small defects in the thiol layer may swell the layer, thereby increasing δ and herewith increasing the calculated value of ε_r. It is evident, however, that ε_r is low (compare $\varepsilon_r = 2.3$ for polyethylene), illustrating the dielectric character of the thiol layer. This low permittivity is found for all chain lengths, except for the alkyl thiol chains shorter than about 11 carbon atoms, because the shorter chains were not stable in the electrochemical environment of our experiments. These results are in agreement with results obtained by other researchers, using other techniques [3,4,21]. The constant dielectric properties imply that the chemical structure of the thiol layer is independent of the chain length for these alkyl thiol chains. A similar chemical structure for the different alkyl thiols does not exclude the presence of any defects in the thiol layer. When defects are present, their influence is smeared out and affects both ε_r and δ, and thus C_i.

5.3.3. Comparison of capacitance and wetting measurements: influence of thiol chain length

The surface charge density as a function of the potential can be determined with the procedure given in the introduction (equation 5.5). The results of this procedure in the double layer region are given in Figure 5.6. At the ecm, the surface charge is set zero (specific adsorption is assumed to be absent). The ecm is obtained from the tensiogram in Figure 5.2. The values found for $\sigma_0(E)$ are relatively low due to the dielectric character of the thiol layers. The curves have a slope C_t (equation 5.5). Because C_t is almost potential independent in the region shown, σ_0 is an almost linear function of E. The potential that remains at the thiol/electrolyte interface is at most 3% of the applied potential ψ_0 for the C_{12}–thiol and only 1.5% of ψ_0 for the C_{22}–thiol.

The electrostatic part of the interfacial tension $\Delta\gamma_{SL}^{el}(E)$ is obtained by graphical integration of the curves in Figure 5.6 according to equation 5.11 (Figure 5.7).
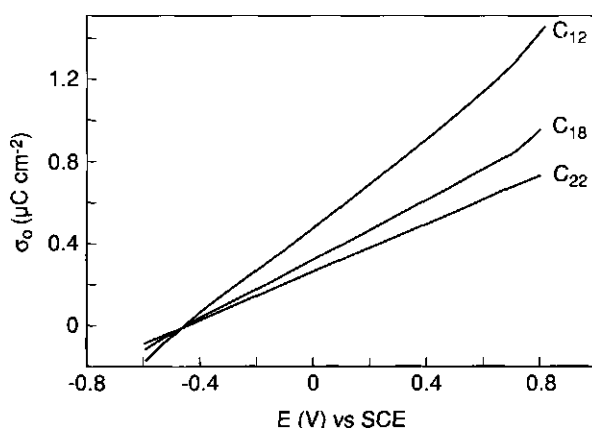
Figure 5.6: Surface charge density of a thiol $(C_nH_{2n+1}SH)$–modified gold electrode in 10^{-2} M K_2SO_4 (n = 12,18,22).

Because C_t is virtually independent of the potential, the Helmholtz energy of double layer formation may, to a good approximation, be written as

$$\Delta F_d = \Delta\gamma_{SL}^{el} \cong -\tfrac{1}{2}C_t(E-E_e)^2 \qquad (5.12)$$

This mathematical integration of a constant C_t results in a nearly identical curve (not shown). The potential-dependent part of the interfacial tension can also be measured directly with our wetting method. The change in γ_{SL} found in this way, is the sum of the change in the electrostatic part of γ_{SL} (due to double layer formation) and of the change in the chemical part of γ_{SL} (due to orientational changes of the molecules in the thiol layer, if any, resulting in a change in composition of the thiol/electrolyte interface). The results of both methods are compared in Figure 5.7. The curves are parabolic in shape, and both sets of results are very similar; the same sequence of the curves for the different thiol chain lengths is found. However, the fit is not perfect. Assuming that both measurements are made under equilibrium conditions, the agreement should be perfect if the change in interfacial tension were purely electrostatic. Whether the small deviations observed in our experiments are due to non–equilibrium effects in the wetting measurement or caused by a slight chemical change of the thiol/solution interface due to the applied potential is hard to say. Our results
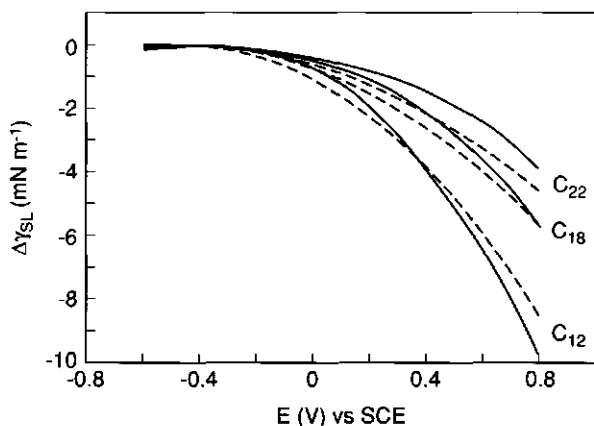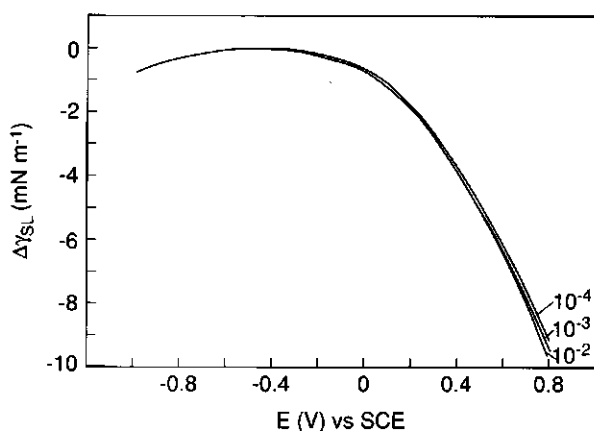
Figure 5.7: Potential–dependent change of the surface tension of the gold/thiol $(C_nH_{2n+1}SH)$/electrolyte interface in 10^{-2} M K_2SO_4 directly measured with the Wilhelmy plate method (——) and indirectly measured via the capacitance (---) $(n = 12,18,22)$.

indicate, however, that such changes in the chemical component of the interfacial tension, may they occur, do not make a significant contribution.

5.3.4. Comparison of capacitance and wetting measurements: influence of ion concentration

In order to verify the double layer model as proposed in the previous section, the effect of the indifferent electrolyte concentration was tested. The tensiograms for C_{12}–thiol measured in 10^{-2}, 10^{-3}, and 10^{-4} M K_2SO_4 respectively, are given in Figure 5.8. The standard deviation is ±5%. The ecm, at –0.45 V(SCE), coincides for all ion concentrations. As expected, small hydrophilic ions like K^+ and SO_4^{2-} do not seem to adsorb specifically on the hydrophobic thiol surface, because specific adsorption would have shifted the ecm. The trend is found that $\gamma(10^{-2})>\gamma(10^{-3})>\gamma(10^{-4})$ although the difference between the respective curves is extremely low. For C_{18}–thiol and C_{22}–thiol (not shown) no effect of the ion concentration was observed.

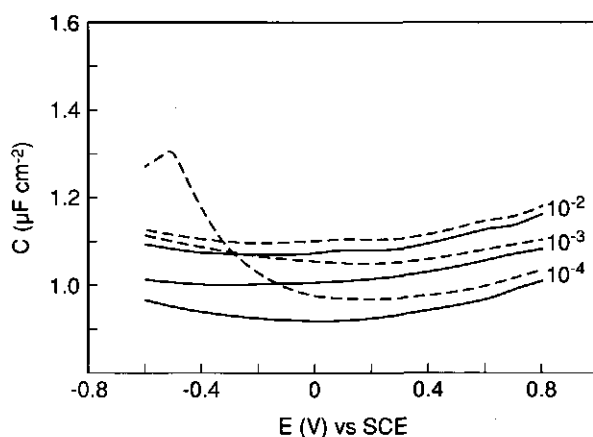The differential capacitance measured at the different K_2SO_4 concentrations is

Figure 5.8: Potential–dependent change of the surface tension of the gold/$C_{12}H_{25}SH$/electrolyte interface in 10^{-2}, 10^{-3} and 10^{-4} M K_2SO_4 measured with the Wilhelmy plate method. The scan rate was 10 mV s^{-1}.

given in Figure 5.9. The difference between the total differential capacitances measured at 10^{-2}, 10^{-3}, and 10^{-4} M K_2SO_4 for a C_{12}–thiol was only small but always according to $C_t(10^{-2})>C_t(10^{-3})>C_t(10^{-4})$. When the capacitance in the respective concentrations was measured on one single modified electrode, this sequence was also reproducibly found. Although less obvious, it was also found that for C_{18} and C_{22}–thiols the total capacitance measured was higher in 10^{-2} M
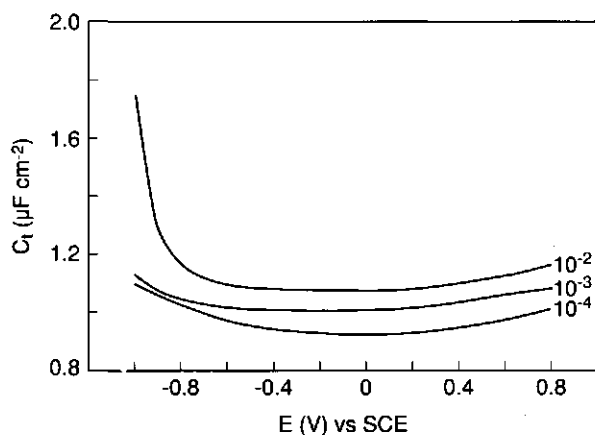
Figure 5.9: Total differential capacitance of a $C_{12}H_{25}SH$–modified gold electrode in 10^{-2}, 10^{-3}, and 10^{-4} M K_2SO_4. The scan rate was 10 mV s^{-1}.

Figure 5.10: The measured total differential capacitance C_t (——) and the derived capacitance of the thiol layer C_i (---) of a $C_{12}H_{25}SH$–modified gold electrode in 10^{-2}, 10^{-3}, and 10^{-4} M K_2SO_4.

K_2SO_4 than in 10^{-4} M K_2SO_4 (results not shown).

The C_i values calculated as a function of E from C_t with equation 5.8 are given in Figure 5.10. Mainly for the lower concentrations (10^{-3} and 10^{-4} M), in the neighbourhood of the potential where C_d is minimal, does C_d influence the calculated value of C_i. For the lowest electrolyte level, C_d calculated from the Gouy–Chapman model reaches a minimum of 3.55 μF cm^{-2} at $E = -0.515$ V(SCE). Because this value is of the same order of magnitude as the measured C_t, the calculated C_i values are strongly affected by the exact value of C_d around this potential. This effect, although less pronounced, is also found for 10^{-3} M K_2SO_4 where the minimal C_d is 11.2 μF cm^{-2} (at $E = -0.640$ V(SCE)). From the deviation between the measured C_t and calculated C_i, it seems that the diffuse part of the double layer does not exactly follow the Gouy–Chapman equation. This may also explain why C_i remains slightly electrolyte concentration-dependent.

By double integration of C_t to E according to equation 5.11, $\Delta\gamma_{SL}^{el}(E)$ is obtained (Figure 5.11). The $\Delta\gamma_{SL}(E)$ curves obtained from the capacitance and from the wetting measurements differ significantly (in 10^{-3} M and 10^{-4} M K_2SO_4),
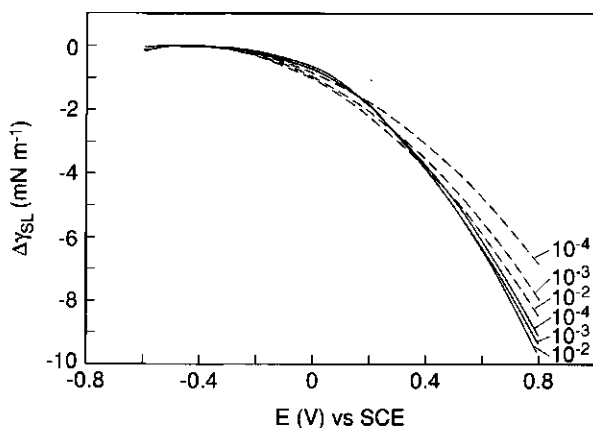
Figure 5.11: Potential-dependent change in the surface tension of the gold/$C_{12}H_{25}SH$ interface in 10^{-2}, 10^{-3} and 10^{-4} M K_2SO_4 directly measured using the Wilhelmy plate method (———) and indirectly measured via the capacitance (---).

although the same trends are found: the potential dependency of γ_{SL} is more distinct for larger ion concentrations. This is in agreement with double layer theory: at high electrolyte levels the screening of the potential is more effective, resulting in a higher charge density and double layer Helmholtz energy. Considering our conclusion in the previous paragraph, it seems unlikely that the differences between the respective curves in Figure 5.11 can be explained by the role of potential-induced orientational changes. Rather, the differences may be caused by the different nature of both methods. The measured capacitance is an average thiol film property. The wetting measurements refer to the surface properties in the three phase boundary in the meniscus. Because all the processes take place in this small and constantly moving area, it is likely that the wetting measurements do not refer to the perfect equilibrium condition.

It is encouraging to find in the capacitance measurements a salt effect that is consistent with our simple representation of the interphase as a dielectric (thiol) layer and a diffuse layer in the electrolyte: the diffuse potential is more effectively screened by raising the electrolyte level and the charge may, thus, further increase.

5.4. Conclusions

Comparing the potential-dependent change of the interfacial tension $\Delta\gamma_{SL}$ of thiol-modified gold electrodes in K_2SO_4 directly measured with the Wilhelmy plate method with $\Delta\gamma_{SL}$ indirectly obtained from the capacitance measurements shows that the results are in reasonable agreement with each other. This is a gratifying result given the completely independent nature of both methods.

Indications for an effect of the potential on the conformation of the adsorbed thiol molecules on gold are not found:
–The capacitance of the thiol layer is found to be practically potential–independent: the capacitance only depends on the thickness and permittivity of the thiol layer.
–The agreement between $\Delta\gamma_{SL}$ obtained from the wetting measurement and from the capacitance measurement points to negligible potential–induced chemical changes of the thiol/solution interface.
Therefore, it is concluded that the sole origin of the potential dependence of wetting is the formation of an electric double layer at the thiol/solution interface.

The potential-dependent change of γ_{SL} of thiol-modified gold electrodes depends strongly on the chain length: the shorter the chain the stronger the influence. A simple representation of the double layer as a dielectric thiol layer and a diffuse double layer in the electrolyte accounts well for the observed chain length effect. The salt concentration dependence of the total capacitance can be qualitatively understood with the model. The salt effect on the potential-dependent wetting is less than theoretically expected, presumably due to the fact that the wetting measurements are not made under perfect equilibrium conditions.

The electrocapillary maximum is situated at about –0.45 V(SCE). This value is neither influenced by the chain length of the thiol molecules nor influenced by the electrolyte concentration. From the latter it is concluded that specific adsorption of ions on the hydrophobic thiol surface does not occur.

The permittivity of the thiol layer is low and independent of the thiol chain length: $\varepsilon_r{\sim}2$. This low and chain length–independent dielectric behaviour implies that the thiol molecules are densely packed and well–ordered and that the chemical structure of the thiol layer is independent of the chain length.

Our conclusions refer to alkyl thiols of chain length longer than 10 carbon atoms. The shorter chains were found to desorb under the influence of an electrochemical potential, due to the less ordered structure of the layers.

Monolayer-modified electrodes such as those studied in the present chapter have wide potential as model systems, for example in metal deposition studies [22,23]. The effect of metal atom–substrate interactions in the initial stages of phase formation on the geometry of nuclei can thus be studied in detail. We will report on these aspects in chapter 8.

This study has shown that potential-dependent wetting experiments in combination with capacitance measurements and voltammetry offer a powerful tool in the characterization of electrical double layers at self-assembled thiol-modified electrodes.

References

[1]   Sondag–Huethorst, J.A.M.; Fokkink, L.G.J. *Langmuir* **1992**, *8*, 2560–2566 and chapter 4, this thesis and references cited therein.
[2]   Ulman, A. *An Introduction to Ultrathin Organic Films from Langmuir–Blodgett to Self–Assembly*; Academic Press: San Diego, 1991; Chapter 3.
[3]   Porter, M.D.; Bright, T.B.; Allara, D.L.; Chidsey, C.E.D. *J. Am. Chem. Soc.* **1987**, *109*, 3559–3568.
[4]   Bain, C.D.; Throughton, E.B.; Tao, Y.-T.; Evall, J.; Whitesides, G.M.; Nuzzo, R.G. *J. Am. Chem. Soc.* **1989**, *111*, 321–335.
[5]   Miller, C.; Cuendet, P.; Graetzel, M. *J. Phys. Chem.* **1991**, *95*, 877–886.
[6]   Beni, G; Hackwood, S. *Appl. Phys. Lett.* **1981**, *38*, 207–209.
[7]   Chapter 8, this thesis and references cited therein.
[8]   Fokkink, L.G.J.; Ralston, J. *Colloids Surf.* **1989**, *36*, 69–76.
[9]   Verwey, E.J.; Overbeek, J.Th.G. *Theory of stability of lyophobic colloids*; Elsevier: Amsterdam, 1948.

[10] Delahay, P. *Double Layer and Electrode Kinetics*; John Wiley: New York, 1965.

[11] Lyklema, J. *Fundamentals of Interface and Colloid Science*; Academic Press: London, 1991.

[12] Dubois, L.H.; Zegarski, B.R.; Nuzzo, R.G. *J. Chem. Phys.* **1993**, *98*, 678–688.

[13] Walczak, M.M.; Chung, C.; Stole, S.M.; Widrig, C.A.; Porter, M.D. *J. Am. Chem. Soc.* **1991**, 2370–2378.

[14] Kim, Y.-T.; Bard, A.J. *Langmuir* **1992**, *8*, 1096–1102.

[15] Edinger, K.; Gölzhäuser, A.; Demota, K.; Wöll, Ch.; Grunze, M. *Langmuir* **1993**, *9*, 4–8.

[16] Sabatini, E.; Rubinstein, I.; Maoz, R.; Sagiv, J. *J. Electroanal. Chem.* **1987**, *219*, 365–371.

[17] Matsushita, F.; Miyaoka, S.; Ikeda, T.; Senda, M. *Analytical Sciences* **1991**, *7*, 1685–1688.

[18] Widrig, C.A.; Chung, C.; Porter, M.D. *J. Electroanal. Chem.* **1991**, *310*, 335–359.

[19] Finklea, H.O.; Lynch, M. *Langmuir* **1987**, *3*, 409–413.

[20] Chidsey, C.E.D.; Loiacono, D.N. *Langmuir* **1990**, *6*, 682–691.

[21] Evans, S.D.; Ulman, A. *Chem. Phys. Let.* **1990**, *170*, 462–466.

[22] Smith, E.L.; Alves, C.A.; Anderegg, J.W.; Porter, M.D. *Langmuir* **1992**, *8*, 2707–2714.

[23] Tarlov, M.J. *Langmuir* **1992**, *8*, 80–89.

Chapter 6

Electrochemical characterization of functionalized alkanethiol monolayers on gold[1]

Abstract: The stability of functionalized alkanethiol monolayers ($HS(CH_2)_{n-1}X$, with X = CH_3, OH, CN, Cl ($n = 12$) and $X = COOH$ ($n = 11$)) adsorbed on polycrystalline gold electrodes is investigated with capacitive current, differential capacitance and electrowetting measurements in indifferent electrolyte. It is found that these monolayers are highly stable upon cycling of the modified electrode in a potential region where only double layer charging occurs. The COOH–terminated thiol monolayer is electroactive. The carboxyl group can in part (5–10% of a monolayer) be cathodically reduced, giving the corresponding aldehyde. Occasionally, the reduction is followed by a second step giving a methyl-hydroxyl group. Reduction and oxidation occurs without destabilizing the thiol monolayer. The difference in the capacitance C_X of the thiol monolayers with terminal group X is determined by the dielectric properties of this group and increases in the following sequence: $C_{CH3} < C_{Cl} < C_{OH} < C_{CN}$. No indications are found that C_X is affected by a difference in ordering or in packing density of the molecules, except for $X = COOH$. In that case the bulkiness of the COOH group influences the ordering and packing of the monolayer, leading to a relatively high capacitance. The potential E_e in the electrocapillary maximum of the functionalized thiol monolayer can be obtained from electrowetting measurements. The sequence found is $E_e^{CH3} < E_e^{Cl} < E_e^{CN} < E_e^{OH}$. The differences in E_e are ascribed to the different dipole moments of the terminal group X. From the electrowetting measurements, in combination with interfacial thermodynamics it is concluded that the "chemical" component of the interfacial tension of the thiol/electrolyte is a function of the applied potential for X = CN, OH and Cl. This is interpreted as a change in the orientation of the molecules, which attempt to align the dipoles parallel to the direction of the electric field across the thiol layer.

6.1. Introduction

This chapter describes the electrochemical characterization and the potential-dependent wettability of monolayer films formed through adsorption of long–chain alkanethiols on gold. Alkanethiol molecules ($HS(CH_2)_{n-1}CH_3$) are known to form densely packed and highly ordered monolayers on various metals [1–7] and even on semiconductors such as GaAs [8]. The density of packing and the tilt angle of the molecules in the monolayer is influenced by the type [9,10] and texture [11,12] of the metal substrate. As demonstrated with diffraction techniques [13–16] and with STM [3,17], the adsorbed sulphur groups are ordered at room temperature in the commensurate ($\sqrt{3}x\sqrt{3}$)R30° Au–overlayer structure. From helium diffraction studies [13] it is known that the tail ends of the thiol molecules on Au (111) are ordered at low temperature (<100 K) and become disordered at room temperature due to thermal motion. The molecules are tilted on this Au(111) surface by an average angle of about 30° with respect to the surface normal [5,12,18]. The packing is not only influenced by the underlying substrate, but also by a terminal group X of the substituted alkanethiol ($HS(CH_2)_{n-1}X$). As long as X is relatively small (e.g., NH_2 or OH), the structure of the monolayer is dominated by the Van der Waals interactions among hydrocarbon chains and not by X [12,19]. When X is bulky (e.g., F, COOH or ferrocene), the density of packing and the ordering becomes less [19–21]. Substituted thiols have been used in several wetting and adsorption studies. From these studies it was found that despite the presence of the terminal groups the sulphur–gold bonding always occurs and that in all cases the terminal groups are located at the outer surface [4,19,22].

The present chapter is the third dealing with the potential-dependent wetting of thiol-modified polycrystalline gold electrodes. In chapter 4, we described a Wilhelmy plate technique to measure the wettability of the hydrophobized gold electrodes as a function of the electrode potential (electrowetting). In chapter 5 this technique was used to determine the electrowettability and electrochemical properties (such as the differential capacitance) of the modified electrodes as a function of the thiol chain length and the electrolyte concentration. The chain

length n was varied between 12 and 22, with $X = CH_3$. It was found that the electrowetting properties of these monolayers can be conveniently described by interfacial thermodynamics. It was concluded that the dependence of the wettability on the electrode potential originates from the formation of an electrical double layer at the electrolyte side of the thiol/electrolyte interface. Potential-induced conformational changes within the alkanethiol monolayer on gold were found to be insignificant.

In this present chapter we investigate the electrowettability and electrochemical properties of substituted thiol monolayers on gold. Simple functional groups are used to vary the polarity and wettability of the surface. Four adsorbates with a small terminal group are examined here: an unsubstituted alkanethiol $(HS(CH_2)_{11}CH_3)$, a chloroalkanethiol $(HS(CH_2)_{11}Cl)$, a cyanoalkanethiol $(HS(CH_2)_{11}CN)$ and an alcohol–thiol $(HS(CH_2)_{11}OH)$. As the fifth adsorbate a carboxylic acid–thiol $(HS(CH_2)_{10}COOH)$ was selected. The chain length of these molecules is long enough and the size of the terminal group small enough to allow the formation of highly ordered monolayers [19], except for the COOH–terminated thiol which has a bulky end group. The thiol monolayers are characterized by differential capacitance and electrowetting measurements. The model proposed in chapter 5 is used to describe and interpret the results of the electrowetting measurements. This model enables exploration of the effect of the applied electric field across the thiol layer on the conformation of the molecules. The results on the COOH–terminated thiol will be treated separately because the COOH group is electroactive which makes the electrochemical characterization of this monolayer more complicated.

The main purpose of this chapter is to determine how these functionalized alkanethiol monolayers on gold behave under the application of an electrical field. This information is essential if such layers are used as model systems in studies of the influence of the surface energy on the morphology of galvanically deposited metals, as will be discussed in chapter 8. We like to emphasize that the interpretation of some of the measurements presented in this chapter is by necessity speculative. In those cases additional measurements are required in order to establish definite conclusions.

6.2. Experimental

Materials. Details on the materials and preparation of the monolayers can be found in chapter 2. 1–Dodecanethiol ($HS(CH_2)_{11}CH_3$) was obtained from Fluka and used as received. 11–Mercapto-1–undecanol ($HS(CH_2)_{11}OH$), 11–mercaptoundecanoic acid ($HS(CH_2)_{10}COOH$) and 11–chloro-1–undecanethiol ($HS(CH_2)_{11}Cl$) were prepared according to references 23, 24 and 6, respectively. 12–Mercapto-1–dodecanenitrile ($HS(CH_2)_{11}CN$) was prepared from 10–undecen-1–ol in a four step synthesis; all chemicals were obtained from Janssen and used as received. First, the hydroxyl moiety was tosylated according to a literature procedure [25]. Second, nucleophilic substitution of the tosylate by potassium cyanide in DMF at 60°C for 24 h yielded 11–dodecenitrile (88% yield). Third, photochemical addition of thiolacetic acid to the double bond as described for the preparation of 11–chloroundecanethiol [6] gave 12–thioacetyldodecanitrile (80% yield). Fourth, deacetylation in degassed methanol with potassium carbonate as described for the preparation of 11–chloroundecanethiol produced 12–mercaptododecanitrile (85% yield).

Potential-dependent contact angle and electrochemical measurements. Details of the experimental set-up are given in chapter 4. This set-up consists of a thiol-modified (Wilhelmy) gold plate suspended on a wire in a bottom–loading balance (Mettler PM2000). The Wilhelmy plate is the working electrode in a three–electrode configuration which allows potentiostatic control (with a Schlumberger 1186 EI/Hi–Tek Instruments PP RI potentiostat). The scan rate was 10 mV s^{-1} (and incidently 1 mV s^{-1}). The potentiostat is coupled to a frequency response analyzer (FRA; Schlumberger Solartron 1170). The FRA supplies an ac signal with a frequency of 10 Hz and an amplitude of 10 mV to the Wilhelmy plate working electrode, which is partly immersed in a deaerated aqueous solution of 10^{-2} M K_2SO_4. The set–up enables simultaneous measurement of the change in mass Δm associated with the electrolyte meniscus rise, of the capacitive current, and of the differential capacitance as a function of applied potential E. The change in mass results from alterations in solid/liquid interfacial tension $\Delta\gamma_{SL}$ [1,2]. In the next section the values of $\Delta\gamma_{SL}$ as calculated

from Δm [1] are given. Only the results for the advancing meniscus are presented. The receding meniscus showed a similar dependence on the potential [1].

The experiments were carried out at 25°C. The surface tension γ_{LV} of the electrolyte solutions was about 72 mN m^{-1}. The reagents were analytical grade (Merck). The results given in Figures 6.1, 6.2 and 6.4 display the average values of at least 4 measurements.

6.3. Results and discussion

6.3.1. Electrochemical measurements

The type of terminal group X (where X = OH, COOH, CN, Cl or CH$_3$) of a thiol HS(CH$_2$)$_{11}$X adsorbed on gold affects the potential-dependent wetting and capacitance of these layers. In all cases, except for COOH, the backbone contained 11 carbon atoms. For X=COOH this number was 10 (i.e., HS(CH$_2$)$_{10}$COOH). The advancing (θ_a) and receding (θ_r) contact angles measured with water (standard deviation ±3°) and other characteristics of the thiol layers are given in Table 6.1. Because the carboxyl thiol behaves distinctly different from the other thiols, this type of monolayer will be treated separately in a following section.

The capacitive current, measured simultaneously with the differential capacitance and the potential-dependent wetting, does not differ significantly for the individual terminal groups. At a potential negative of about –0.6 V(SCE), the cathodic current starts to increase due to hydrogen evolution. Between about –0.6 and 0.7 V(SCE) the current is only due to double layer charging.

The results of the differential capacitance measurements are given in Figure 6.1 and Table 6.1. The capacitance is independent of the scan direction. The average values of scans in anodic and cathodic direction are given. The standard
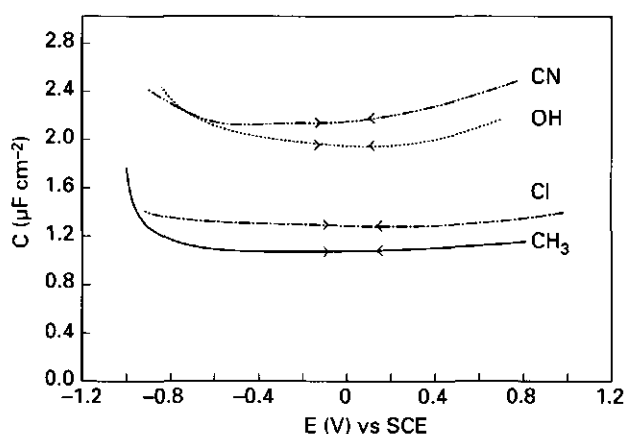
Figure 6.1: Total differential capacitance of a $HS(CH_2)_{11}X$-modified gold electrode in 10^{-2} M K_2SO_4. The scan rate was 10 mV s^{-1}. The type X of terminal group is indicated in the figure.

deviation of these measurements is within ±5%. The capacitance is nearly independent of the potential in the potential region where only double layer charging occurs. Outside the regions given in Figure 6.1 the monolayers are found to be disrupted.

Although the chain length of the adsorbed thiols with different terminal groups is nearly the same, the capacitance is found to be a function of the type of terminal group (Table 6.1 and Figure 6.1). We assume that the total capacitance C_t (per unit area) is given by the capacitance C_i of the thiol layer and the capacitance C_d of the diffuse part of the electrical double layer in series [2]. For the relatively high electrolyte concentration of 10^{-2} M, C_t approximately equals the capacitance of the thiol layer C_i:

$$C_t \approx C_i = \frac{\varepsilon_0 \varepsilon_r}{\delta} \qquad (6.1)$$

where ε_0 is the permittivity of vacuum, ε_r the relative dielectric constant of the thiol layer, and δ its thickness.

The sequence of decreasing capacitance is $C_{CN} > C_{OH} > C_{Cl} > C_{CH3}$. A similar

sequence was also found by Chidsey [19]. Clearly, the capacitance is affected by the terminal group. This may be caused by a difference in ordering and density of packing of the thiol monolayer induced by the terminal group. A disordered monolayer will less effectively prevent water and ions from penetrating into the monolayer. If such penetration would occur, this would result in a higher relative dielectric constant and, consequently, in a higher capacitance. However, no indications for less dense packing and disorder are found: the capacitance as a function of the scanning potential is highly reversible for every terminal group studied. If water would penetrate in the monolayer, hydrolysis of water at the Au–thiol interface might disrupt this layer, which would lead to an (irreversibly) increasing capacitance during scanning. Moreover, infrared spectroscopy [19] has shown that the alkanethiol, alcohol–thiol and cyano–thiol monolayers have a nearly crystalline packing. Therefore, it is not likely that a different ordering due to the terminal group causes these differences in capacitance.

Table 6.1: Characteristics of functionalized thiol $(HS(CH_2)_{11}X)$ monolayers adsorbed on polycrystalline gold in 10^{-2} M K_2SO_4.

| X	θ_a [†] (deg)	θ_r [†] (deg)	E_e V(SCE)	C_t (μF cm^{-2})	δ (nm)	ε_r $HS(CH_2)_{11}X$	ε_r [‡] CH_3CH_2X
CH_3	112	88	−0.5	1.1	1.53	1.8	1.61
Cl	95	80	+0.1	1.3	1.47	2.1	9.45
OH	24	<5	+0.5	1.9	1.52	3.3	24.3
CN	69	51	+0.2	2.1	1.56	3.7	27.2
COOH[*]	45	<5	?	2.1	1.52	3.5	3.44

[†]measured with water
[‡]from ref. 26
[*]$HS(CH_2)_{10}COOH$

Most likely the differences in capacitance are due to the differences in dielectric

behaviour of the terminal groups. In order to be able to compare ε_r of the various X–terminated monolayers, ε_r was calculated with equation 6.1. First, the thickness of the monolayer δ was calculated. This is done by using known bond lengths and bond angles [27], assuming the contribution of S^- to the total thickness of the monolayer to be 0.15 nm and the tilt angle of the molecules to be 30° [6]. The results for δ and ε_r are given in Table 6.1. The sequence found for ε_r of the thiol monolayers is the same as that for substituted alkanes in bulk, which strongly suggests that indeed the dielectric properties of the terminal groups largely determines the capacitance of the monolayer. An exception forms the COOH–terminated monolayer. The cause of this exception will be discussed in paragraph 6.3.4. For comparison, ε_r of substituted ethanes (CH_3CH_2X [26]) is included in Table 6.1.

6.3.2. Tensiometry

The tensiograms for the different terminal groups are given in Figure 6.2. The curves represent the average of at least 5 measurements; standard deviation of the average is below ±5%. For most of the curves in Figure 6.2 the shape is not parabolic, which is expected for systems where the potential dependency is dominated by the electrostatic effect [1,2], like for mercury. The potential E_e at the maximum of the curve is usually referred to as the electrocapillary maximum (ecm). This potential is the potential at which the surface charge is zero [1,2] and is also referred to as the potential of zero charge. The values of E_e are tabulated in Table 6.1. At E_e, the advancing contact angle with water is equal to the advancing contact angle determined with water by the sessile drop method. The maximum of the curve shifts in the anodic direction with increasing hydrophilicity of the thiol-modified gold substrate: $E_e^{CH3}<E_e^{Cl}<E_e^{CN}<E_e^{OH}$. It is not likely that specific adsorption of the cation K^+ causes this variation in E_e because this cation is not expected to adsorb on the rather hydrophobic substrates. Moreover, similar values for E_e were found when using H_2SO_4 or KOH as the electrolyte. Therefore, we assume the difference in potential of zero charge to be caused by the intrinsic properties of the monolayers. As demonstrated in the
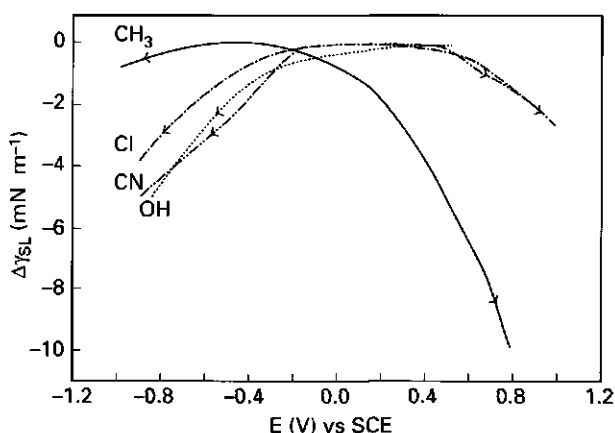
Figure 6.2: Potential-dependent change of the surface tension of the gold/thiol ($HS(CH_2)_{11}X$) electrolyte interface in 10^{-2} M K_2SO_4 measured using the Wilhelmy plate method. The scan rate was 10 mV s^{-1}. The type X of terminal group is indicated in the figure.

previous section there are no indications that the ordering of the monolayer is influenced by the terminal group. Hence, the difference in E_e must be due to the type of terminal group.

The potential drop across the electrical double layer may be decomposed in a potential drop associated with free charges at the gold/thiol interface (ionic contribution) and a potential drop due to dipoles in the monolayer (dipole contribution) [28]. At the potential of zero charge the potential drop associated with the free charges is by definition zero [28]. In this case, the potential drop is determined by the dipole moment of the monolayer. The dipole contributes to a positive surface potential if the positive end of the dipole points to the gold/thiol interface. This is the case for the Cl, CN, and OH terminal groups. Due to the electronegativity of Cl, N and O, a small negative charge resides at these atoms. This charge is compensated by a positive charge on the carbon and/or hydrogen in contact with the electronegative atom. Hence, at the point of zero charge, the potential is positive with respect to the potential of zero charge of the CH$_3$–terminated monolayer, where only a very small dipole moment is present in the terminal group. According to the sequence found for the potential of zero charge, the dipole contribution should increase in the order

CH_3>Cl>CN>OH. One of the factors determining the dipole moment is the electronegativity of the atoms. Indeed, the sequence of increasing E_e follows the sequence of increasing electronegativity of the atoms in the terminal group: C<Cl<N<O [29]. Therefore, there is a strong indication for the influence of the dipole moment on the potential of zero charge of gold covered with a X–terminated thiol monolayer.

One might have expected that this sequence would also apply for the dielectric constant of the monolayer because of the correlation between the dipole moment and the dielectric constant [30]. However, ε_r given in Table 6.1 is the value for the entire monolayer whereas the dipole moment as discussed above refers to the terminal group only. This may cause the difference in sequence between ε_r and E_e. In addition, other factors than the dipole moment might determine ε_r. For example, the packing density of the molecules in the monolayer could differ slightly for the various monolayers investigated.

6.3.3. Comparison of capacitance and wetting measurements for electroinactive terminal groups (Cl, CN, OH, and CH_3)

In chapters 4 and 5 a model was presented to explain the influence of the potential on the wetting behaviour of the alkanethiol-modified gold electrodes. In this model, the double layer of the alkanethiol-modified gold electrode in an indifferent electrolyte is subdivided in a dielectric thiol layer and a diffuse double layer in the electrolyte. This model leads to a correlation between the capacitance and the potential-dependent wetting. The latter property is expressed in terms of the change in the electrical component of the interfacial tension $\gamma_{SL}{}^{el}$ of the solid/liquid interface. In chapter 5 we derived the following relation:

$$\Delta\gamma_{SL}{}^{el} = -\int\int C_i (d(E-E_e))^2 \tag{6.2}$$

where E is the applied electrode potential and E_e is the potential of the electrocapillary maximum.

The change in the electrical component of the interfacial tension results from a change in the distribution of ions in the electrolyte upon variation of the potential. The absolute value γ_{SL} of the solid/liquid interfacial tension is, in first approximation, taken to consist of an electrical (potential-dependent) component γ_{SL}^{el} and a "chemical" (i.e., potential-independent) component γ_{SL}^{0}:

$$\gamma_{SL}(E) = \gamma_{SL}^{0} + \gamma_{SL}^{el}(E) \qquad (6.3)$$

The chemical component γ_{SL}^{0} is the intrinsic interfacial tension. This chemical component is only constant if potential-induced changes of the monolayer do not occur. From equation 6.3, the change in γ_{SL}^{0}, $\Delta\gamma_{SL}^{0}$, can be calculated from direct measurements of $\Delta\gamma_{SL}(E)$ with a Wilhelmy plate balance, and comparing these results with $\Delta\gamma_{SL}^{el}$ obtained from the capacitance measurements (equation 6.2). Both $\Delta\gamma_{SL}^{el}$ and $\Delta\gamma_{SL}$ are changes with respect to γ_{SL} in the electrocapillary maximum. From the comparison between $\Delta\gamma_{SL}$ and $\Delta\gamma_{SL}^{el}$ it can be concluded whether or not γ_{SL}^{0} is independent of the potential. For the alkanethiol-modified gold electrodes it was found that $\Delta\gamma_{SL}^{el}$ obtained from the capacitance measurements and $\Delta\gamma_{SL}$ obtained from the direct Wilhelmy plate measurements are in excellent agreement, and it was therefore concluded that the potential has no effect on the conformation of the adsorbed molecules [2], hence, $\Delta\gamma_{SL}^{0}=0$.

Comparing the results of $\Delta\gamma_{SL}$ obtained from the wetting method and $\Delta\gamma_{SL}^{el}$ obtained from the capacitance for the alkanethiol substituted with different terminal groups, it is found that both sets of results deviate. In all cases the effect of the potential on $\Delta\gamma_{SL}$ is much less than the effect determined from the capacitance measurements. In Figure 6.3 the difference between $\Delta\gamma_{SL}$ determined with the wetting method and $\Delta\gamma_{SL}^{el}$ determined with the capacitance method is given as a function of the potential. A strong effect of the hydrophilicity of the thiol on $(\Delta\gamma_{SL} - \Delta\gamma_{SL}^{el})$ is found: the more hydrophilic the stronger the effect.

According to our model, $(\Delta\gamma_{SL} - \Delta\gamma_{SL}^{el})$ equals $\Delta\gamma_{SL}^{0}$ (equation 6.3). A change of $\Delta\gamma_{SL}^{0}$ as a function of the potential is only possible if the intrinsic interfacial tension is influenced by the potential, for example through a change in rotation or tilt angle of the molecules. In that case the capacitance of the thiol layer may
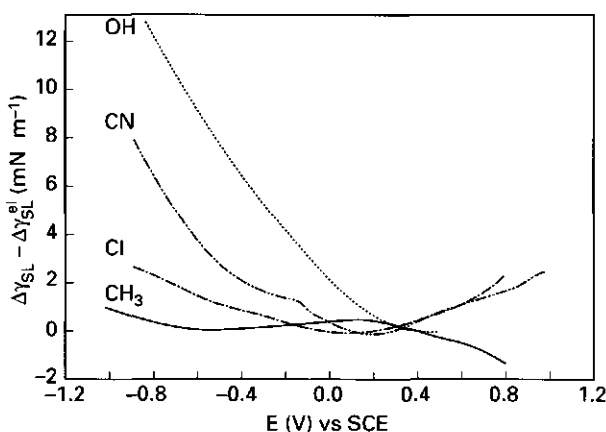
Figure 6.3: Difference between $\Delta\gamma_{SL}$ as given in Figure 6.1 and $\Delta\gamma_{SL}^{el}$ determined with the capacitance method as a function of the potential in 10^{-2} M K_2SO_4 for a $HS(CH_2)_{11}X$-modified gold electrode. The type X of terminal group is indicated in the figure.

also change due to a change in δ and/or ε_r, but these effects may (in part) compensate each other (equation 6.1). From our capacitance measurements (Figure 6.1), it was deduced that the capacitance was almost independent of the potential. Hence, a change in contact angle as a function of the potential does not necessarily imply that the capacitance of the thiol layer has changed.

We speculate that a change in contact angle as a function of the potential may occur when there is enough space for the molecules to adapt their tilt angle. According to calculations by Ulman [12], an energy minimum is achieved by arranging the monolayer of alkanethiols in a close–packed hexagonal pattern with spacing of ≈0.42 nm and with the molecules normal to the surface. This will only occur if the underlying gold is compatible with such a lattice. For thiols on gold(111), a close–packed structure is obtained for a lattice spacing of 0.497 nm [12]. To maximize the Van der Waals interaction, the molecules tilt by about 30°. This latter value is also experimentally confirmed with infrared spectroscopy [5,18]. However, this value is only an average quantity. At room temperature, the ends of the alkane tails are still disordered [13]. The disordering indicates that there is room for the terminal groups to change their orientation. At our polycrystalline gold electrodes (predominantly (111), (200), and (300)

textured) an even stronger disordering of the tails may occur due to the different tilt angles at domains with different textured gold [11].

A change in the tilt angle of the molecules or in the orientation of the terminal group may be induced by the very strong electric field across the thiol layer ($\approx$ $10^6 - 10^7$ V cm^{-1}). This field tends to align the dipoles and consequently, (part of) the thiol molecules along the field lines to reduce the electrostatic energy [30]. Because the dielectric constant and, hence, the dipole moment of the substituted thiols is larger than that of the alkanethiols, these functionalized molecules are more strongly influenced by the field. The dipole moment perpendicular to the surface may increase when the tilt angle of the molecules or of the terminal groups of the molecules becomes less. As a consequence, the contact angle will change. When the tilt angle is about 30°, the contact angle is mainly determined by the terminal group. When the tilt angle of the molecules is reduced, the underlying CH_2 group may be exposed to the liquid in contact with the monolayer. The wettability of the CH_2 groups is less than that of the CN, OH or Cl groups. Therefore, with decreasing tilt angle, the contact angle increases. The effect of the increase in contact angle will be most pronounced when the difference between the wettability of CH_2 and the terminal groups is large. This explains the sequence OH>CN>Cl>CH_3, as observed in Figure 6.3. A similar influence of the underlying CH_2 on the contact angle was also observed when comparing the (wetting) properties of alkanethiols with an even or uneven number of carbon atoms [4,7,18,31–33]. In case the number of carbons is even, the terminal CH_3–CH_2 bond is oriented perpendicular to the surface whereas for an uneven carbon number the CH_3–CH_2 bond is oriented more parallel to the surface. This difference in orientation influences the wettability of the surface. For alkanethiol modified-gold the wettability with water of the "even" alkanethiol monolayers is worse than those consisting of the "uneven" compounds. This is caused by the fact that in the former case mainly the CH_3 group determines the wettability, whereas in the latter case both CH_3 and CH_2 contribute to the wettability. Because CH_3 groups are slightly less wettable by water than CH_2 groups, the wettability of the even alkanethiol monolayers is less [9,33]. Whether or not the orientation of the molecules does indeed change as a function of the applied potential has to be checked with

independent in–situ measurements. Then the change in orientation could possibly be determined as a function of the potential. Such a technique may be for example infrared spectroscopy. To our knowledge, such studies have not been performed sofar.

6.3.4. Comparison of the capacitance and wetting measurements for the electroactive terminal group COOH

There are two important reasons for treating the carboxyl thiol $(HS(CH_2)_{10}COOH)$ separately from the other thiols. First, the self-assembled structure of the adsorbed carboxyl thiol monolayer is less ordered because the terminal COOH group is relatively bulky [19]. Second, the COOH group is electrochemically active and may be cathodically reduced.

In Table 6.1 the contact angle of water with the COOH–thiol monolayer is given. The contact angle is 45° and is larger than expected. Water is expected to completely wet a COOH covered surface, due to the polarity and hydrogen–bonding capability of the exposed acid functional group. Other researchers [6,19,24,34] found the advancing contact angle with water to vary between 0° and 30°. The cause of the deviation between our results and those of others may be some disorder in our thiol layer. Such disorder will result in some exposure of the underlying CH_2 groups to water and, consequently, in a larger contact angle. Larger contact angles were also found when adsorbing COOH–terminated thiol on Cu [22] or adsorbing dialkylsulfides on gold [24]. Ellipsometry and infrared spectroscopy in the latter case showed these layers to be less ordered [24].

The capacitive current, the differential capacitance and the solid/liquid interfacial tension of gold modified with COOH–terminated thiol as a function of the potential are given in Figure 6.4. On scanning the potential in the cathodic direction, the current and the capacitance show a peak when the potential is between about –0.1 and –0.4 V(SCE). By scanning in the anodic direction, a
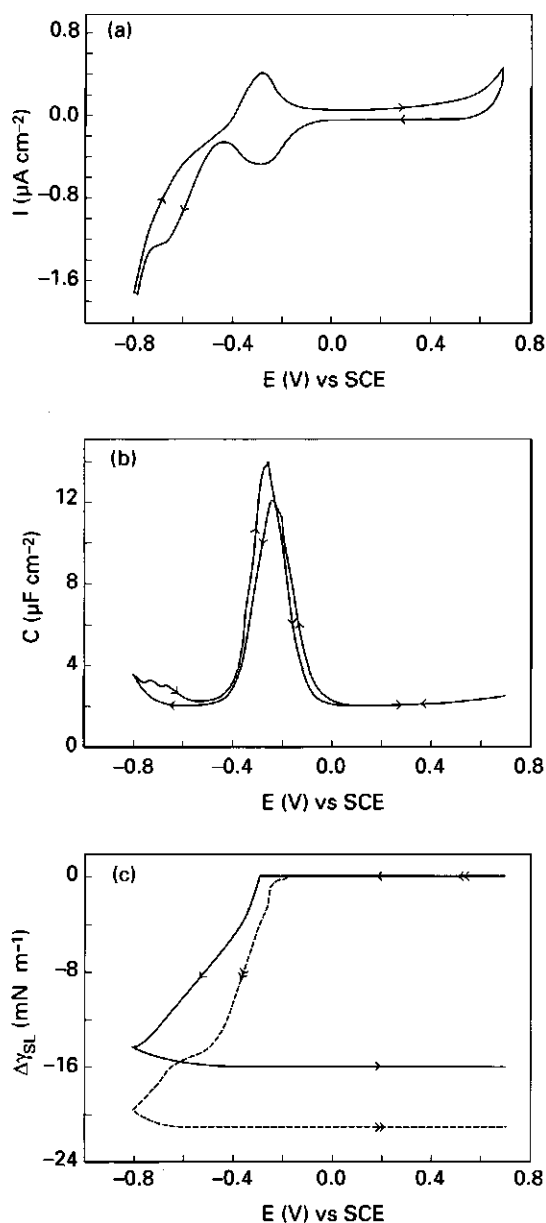
Figure 6.4: The capacitive current (a), the differential capacitance (b) and the interfacial tension (c) of the gold/HS(CH$_2$)$_{10}$COOH electrolyte interface in 10^{-2} M K$_2$SO$_4$, as a function of the applied potential. (a), (b) and (c) are measured simultaneously. The scan rate was 10 mV s^{-1} (solid curves). The interfacial tension was also measured at a scan rate of 1 mV s^{-1} (dotted curve in diagram c).

reversible wave is observed in the cyclic voltammogram. From integration of the area under the peaks, the amount of charge passed can be calculated. This amount is similar for both the anodic and the cathodic scan, and was found to vary between 5 and 15 μC cm^{-2}. This electrode process is not very likely to result from the reduction of protons, formed by dissociation of RCOOH to hydrogen. Reduction of protons would only have resulted in a cathodic peak, whereas no or only a small anodic peak on the return scan would have appeared.

The most likely mechanism for the charge transfer is a cathodic reduction of the carboxyl group according to the following steps:

(1) $R\text{–}COOH + 2H^+ + 2e^- \leftrightarrows R\text{–}CHO + H_2O$
(2) $R\text{–}CHO + 2H^+ + 2e^- \leftrightarrows R\text{–}CH_2OH$
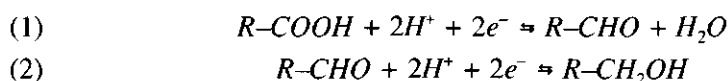
Where R stands for $Au\text{–}S\text{–}(CH_2)_{10}$. In step (2), the aldehyde $RCHO$ is reduced in a two–electron process to a hydroxy–methyl compound [35]. In about half of our measurements, we did indeed observe a second peak or shoulder, but with an area smaller than the first peak (see Figure 6.4a). In Figure 6.4a this shoulder can be observed at about -0.65 V(SCE). The position of the first and the second peak was found to swift by about 60 mV in anodic direction per unit pH decrease of the solution. This is in agreement with the above reaction equations.

If all the COOH groups present at the thiol/electrolyte interface would have been reduced, a much larger current would have been observed. From an estimated surface concentration of COOH groups of about 4.10^{14} molecules per cm^2 [19], the maximum charge transfer would be about 130 μC cm^{-2}. Apparently, only 5–10% of the COOH groups are reduced to CHO. The main reason for the incomplete reduction of the COOH groups may be the presence of the long decane chain attached to the COOH group. Due to this aliphatic chain, the carboxyl group is deactivated by the electron-releasing alkyl group. According to Iverson and Lund [36], the presence of electron withdrawing groups is a prerequisite for the reduction of the carboxyl group. However, it was found that even acids with the carboxyl group attached to an aliphatic carbon chain can to some extent be reduced to the corresponding aldehyde or alcohol [35]. The yield

of the conversion is often low. Depending on the experimental conditions, it varied between 6% and 35% [35]. For example, the yield of the reduction of butyric acid to butanol in 80% sulphuric acid was 6.5% [35]. Hence, our results on the adsorbed COOH–terminated thiol monolayers agree with these results.

The Faradaic current involved in the reduction/oxidation reaction results in an increase in the differential capacitance as observed in Figure 6.4b. The capacitance in the potential region where no Faradaic current is observed is almost equal before and after reduction/oxidation which indicates that the structure of the adsorbed layer is not affected by the reaction of the terminal group (COOH ⇌ CHO). The value of the capacitance in this potential region is about 2.1 μF cm^{-2}; this value is included in Table 6.1. Also the calculated values of δ and ε_r are given in this table, together with ε_r of propionic acid (CH$_3$CH$_2$COOH [26]). Upon comparison of the values of ε_r for CH$_3$CH$_2$X with different terminal groups (Table 6.1), it is found that ε_r (COOH) is higher than ε_r for CH$_3$–terminated alkanes, but considerably lower than ε_r of the Cl, OH, CN terminated compounds. Apparently, the influence of the COOH group on ε_r of the COOH terminated alkane is low. However, comparing ε_r of the X–terminated thiol monolayers, we find that ε_r of the COOH thiol monolayer is relatively high. This may be explained from the lesser ordering and the less dense packing of the thiol molecules in the monolayer due to the bulkiness of the terminal COOH–group [19] as explained in section 6.3.1.

At the potential where the COOH group is (partly) reduced to CHO, the interfacial tension of the thiol/electrolyte interface decreases (Figure 6.4c). Consequently, the contact angle decreases. This may be caused by some irreversible reorganization of the thiol layer due to the smaller size of the CHO group. It is likely that this reorganization mainly occurs in the terminal groups because the capacitance of the thiol layer remains unaffected after reduction/oxidation. Upon scanning with a speed of 10 mV s^{-1}, γ_{SL} decreases by 16 mN m^{-1} in the first scan, which corresponds to a decrease in contact angle from 45° to 22° [12]. Scanning in the reverse direction, the contact angle remains 22°. Scanning again in cathodic direction results in a continuous decrease in contact angle from 22° to 18° at about –0.5 V(SCE) (not shown in

Figure 4c). After several scans, the contact angle finally reaches 0°, after which it remains unchanged upon repeated scanning. If the potential is scanned at 1 mV s^{-1} instead of 10 mV s^{-1}, $\Delta\gamma_{SL}$ decreases irreversibly by about 22 mN m^{-1} (Figure 6.4c). This corresponds to a decrease in contact angle from about 45° to about 0° already in the first scan. Apparently, the change in contact angle is a rather slow process. This is likely to be a result of the mechanism of the charge transfer process: the COOH will only be reduced to CHO when the electrolyte wets the surface sufficiently. After reduction, the wettability changes and the liquid meniscus will move and wet a fresh fraction of COOH surface. This process continues until the contact angle of the meniscus with the CHO–terminated surface reaches its equilibrium value.

6.4. Conclusions

This work has shown that monolayers of X–terminated thiol (HS(CH$_2$)$_{11}X$, with X = CH$_3$, CN, Cl, OH) on polycrystalline gold electrodes are highly stable upon cycling of the electrode in a potential region where only double layer charging occurs. From electrowetting measurements it is found that the electrocapillary maximum E_e depends on the electronegativity of the terminal group. With increasing electronegativity E_e increases in the order $E_e^{CH3} < E_e^{Cl} < E_e^{CN} < E_e^{OH}$.

The capacitance C of the monolayer depends on the dielectric properties of the terminal group X and increases in the sequence $C_{CH3} < C_{Cl} < C_{OH} < C_{CN}$. No indications are present that the capacitance is influenced by a difference in the density of packing and ordering of the molecules induced by the group X.

The change in γ_{SL} as a function of the potential as measured with the Wilhelmy balance is smaller than the electrostatic contribution γ_{SL}^{el} as calculated from the measured capacitance. The difference between these results (for X = OH, Cl, CN) are ascribed to the fact that the "chemical" component γ_{SL}^0 of the interfacial tension changes as a function of the applied potential. This change in γ_{SL}^0 is believed to be due to change in orientation of the molecules or of a part of the

molecules when altering the applied electric field across the thiol layer. Additional measurements are required to confirm this hypothesis. These structural changes, which do affect γ_{SL}^{0}, may occur without changing the capacitance of the thiol layer.

It is found that $HS(CH_2)_{10}COOH$ also forms a highly stable monolayer on gold electrodes, despite of the relative bulky COOH groups. The COOH group is partly (5–10%) reduced to the corresponding aldehyde. Reduction and oxidation occurs without affecting the capacitance of the COOH–terminated monolayer. The capacitance of the COOH thiol monolayer is higher than expected considering the dielectric properties of the COOH group. This is interpreted as a less dense and ordered structure of the monolayer.

In summary, it has been shown that functionalized alkanethiol monolayers on gold electrodes are stable in a wide potential region. This makes these layers suitable as model systems, for example for studying the influence of surface properties on the structure and morphology of electrochemically deposited metals. We will report on this subject in chapter 8.

References

[1]   Sondag–Huethorst, J.A.M.; Fokkink, L.G.J. *Langmuir* **1992**, *8*, 2560–2566 and Chapter 4, this thesis.

[2]   Sondag–Huethorst, J.A.M.; Fokkink, L.G.J. *J. Electroanal. Chem.* **1994**, *367*, 49–57 and Chapter 5, this thesis.

[3]   Schönenberger, C.; Sondag–Huethorst, J.A.M.; Jorritsma, J.; Fokkink, L.G.J. *Langmuir* **1994**, *10*, 611–614. Schönenberger, C.; Jorritsma, J.; Sondag–Huethorst, J.A.M.; Fokkink, L.G.J. *J. Phys. Chem. in press* and Chapter 3, this thesis.

[4]   Ulman, A. *An Introduction to Ultrathin Organic Films from Langmuir–Blodgett to Self–Assembly;* Academic Press: San Diego, 1991, and references cited therein.

[5]   Porter, M.D.; Bright, T.B.; Allara, D.L.; Chidsey, C.E.D. *J. Am. Chem. Soc.* **1987**, *109*, 3559–3568.

[6]   Bain, C.D.; Troughton, E.B.; Tao, Y.–T.; Evall, J.; Whitesides, G.M.; Nuzzo, R.G. *J. Am. Chem. Soc.* **1989**, *111*, 321–335.

[7]   Laibinis, P.E.; Whitesides, G.M.; Allara, D.L.; Tao, Y.–T.; Parikh, A.N.; Nuzzo, R.G. *J. Am. Chem. Soc.* **1991**, *113*, 7152–7167.

[8]   Sheen, C.W.; Shi, J.–X.; Mårtensson, J.; Parikh, A.N.; Allara, D.L. *J. Am. Chem. Soc.* **1992**, *114*, 1514–1515.

[9]   Walczak, M.M.; Chung, C.; Stole, S.M.; Widrig, C.A.; Porter, M.D. *J. Am. Chem. Soc.* **1991**, *113*, 2370–2378.

[10]   Fenter, P.; Eisenberger, P.; Li, J.; Camillone III, N.; Bernasek, S.; Scoles, G.; Ramanarayanan, T.A; Liang, K.S. *Langmuir* **1991**, *7*, 2013–2016.

[11]   Dubois, L.H.; Zegarski, B.R.; Nuzzo, R.G. *J. Chem. Phys.* **1993**, *98*, 678–688.

[12]   Ulman, A.; Eilers, J.E.; Tillman, N. *Langmuir* **1989**, *5*, 1147–1152.

[13]   Chidsey, C.E.D.; Liu, G.–Y.; Rowntree, P.A.; Scoles, G. *J. Chem. Phys.* **1989**, *91*, 4421–4423. Camillone III, N.; Chidsey, C.E.D.; Liu, G.–Y.; Putvinski, T.M.; Scoles, G. *J. Chem. Phys.* **1991**, *94*, 8493–8502.

[14]   Strong, L.; Whitesides, G.M. *Langmuir* **1988**, *4*, 546–558.

[15]   Fenter, P.; Eisenberger, P.; Liang, K.S. *Phys. Rev. Lett.* **1993**, *70*, 2447–2450.

[16]   Nuzzo, R.G.; Dubois, L.H.; Allara, D.L. *J. Am. Chem. Soc.* **1990**, *112*, 558–569.

[17]   Widrig, C.A.; Alves, C.A.; Porter, M.D. *J. Am. Chem. Soc.* **1991**, *113*, 2805–2810.

[18]   Nuzzo, R.G.; Dubois, L.H.; Allara, D.L. *J. Am. Chem. Soc.* **1990**, *112*, 558–569.

[19]   Chidsey, C.E.D.; Loiacono, D.N. *Langmuir* **1990**, *6*, 682–691.

[20]   Walczak, M.M.; Popenoe, D.D.; Deinhammer, R.S.; Lamp, B.D.; Chung, C.; Porter, M.D. *Langmuir* **1991**, *7*, 2687–2693.

[21]   Alves, C.A.; Porter, M.D. *Langmuir* **1993**, *9*, 877–886.

[22]   Laibinis, P.E.; Whitesides, G.M. *J. Am. Chem. Soc.* **1992**, *114*, 1990–1995.

[23]   Miller, C.; Cuendet, P.; Grätzel, M. *J. Phys. Chem.* **1991**, *95*, 877–886.

[24]   Throughton, E.B.; Bain, C.D.; Whitesides, G.M.; Nuzzo, R.G.; Allara, D.L.; Porter, M.D. *Langmuir* **1988**, *4*, 365–385.

[25]   Percec, V.; Heck, J. *J. Poly. Sci. Polym. Chem. Ed.* **1991**, *29*, 591–597.

[26]   Mellan, I. *Industrial Solvents Handbook*, 2nd ed.; Noyes Data Corp., New Jersey, 1977.

[27]   *Handbook of Chemistry and Physics*, 71st ed.; Lide, D.R., Ed.; CRC Press, USA, 1990.

[28]   Trasatti, S.; Parsons, R. *Pure & Appl. Chem.* **1983**, *8*, 1251–1268.

[29]   Allred, A.L. *J. Inorg. Nucl. Chem.* **1961**, *17*, 215–221.

[30]   Moore, W.J. *Physical Chemistry;* Longman: London, 1978.

[31]   Tao, Y.–T. *J. Am. Chem. Soc.* **1993**, *115*, 4350–4358.

[32]   Camillone III, N.; Chidsey, C.E.D.; Liu, G.; Scoles, G. *J. Chem. Phys.* **1993**, *98*, 3503–3511.

[33]   Tao, Y.–T.; Lee, M.–T. *Thin Solid Films* **1994**, *244*, 810–814.

[34]   Bain, C.D.; Whitesides, G.M. *Langmuir* **1989**, *5*, 1370–1378.

[35]   Eberson, L. In *Organic Electrochemistry*; Baizer, M.M., Ed.; Marcel Dekker Inc.: New York, **1973**; chapter 10.

[36]   Iversen, P.E.; Lund, H. *Acta Chem. Scand.* **1967**, *21*, 279–285.

Chapter 7

Potential-dependent wetting of electroactive ferrocene-terminated alkanethiolate monolayers on gold[1]

Abstract: The electrochemical and electrowetting behaviour of ferrocene(Fc)–terminated alkanethiol ($FcCO_2C_{11}H_{22}SH$) monolayers adsorbed on gold is studied in 1 M $HClO_4$. The concentration of the ferrocene groups in the monolayer is varied by diluting the adsorbed ferrocenethiol with alkanethiol ($C_nH_{2n+1}SH$ with n = 8, 12, 16, or 22). The Fc group of $FcCO_2C_{11}H_{22}SH$ can be oxidized to the Fc^+ cation while leaving the monolayer intact. Upon oxidation, the wettability of the surface increases: the advancing contact angle of the $FcCO_2C_{11}H_{22}SH$ monolayer with the electrolyte (θ_a^{red}) decreases from 74° to 49°, the latter being the advancing contact angle of the oxidized Fc^+ cation, θ_a^{ox}. Upon renewed reduction the meniscus recedes and the receding contact angle, θ_r^{red}, becomes 56° and can be continuously stepped between θ_r^{red} and θ_a^{ox}. Due to contact angle hysteresis this potential-dependent change in contact angle is only partly reversible. With the number of applied steps, a decrease in θ_r^{red} is observed due to disordering of the monolayer on continuous oxidation/reduction. This disruptive effect is reduced for a mixed $FcCO_2C_{11}H_{22}SH/C_{12}H_{25}SH$ monolayer. The $C_{12}H_{25}SH$ thiol increases the distance between the bulky Fc groups and consequently the monolayer becomes more stable. For a mixed monolayer with 60% $FcCO_2C_{11}H_{22}SH$ and 40% $C_{12}H_{25}SH$, the contact angle can reversibly be switched between 49° and 59°. We suggest that the change in wettability after oxidation/reduction is due to specific interactions of the charged Fc^+ ion with anions from the electrolyte. Due to the hydrophilic nature of the ClO_4^- anion, the wettability of the surface increases.

7.1. Introduction

The wettability of materials is determined by their surface properties. A well-known method to change the wettability of a material is through the adsorption of (a monolayer of) molecules. Many technological examples exist where the wettability is manipulated by such surface modification, for example in order to promote adhesion between surfaces [1], to prevent corrosion [2] or for lubrication purposes [3].

In addition to chemically-induced changes in the wettability, the surface wettability can also be adjusted electrochemically. Traditionally, this so-called electrowetting has been applied to liquid mercury [4]. Upon changing the potential, the diffuse electrical double layer at the electrolyte side of the interface adjusts itself. This induces a change in the surface free energy of the system and, consequently, a change in wettability [5]. This effect can for example be observed as a change in shape of a drop of liquid mercury deposited on a solid substrate in an electrolyte solution. The altered wettability of mercury as a function of the potential has also been measured using a platinum Wilhelmy plate covered with a thin mercury layer connected to a potentiostat (to control the potential) which measures the wettability as a function of the potential [6]. We used this latter method to determine the potential-dependent wetting of hydrophobic thiol-modified gold electrodes [7]. It was found both for mercury and thiol-modified gold that the relationship between the wettability and the potential could conveniently be described by interfacial thermodynamical relationships.

In this chapter we describe potential-induced wettability effects due to oxidation/reduction of a surface. To that end we modified gold electrodes with a ferrocene-terminated alkanethiol layer. As recently reported by Abbott and Whitesides [8], oxidation of the ferrocene groups of an adsorbed ferrocene thiol monolayer results in a decrease of the contact angle against 0.1 M $NaClO_4$ from 70° to about 43°. After renewed reduction the contact angle becomes 58°.

Repeated oxidation/reduction was found to result in progressively decreasing response.

Despite the bulky ferrocene (Fc) groups, the Fc–alkanethiols form a self-assembled monolayer on gold [8–16]. The ferrocene group of the ferrocenyl alkanethiol immobilized on gold may be oxidized to the ferricinium cation (Fc^+). The potential where oxidation/reduction takes place depends on the length and type of the alkanethiol chain connected to the ferrocene group, on the presence of other molecules in the monolayer and on the type and concentration of anions (Y^-) present in the electrolyte [9–12,14,17]. The anion effect has been claimed to result from specific interactions with anions (ion pair formation [11,13,14,17,18]) compensating the electric charge on the gold surface after oxidation:

$$(Fc)_S \rightleftharpoons (Fc^+)_S + e^- \tag{7.1}$$

$$(Fc^+)_S + Y^- \rightleftharpoons (Fc^+Y^-)_S \tag{7.2}$$
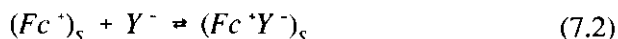
with $(Fc)_S$, $(Fc^+)_S$, and $(Fc^+Y^-)_S$ being the ferrocene group, the ferricinium cation, and the ion pair immobilized on the surface, respectively. Whether all Fc^+ groups formed in the monolayer bind an anion, or some charge remains uncompensated, still needs to be clarified. The formation of ion pairs is strongly affected by the nature of the anions [11,14,17]. Consequently, the electrical potential where oxidation of the Fc groups occurs depends on the anions. It was found that this potential increases in the order of $ClO_4^- > NO_3^- > SO_4^{2-}$. Ion pair formation was confirmed by using an electrochemical quartz crystal microbalance [13,18]. Upon oxidation of the ferrocene groups, an increased mass was observed which was attributed to the association of anions with the self-assembled layer.

The potential-dependent wetting of the Fc thiol is a direct consequence of oxidation/reduction of the Fc groups. The oxidation/reduction influences the surface free energy and consequently the surface tension of the solid-liquid interface, γ_{SL} [7b]. As suggested in ref. 7b, γ_{SL} may be taken to be composed of an electrical (potential-dependent) component, γ_{SL}^{el}, and a chemical (potential-

independent) component, $\gamma_{SL}^{\ 0}$

$$\gamma_{SL}(E) = \gamma_{SL}^{\ 0} + \gamma_{SL}^{\ el}(E) \tag{7.3}$$

where E is the applied potential. The chemical part is due to the intrinsic wetting properties of the surface. For the ferrocenethiol-modified gold electrode, $\gamma_{SL}^{\ 0}$ will be influenced by ion pair formation after oxidation; the associated (hydrophilic) anions will largely affect the wettability. However, according to microbalance measurements [13,18] it is not clear whether all Fc^+ cations in the monolayer are associated with anions. Therefore, it is possible that charge remains on the monolayer, compensated by ions in the diffuse electrical double layer in the electrolyte. This compensation of charge results in a change in $\gamma_{SL}^{\ el}$ with potential. In this chapter we attempt to unravel how the two components of γ_{SL} determine the electrowettability of gold electrodes modified with a monolayer of ω–(ferrocenyl carbonyloxy)–undecanethiol ($FcCO_2C_{11}H_{22}SH$ or, for short, FcC_{11}). From electrowetting measurements, an impression is thus obtained of the extent of charge compensation through ion binding. The influence of mixing the FcC_{11} thiol with alkanethiols ($C_nH_{2n+1}SH$ abbreviated as C_n thiol) as a function of the relative concentration and the chain length n of the alkanethiols on the electrowettability will be discussed.

7.2. Experimental

Materials. 1–Octanethiol ($C_8H_{17}SH$) obtained from Aldrich and 1–dodecanethiol ($C_{12}H_{25}SH$) and 1–hexadecanethiol ($C_{16}H_{33}SH$) obtained from Fluka were used as received. 1–Docosanethiol ($C_{22}H_{45}SH$) was prepared following literature procedures (supplementary material to ref. 19). The ω–(ferrocenyl carbonyloxy)-undecanethiol ($FcCO_2(CH_2)_{11}SH$, where Fc is $(\eta^5–C_5H_5)Fe(\eta^5–C_5H_4)$) was synthesized by esterification of ferrocene carboxylic acid and ω–bromoalcohol, and conversion of the bromide to the thiolacetate with sodium thioacetate, followed by hydrolysis of the thiolacetate with sodium carbonate (see supplementary material to ref. 10). The polycrystalline gold electrodes (of length 4.4 cm and thickness 0.5 mm) were mechanically polished and subsequently 200

nm of gold (99.999%) was thermically evaporated onto both sides of the gold substrate in a cryogenically pumped coating system.

Preparation of the monolayers. Detailed preparation procedures are reported in chapter 2. A self-assembled thiol monolayer on a UV/ozone cleaned gold electrode was formed by immersing the electrodes in a mixture of ferrocene-terminated thiol and unsubstituted alkanethiol in ethanol at 5 mM total thiol concentration. The relative mole fraction of Fc–terminated thiol to total thiol in the solution is denoted x_{Fc} and was 0.33, 0.60, and 1.0, respectively. The adsorption time was about 24 hours. The monolayers were characterized by (advancing and receding) sessile drop contact angle measurements with water (see chapter 2). After the electrochemical measurements, the modified electrodes were cleaned with UV/ozone to remove the thiol before renewed modification. This procedure resulted in reproducible behaviour of the thiol layer. However, after repeating this procedure for about 4 or 5 times, the quality of the layers became less (large contact angle hysteresis, irreproducible cyclovoltammograms) and a fresh gold layer was evaporated on the cleaned electrode after which the entire modification procedure could be repeated.

Potential-dependent contact angle and electrochemical measurements. The experimental procedure has been described in detail elsewhere [7a]. In summary, the thiol-modified gold electrode was used as a Wilhelmy plate connected to a bottom loading balance (Mettler PM2000). To allow potentiostatic control (with a Schlumberger 1186 EI/Hi–Tek Instruments PP RI potentiostat), the plate was used as a working electrode in a three-electrode configuration, using platinum as the counter electrode and a saturated calomel electrode (SCE) as the reference electrode. The plate is partly immersed in deaerated 1 M $HClO_4$. The scan rate was 10 or 100 mV s^{-1}. The capacitive current and the change in mass associated with the meniscus rise or fall were sampled (on a personal computer) as a function of the potential. The change in mass resulting from alterations in solid-liquid surface tension was converted to a change in contact angle [7].

Before and after a potential sweep, the differential capacitance of the thiol layer was measured at 0 V(SCE) using a frequency response analyzer (FRA;

Schlumberger Solartron 1170) generating a sinusoidally modulated potential with a frequency of 10 Hz and an amplitude of 10 mV to the Wilhelmy plate working electrode.

Besides in the scanning mode, the measurements were also performed in a step mode where the potential was switched between 0 V(SCE) and 0.9 V(SCE) in order to determine the rate of wettability changes.

The experiments were carried out at 25°C. The surface tension of the electrolyte solutions was about 72 mN m^{-1}. The reagents were analytical grade (Merck). The reported results are the average values of at least 3 independent measurements.

7.3. Results and discussion

7.3.1. ω–(Ferrocenyl carbonyloxy)undecanethiol

Figure 7.1a shows the change in current as a function of the applied potential for a gold electrode modified with a FcC_{11} thiol monolayer. The applied potential is scanned at 10 mV s^{-1}, beginning at 0 V(SCE), where the uncharged ferrocene group is stable, and reversing at 0.9 V(SCE), where the ferricinium cation is stable. For a scan rate of 100 mV s^{-1}, the shape of the curve (not shown) does not differ significantly. The current increases almost linearly with the scan rate as expected for a surface bound redox couple [20]. The shape of the cyclovoltammograms is symmetrical, indicating that the distribution of the reactivity of the ferrocene terminated alkanethiol molecules in the monolayer is narrow.

In addition to the redox peaks always some random sharp current spikes were observed in the oxidation/reduction potential region. Outside this region no such spikes were observed. The number and value of the current peaks varied per sample. Similar peaks were also observed by Uosaki et al. [14]. It was suggested that these peaks may either be due to structural changes in the self-assembled
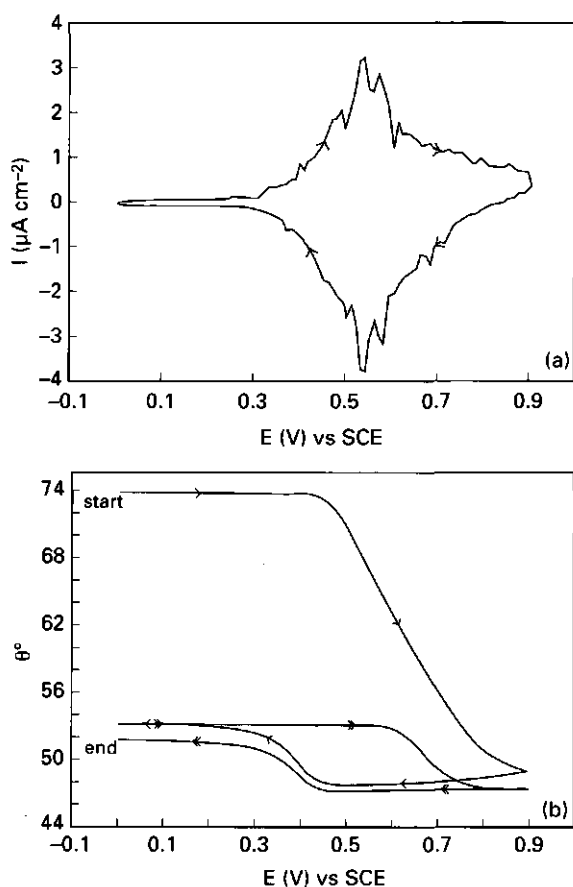
Figure 7.1: (a) Cyclovoltammogram for a FcC_{11} thiol modified gold electrode in 1 M $HClO_4$. (b) Potential-dependent change of the contact angle measured with the Wilhelmy method. Two successive scans between 0 and 0.9 V(SCE) are shown. (a) and (b) are measured simultaneously. The scan rate is 10 mV s^{-1} (first scan, > and <; second scan, ≫ and ≪).

monolayer or to strong interactions between the electroactive groups. The former is not very likely, because infrared spectroelectrochemical measurements did not show detectable changes in orientation of the ferrocenealkyl chains as a function of the applied potential [12]. The latter cause seems more probable since the electron transport through the alkane tail of the FcC_{11} thiol molecule and the subsequent oxidation of the Fc group may influence the oxidation of the neighbouring molecules.

Repeated scanning does not affect the cyclovoltammograms (including the random sharp current spikes), which demonstrates that the monolayers are stable in this potential range. The stability of the thiol layers is also confirmed by differential capacitance measurements at 0 V(SCE) before and after the electrochemical measurements. The value of the capacitance C_t ($\approx 2.0 \pm 0.1$ µF cm^{-2}) does not change, indicating that the FcC$_{11}$ monolayer is not affected by oxidation. The absolute capacitance value of the FcC$_{11}$ monolayer is relatively high compared to that of an unsubstituted alkanethiol layer of about the same chain length ($\approx$ hexadecanethiol ("C$_{16}$ thiol"), for which $C_t \approx 0.9$ µF cm^{-2} [7b]). The higher capacitance is partly due to the polar character of the ferrocene group [7c] and partly to the lower degree of ordering of the FcC$_{11}$ molecules.

The surface coverage of the FcC$_{11}$ thiol can be quantified by integration of the current peaks and dividing this area by the scan rate giving the amount of transferred charge Q [15]. The result is given in Table 7.1 for the pure FcC$_{11}$ thiol monolayer and several mixed monolayers. Knowing Q and realizing that oxidation is a single-electron process (see eq 7.1), the ferrocene surface coverage Γ_{Fc} can be estimated (see Table 7.1). The surface coverage is comparable for the cathodic and the anodic scan. Per individual sample the surface coverage varies between 3.6×10^{14} and 4.2×10^{14} molecules cm^{-2}. From geometrical considerations, the maximum surface coverage of the Fc–thiol is calculated to be 2.7×10^{14} cm^{-2} [10]. The discrepancy between the measured and calculated value may point to the roughness factor of about 1.5 for our gold electrodes which seems to be a reasonable number. The relatively large scatter in surface coverage per individual electrode is also found by other researchers [12,14,15]. It is probably a result of the relatively low ordering of the molecules due to the complex nature of the film-formation mechanism imposed by the bulky size of the ferrocene groups.

Figure 7.1b shows the influence of the potential on the contact angle θ as indirectly determined with the Wilhelmy plate method. The change in contact angle was determined simultaneously with the cyclovoltammogram in Figure 7.1a. The advancing contact angle is initially 74°. On scanning in the cathodic direction, the contact angle starts to decrease at a potential of about 0.4 V(SCE), just after the oxidation of the Fc group has started at 0.3 V(SCE) (Figure 7.1a).

After the oxidation is completed at about 0.8 V(SCE), the contact angle continues to decrease slowly (the front of the meniscus advances). In the reversed scan direction, the contact angle at first slightly decreases. The minimum contact angle reached is about 48°. When more than half of the Fc^+ cations have been reduced to Fc (at about 0.5 V(SCE)) the meniscus starts to recede and the contact angle increases. After the reduction of all the Fc^+ ions in the monolayer, θ still slightly increases until an equilibrium is reached. In this situation, the final contact angle at the end of the first scan has a value of about 53° at 0 V(SCE) which is much lower than the original value of 74°. In a second scan the contact angle starts to decrease again after more than 50% of the Fc groups have been oxidized and reaches about 48° at 0.9 V(SCE). On renewed reduction, the contact angle increases to 52°. Repeated scanning shows that the contact angle in this system can reversibly be switched between 48° and about 52°. The background of this change in wettability upon oxidation and reduction will be discussed in the next section.

Table 7.1: Characteristics of a ω-(ferrocenyl carbonyloxy) undecanethiol monolayer diluted with unsubstituted alkanethiols ($C_nH_{2n+1}SH$) adsorbed on gold.

Thiol	x_{Fc}	Q (μC cm^{-2})	$\Gamma_{Fc}\times10^{-14}$ (cm^{-2})	E_{max} (V(SCE))	C_t (μF cm^{-2})	θ_a^* (deg)	θ_r^* (deg)
FcC_{11}	1.0	62±6	3.9±0.3	0.54±0.01	2.0±0.1	74±3	55±3
FcC_{11}/C_{12}	0.6	39±3	2.4±0.2	0.56±0.01	1.8±0.1	76±3	58±3
FcC_{11}/C_{12}	0.33	26±2	1.6±0.1	0.56±0.01	1.4±0.1	85±3	60±3
FcC_{11}/C_8	0.6	48±4	3.0±0.3	0.54±0.01	1.9±0.1	74±3	51±3
FcC_{11}/C_{16}	0.6	38±3	2.4±0.2	0.59±0.01	1.4±0.1	93±3	75±3
FcC_{11}/C_{22}	0.6	20±2	1.3±0.1	0.61±0.01	0.9±0.1	110±3	86±3

*measured with water

The partly irreversible behaviour of the potential-dependent wetting of the FcC_{11} thiol is due to contact angle hysteresis: the advancing contact angle θ_a measured with water using the sessile drop method is 74°±3° and the receding contact
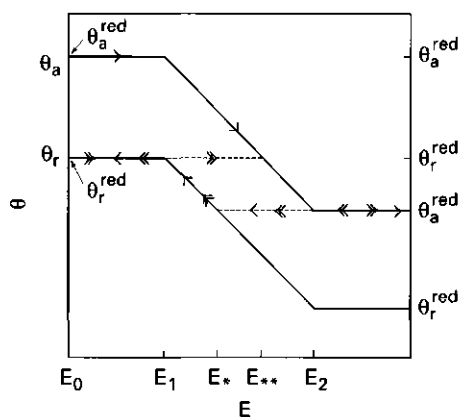
Figure 7.2: Schematic representation of the hysteresis effect on the potential-dependent change in wettability (first scan, > and <; second scan, ≫ and ≪). Details are given in the text.

angle θ_r is $55°\pm3°$ (see Table 7.1). Additionally, the contact angles of 1 M $HClO_4$ with this modified electrode were measured. Although there was a trend that the contact angles were lower than those with water, this difference was not significant. Figure 7.2 schematically shows the change in advancing and receding contact angles as a function of the potential. The meniscus will only move when the contact angle has a value beyond the solid lines drawn in Figure 7.2. Starting at a potential E_0 (at which the ferrocenethiol is in its reduced form) with an advancing meniscus with a contact angle θ_a^{red}, the potential is increased to E_1. At this potential the oxidation of the Fc groups starts and, consequently, the contact angle begins to decrease. At the potential E_2 where all FcC_{11} has reacted to Fc^+C_{11}, θ_a has reached the value of the advancing contact angle of the oxidized Fc^+C_{11} thiol θ_a^{ox} and remains constant. On the reverse scan in anodic direction, reduction of the Fc^+ cation starts at E_2. The contact angle does not start to recede at that potential since receding only occurs when the contact angle becomes smaller than the equilibrium contact angle $\theta_r(E)$ as indicated by the solid line drawn in Figure 7.2. At the potential E_* the meniscus will recede and the contact angle increases. At E_1 all Fc^+ is reduced, and θ_r becomes constant having a value of θ_r^{red}. The contact angle θ_r^{red} (at $E = E_0$) is equal to θ_r as measured with the sessile drop method. On repeating this cycle, θ again

decreases at E_{sw}. On continuous scanning a reversible contact angle loop is obtained where θ switches between θ_r^{red} and θ_a^{ox}. For the FcC_{11} monolayer, θ_r as measured with the sessile drop method is $55°\pm3°$. This agrees well with the θ_r^{red} (at 0 V(SCE)) found in Figure 7.1b ($\theta_r^{red} \approx 53°$).

The situation found in Figures 7.1a and 7.1b does approximately correspond with the schematic representation in Figure 7.2. The equilibrium contact angles are reached beyond the potential at which all Fc groups are reduced or oxidized. Clearly, the change in wetting is slow as compared to the change in charge transfer. One should realize, however, that the charge transfer at the surface of the macroscopic electrode is not necessarily the same as the charge transfer in the (thin) meniscus.
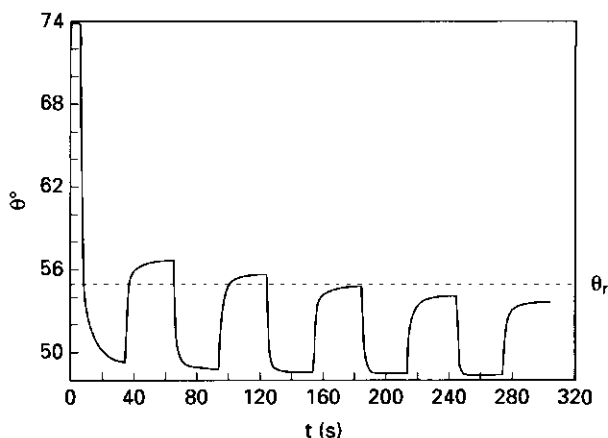
Figure 7.3: Change in contact angle of a FcC_{11} monolayer on gold in 1 M $HClO_4$ upon stepping the potential between 0 and 0.9 V(SCE) and back. Starting at 0 V(SCE) the potential is switched to 0.9 V(SCE) after 4 s. The potential remains at this value during 30 s and is then switched back to 0 V(SCE). After 30 s the potential is again stepped to 0.9 V(SCE). After 5 min this cycle is stopped. The dashed line (---) indicates the receding contact angle with water as measured with the sessile drop method.

The relatively slow movement of the advancing meniscus can be clearly observed when stepping the potential between 0 and 0.9 V(SCE). The time between the steps was 30 s. The results of these step experiments are shown in

Figure 7.3 where the contact angle is shown as a function of step time and potential. Initially θ_a is 74° ($=\theta_a^{red}$). After a few seconds the potential is stepped to 0.9 V(SCE), and the contact angle immediately starts to decrease. Within 2 seconds the meniscus is half–way between its initial and final height (t_{h50}). Within 4 s the meniscus is at 80% of its final height (t_{h80}) and finally the contact angle becomes 49° ($=\theta_a^{ox}$). After 30 s the potential is switched back from 0.9 to 0 V(SCE) and the contact angle increases from 49° to 56° ($=\theta_r^{red}$) in $t_{h50} \approx 1.5$ s and $t_{h80} \approx 3$ s (t_{h50} and t_{h80} are determined relatively to the difference between meniscus height before and after the last step). After another 30 s the potential is switched again from 0 to 0.9 V(SCE). The contact angle decreases from 56° (θ_r^{red}) to 49° (θ_a^{ox}) in $t_{h50} \approx 2$ s and $t_{h80} \approx 4$ s. The absolute values between which the contact angle is being switched is comparable with those observed in ref. 8b. The recession of the meniscus is always faster than the advance. When receding, the meniscus passes over a surface where the charge transfer has already occurred. On advancing, there is a dynamic quasi-equilibrium in the three phase line where charge transfer can only occur when the advancing meniscus has passed. Therefore, it is obvious that recession is a faster process than advance. The absolute values between which the contact angle is being switched is comparable with those observed in ref. 8b.

Besides the influence of the direction of the meniscus movement on the velocity of the meniscus, there is also an effect of the difference in contact angle before and after oxidation. This difference, and hence the total meniscus rise, is much larger in the first step from 0 to 0.9 V(SCE) than in the second one, whereas the time in which the rise takes place is about the same. Hence, the velocity (meniscus rise/time) is higher when the driving force, $\Delta\cos\theta$, is larger.

The receding contact angle with water θ_r determined with the sessile drop method is indicated by a dashed line in Figure 7.3. As was observed for the cyclovoltammogram, it is evident that the maximum recession of the meniscus when switching from 0.9 to 0 V(SCE) is mainly determined by the receding contact angle. However, in Figure 7.3 a constant decrease of θ_r^{red} after several cycles is observed. This effect is also seen in Figure 7.1b and is also observed by Whitesides et al. [8b]. The cause of this effect will be discussed in the next

section where pure FcC_{11} thiol monolayers are compared with FcC_{11}/alkane mixed thiol monolayers.

7.3.2. Coadsorption of ferrocene and dodecanethiols: influence of concentration

It is to be anticipated that mixing of ferrocenethiol with unsubstituted thiol will have two important effects on the monolayer [10]. First, assuming that the two compounds are homogeneously mixed in the monolayer, the unsubstituted alkanethiols may act as a spacer and keep the ferrocene groups laterally well-separated giving non–interacting sites. Second, the unsubstituted thiols may promote a more ordered self-assembled monolayer, resulting in a fixed distance between the Fc group and the electrode surface. Due to the bulkiness of the Fc group, the ordering of the FcC_{11} thiol monolayer is less than that of unsubstituted alkanethiols. On mixing with alkanethiol, the rate of ordering is expected to be influenced by the chain length and concentration of the unsubstituted thiol. The influence of the concentration was studied by mixing ω–(ferrocenyl carbonyloxy)undecanethiol with dodecanethiol ("C_{12} thiol"). The dodecyl chain is slightly shorter than the carbonyloxyundecyl tail of the FcC_{11} thiol because of the carboxyloxy link, and is therefore expected to separate the ferrocenethiol molecules which might have a positive effect on the ordering of the Fc groups.

The results of the electrochemical measurements on gold electrodes modified with a monolayer of FcC_{11} thiol mixed with C_{12} thiol are given in Figure 7.4a. The relative mole fraction x_{Fc} of FcC_{11} in the ethanol solutions was 1.0, 0.6 and 0.33, respectively. The characteristics of these layers are given in Table 7.1. The surface coverage of the FcC_{11} thiol is determined by integration of the *I–E*–curve as explained before. Comparing the surface coverage of the pure FcC_{11} thiol monolayer with those in the mixed monolayers, it is easily calculated that the relative surface coverage of FcC_{11} thiol is 0.6 for $x_{Fc} = 0.6$ and 0.4 for $x_{Fc} = 0.33$. Hence, there is no significant preferential adsorption of one of the
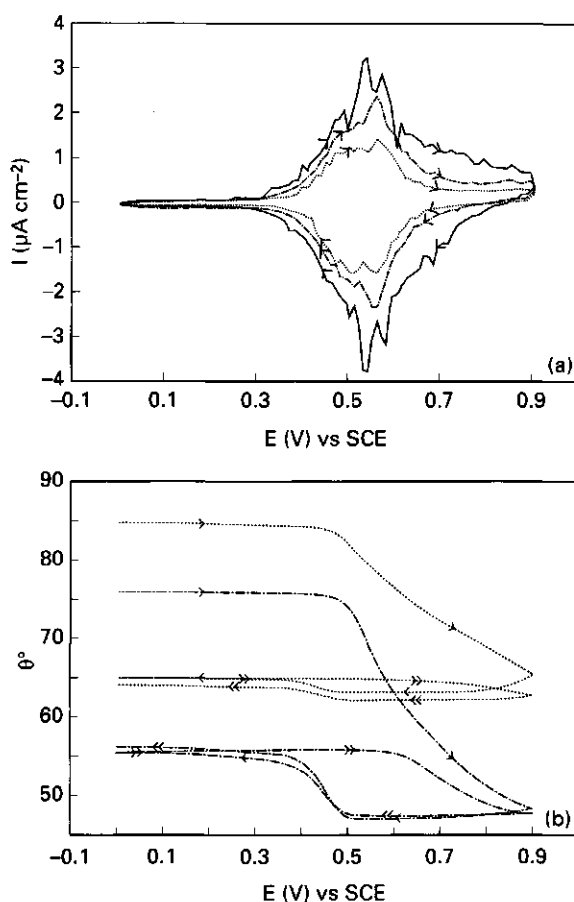
Figure 7.4: (a) Cyclovoltammogram (in 1 M $HClO_4$) for mixed monolayers of FcC_{11} thiol and C_{12} thiol on gold formed from ethanol solutions containing various mole fractions of the ferrocene-terminated thiol: $x_{Fc} = 1.0$ (——), 0.6 (-·-·-) and 0.33 (····). (b) Potential-dependent change of the contact angle measured simultaneously with (a) with the Wilhelmy plate method. The scan rate is 10 mV s^{-1} (first scan, > and <; second scan, ⪢ and ⪡). The analogous curve for $x_{Fc} = 1$ is shown in Figure 7.1b.

two compounds on the gold surface. The position of the maximum in the *I–E*-curve, E_{max}, is hardly affected by x_{Fc} (see Table 7.1 and Figure 7.4a). We will comment on this point later.

The differential capacitance C_t at 0 V(SCE) of the mixed monolayers depends

on the composition, and decreases with decreasing x_{Fc}. Mixing the FcC_{11} monolayer with C_{12} lowers the capacitance primarily because the capacitance of a pure C_{12} thiol monolayer is much lower ($\approx 1.1 \ \mu F \ cm^{-2}$ [7b]). Moreover [21], the monolayer will be more ordered because the surface concentration of the FcC_{11} thiol with its bulky Fc groups is less.

The advancing and receding contact angles have been measured with the sessile drop method for the different Fc concentrations and are given in Table 7.1. The contact angles are to some extent influenced by the concentration of the hydrophobic C_{12} thiol (θ_a of C_{12} thiol is $112°$[7b]). When $x_{Fc} = 0.6$, the contact angle is slightly changed compared to that at $x_{Fc} = 1$. At larger C_{12} thiol concentrations ($x_{Fc} = 0.33$) the contact angle notably increases. According to the Isrealachvili–Gee equation [22,23] the influence of the C_{12} thiol on the contact angle should have been more pronounced if the interface were composed of a random molecular mixture of the FcC_{11} and C_{12} thiol. However, the surface region is probably mainly composed of ferrocene due to the bulky Fc groups so that the underlying C_{12} thiol is partly shielded. Only at large C_{12} thiol concentrations is the C_{12} thiol experienced by the sessile drop. This shielding is only effective if the molecules are homogeneously mixed. If the surface would have consisted of large patches of relatively pure C_{12} thiol and FcC_{11} thiol, respectively, the advancing contact angle and the contact angle hysteresis are expected to have been higher. Therefore, we believe that either the two types of molecules are homogeneously mixed as has also been found for other types of thiol molecules [23,26,27] or that the patches are too small to be experienced by the sessile drop.

The results of the contact angle measurements obtained simultaneously with the cyclovoltammogram in Figure 7.4a, are given in Figure 7.4b. For sake of clarity only two curves are shown in this figure: for $x_{Fc} = 0.33$ and $x_{Fc} = 0.6$. The curve for $x_{Fc} = 1$ was already shown in Figure 7.1b. For the mixed monolayers, the same kind of semireversible behaviour of the contact angle as a function of the potential is found as for pure FcC_{11} thiol (compare Figures 7.4b and 1b). However, there are some differences. The reversible contact angle loop of the monolayer with $x_{Fc} = 0.33$ is much smaller than for $x_{Fc} = 1$. This is directly

caused by the lower Fc concentration in the monolayer for $x_{F_c} = 0.33$. Due to this lower concentration the difference between θ_a^{red} and θ_a^{ox} will be less whereas the contact angle hysteresis ($\theta_a^{red} - \theta_r^{red}$) is not affected. Consequently, the reversible contact angle loop becomes smaller (see Figure 7.2). Since θ_r of water measured with the sessile drop method is 60°, it is surprising that any contact angle loop is observed at all. Probably the contact angle determined with the sessile drop method differs slightly from θ_r^{red} as determined by the Wilhelmy plate. On the other hand, the contact angle loop of the monolayer with $x_{F_c} = 0.6$ is larger than with $x_{F_c} = 1$: θ can be switched between 47° (θ_a^{ox}) and 57° (θ_r^{ox}) whereas for the thiol layer with pure FcC_{11} thiol θ can be switched between 48° and about 52°. Apparently, θ_a^{ox} is hardly affected by a decreased FcC_{11} thiol concentration in the monolayer whereas θ_r^{red} is affected.

The effect of contact angle hysteresis can also be observed in the step–measurements in Figure 7.5 where the potential is periodically switched between 0 V(SCE) and 0.9 V(SCE), as in Figure 7.3. For ease of comparison, the curve of the latter figure is reproduced in Figure 7.5. The θ_r values determined with the sessile drop method are indicated by the dashed horizontal
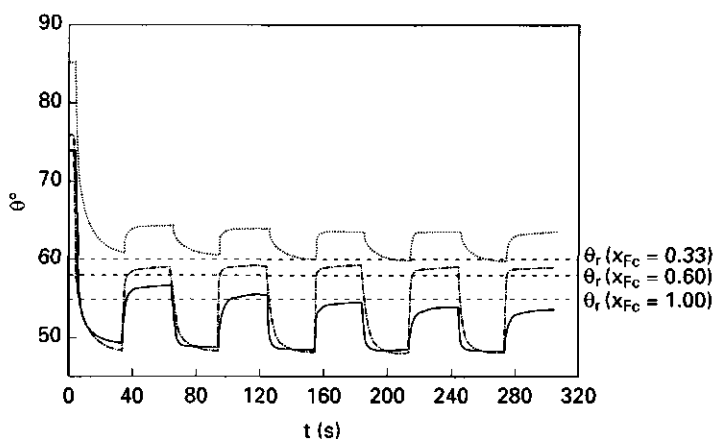
Figure 7.5: Change in contact angle (in 1 M $HClO_4$) for mixed monolayers of FcC_{11} thiol and C_{12} thiol on gold ($x_{F_c} = 1$ (——), 0.6 (-·-·-) and 0.33 (····)) while stepping the potential between 0 and 0.9 V(SCE). The description of the step procedure is given in the legend of Figure 7.3. The dashed horizontal lines (---) indicate the receding contact angle with water measured with the sessile drop method.

lines. An effect of θ_r on the shape of the curves is observed: the maximum recession of the meniscus is largely determined by θ_r. Like in the cyclic electrowetting measurements, the largest reversible electrowetting effect is observed for $x_{Fc} = 0.6$. In this case the contact angle can be switched between 49° and 59° (see Figure 7.5). For the potential scanning measurements (Figure 7.4b) it was found that the contact angle could be switched between 47° and 57°. The small difference between these measurements falls within the deviation between the individual measurements.

The absolute difference between the initial contact angle (θ_a^{red}) and the contact angle after the first step from 0 to 0.9 V(SCE), θ_a^{ox}, is hardly affected by x_{Fc}. This is a remarkable result since the surface charge of the undiluted monolayer after reduction is much higher than of the monolayer with $x_{Fc} = 0.33$, and therefore it is expected that the electrical double layer charge would also be much higher. Besides, if the change in electrical double layer would affect the electrowettability of the monolayer, this effect would have been larger anyway. For an undiluted Fc thiol layer on gold, the surface charge σ_0 is, after oxidation, 62 ± 6 μC cm^{-2}. It can be derived thermodynamically [7] that the change in free energy involved in establishing the electrical double layer (ΔF_d), which is equivalent to the change in the electrical component of the solid-liquid interfacial tension (γ_{SL}^{el}), is given by

$$\Delta F_d = \gamma_{SL}^{el} = -\int_{E_e}^{E} \sigma_0 d(E-E_e) \qquad (7.4)$$

where E_e is the potential of zero charge. Although we are not able to calculate exactly the difference in free energy involved in establishing the double layer at the ferrocenethiol-electrolyte interface because the potential of zero charge is unknown in this case, it is clear that the large surface charge (being about a factor 10–100 larger than that of an alkanethiol monolayer of the same chain length) would result in a very large change in γ_{SL}^{el} and, hence, in a very low contact angle. Comparing for example the surface charge of a dodecanethiol monolayer on gold in 10^{-2} M K_2SO_4, we found the maximum surface charge to

be about 1.4 μC cm^{-2} [7b] and the corresponding change in γ_{SL}^{el} being about 10 mN m^{-1}, which produced a contact angle shift from 112° to 105°.

Because the electrowettability effects are smaller than expected according to eq 7.4, and no measurable effect of the Fc concentration in the mixed monolayer on the electrowettability is found, it is concluded that the change in wettability is not mainly a result of a change in γ_{SL}^{el}. According to the model underlying eq 7.3, the electrowettability must consequently be ascribed to a change in the chemical component of γ_{SL}, γ_{SL}^{0}. This will be a direct result of the wetting properties of the anions bound to surface groups. These anions form ion pairs with Fc$^+$ after oxidation and give, for the ClO$_4^-$ anion, an advancing contact angle of about 48°. The charge of the Fc$^+$ groups must be completely compensated by the anions because no indications for an influence of the diffuse electrical double layer are found.

The question is whether a surface covered with ClO$_4^-$ results in a contact angle of about 48°. The hydration properties of perchlorate anions, which are in fact a degree of wetting, are unknown to us. Presumably, the perchlorate is not fully hydrated. For example, many perchlorate salts are soluble in both organic solvents and water. Hence, a contact angle of about 48° for the perchlorate adsorbed on the Fc$^+$ surface seems reasonable. In order to prove that ClO$_4^-$ ions specifically adsorbed on the Fc$^+$ surface are responsible for the change in wettability, we tried to adsorb other types of anions like Cl$^-$ (from 1 M HCl) or F$^-$ (from 1 M NaF). These attempts were not successful due to desorption of the Fc groups in these environments upon oxidation. This is likely to be caused by hydrolysis of the ester group, which is catalyzed by both base and acid [24]. On dilution of the Fc–monolayer with the C$_{12}$ thiol, the contact angle is mainly determined by the wetting properties of the FcC$_{11}$ thiol due to shielding effects of the large Fc groups. This effect still occurs when the Fc groups are oxidized and ion pairs are formed. Therefore, the initial contact angle jump after switching the potential from 0 to 0.9 V(SCE) will be hardly affected by the absolute FcC$_{11}$ concentration, unless the concentration becomes very low. This will be further demonstrated in the next section.

The ion pair formation also accounts for the difference between the electrowetting results between the monolayers with $x_{Fc} = 1$ and with $x_{Fc} = 0.6$ (see Figure 7.5). Due to this ion pair formation, θ_a^{ox} of the pure FcC_{11} thiol monolayer and of the mixed FcC_{11}/C_{12} ($x_{Fc} = 0.6$) monolayer are comparable. Apparently, the concentration of ClO_4^- anions is large enough for completely shielding the hydrophobic C_{12} thiol. The shielding of the reduced Fc groups (without ClO_4^- adsorbed) is less effective, resulting in a higher θ_r^{red} for the mixed monolayer.

For $x_{Fc} = 1$, a decrease of θ_r^{red} with the number of applied steps is observed. This was also observed in ref. 8b. This is not the case for the diluted thiol layers (see Figure 7.5). This effect is attributed to the lower degree of ordering of the bulky Fc–molecules in the pure FcC_{11} thiol monolayer. Continuous oxidation and reduction may induce more disorder stimulated by the relatively high Fc concentration in the monolayer, resulting in a lower receding contact angle and thus in a lower θ_r^{red}.

7.3.3. Coadsorption of ferrocene– and alkanethiols: influence of chain length of alkanethiols

In this set of experiments, the FcC_{11} thiol was mixed with alkanethiols of different chain length: C_8, C_{12}, C_{16} and C_{22}. The mole fraction of FcC_{11} thiol in the solutions was kept constant at 0.6. The results of the electrochemical measurements are shown in Figure 7.6a. The chain length has two effects on the cyclovoltammograms. First, the longer the unsubstituted thiol, the lower the concentration of FcC_{11} thiol in the monolayer (see Table 7.1). The relative surface coverages are respectively 0.8 (C_8 thiol), 0.6 (C_{12} thiol), 0.6 (C_{16} thiol) and 0.3 (C_{22} thiol). This preference was also found in the competition of other long–chain adsorbates with short–chain compounds [10,11,16,25] and can be attributed to the relatively poor solubility of the longer chains in the polar solvent ethanol leading to their preferential adsorption on gold. The relative concentration of the alkanethiols in the FcC_{11} monolayer also affects the

differential capacitance of the layers. With increasing alkanethiol concentration the capacitance becomes lower and eventually approaches that of the pure alkanethiol monolayer [7]. Second, with increasing chain length, E_{max} is shifted in the cathodic direction for both anodic and cathodic scans. This can be attributed to the hydrophobic environment of the FcC_{11} thiol molecules created by the coadsorbed alkanethiol [11]. It is most pronounced when the chain length
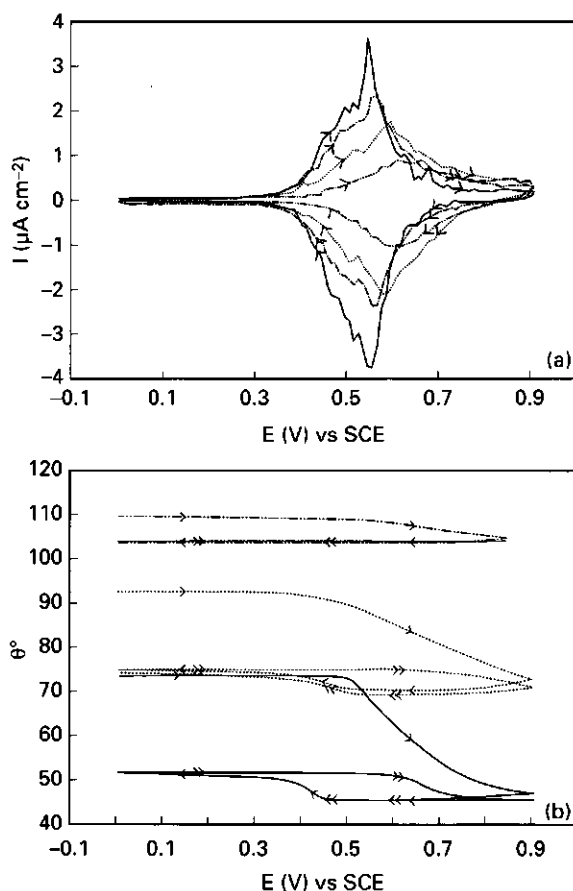
Figure 7.6: (a) Cyclovoltammogram (in 1 M $HClO_4$) for mixed monolayers of FcC_{11} thiol and C_8 (———), C_{12} (-·-··-), C_{16} (·····) or C_{22} (-···-··) thiol, respectively, on gold formed from ethanol solutions with $x_{Fc} = 0.6$. The relative concentration of the FcC_{11} thiol in the monolayer is then respectively 0.8, 0.6, 0.6, and 0.33. (b) Potential-dependent change of the contact angle measured simultaneously with (a) with the Wilhelmy plate method. The scan rate is 10 mV s^{-1} (first scan, > and <; second scan, ➤ and ◄). The curve for FcC_{11}/C_{12} ($x_{Fc} = 0.6$) is shown in Figure 7.4b.

of the alkanethiols is equal to or longer than the ferrocenethiol [11]. In our measurements this is the case for mixtures of FcC_{11} thiol with C_{16} or C_{22} thiol. With C_{12} thiol, even at high concentrations, E_{max} is hardly affected (Figure 7.4a). Therefore, the main effect of mixing on E_{max} is due to the creation of a hydrophobic environment for the terminal Fc groups by the longer alkanethiols. This may be ascribed to a reduced interaction of anions with the hydrophobic surface influencing the formation constant involved in the formation of ion pairs (eq 7.2).

The chain length of the alkanethiol strongly influences the contact angle of water with the mixed monolayers: the longer the alkane chain, the stronger the influence on the contact angles of the mixed monolayers (Table 7.1). For the FcC_{11}/C_{22} mixture, the C_{22} chain is considerably longer than the FcC_{11} chain, so that the Fc groups are almost completely buried in the alkane chains. The contact angles do not differ markedly then from those obtained with 100% C_{22} thiol (θ_a = 117°, θ_r = 88° [7b]).

The results of the contact angle measurements as a function of the potential of the FcC_{11} thiol layer mixed with C_8, C_{16}, and C_{22} thiol (x_{Fc} = 0.6), respectively, are given in Figure 7.6b. The corresponding result of the FcC_{11}/C_{12} mixed monolayer can be found in Figure 7.4b. The electrowettability of the FcC_{11}/C_8 and FcC_{11}/C_{16} mixed monolayer is (partly) reversible. Due to a much lower FcC_{11} concentration in the mixture with C_{22} thiol, the effect of the potential on the contact angle becomes less pronounced for this monolayer. Hence the difference between θ_a^{red} and θ_a^{ox} and between θ_r^{red} and θ_r^{ox} becomes less. This will influence the reversibility of the electrowettability: considering the situation sketched in Figure 7.2, the slope of the lines in Figure 7.2 will be less. In case θ_a^{ox} is larger than θ_r^{red}, the meniscus will not recede upon switching the potential from a value where Fc is oxidized to Fc^+ to a potential where the Fc^+ is reduced. This is the case for the FcC_{11}/C_{22} mixed monolayer where θ_a^{ox} = 103° and θ_r^{red} = 86°. Therefore, no reversible contact angle loop is found for the FcC_{11}/C_{22} mixture; the potential-dependent wetting behaviour of these monolayers is completely irreversible.

The influence of the alkane chain length on the results of the step measurements is shown in Figure 7.7 together with θ_r (dashed horizontal lines). Generally, mixing of the FcC_{11} thiol with C_8, C_{12}, or C_{16} thiol has a positive effect on the stability of the monolayer: no effect of the number of potentialsteps on θ_r^{red} of these mixed monolayers is found (Figure 7.7) whereas for the pure FcC_{11} thiol monolayer θ_r^{red} decreased with the number of potential-steps (Figure 7.3). Comparable with the scanning measurements in Figure 7.6b, it is observed that the electrowettability of the FcC_{11}/C_{22} mixture is irreversible.

Apart from the hysteresis effect on the potential-step curves, another effect is evident. The time frame in which the meniscus advances to arrive at its equilibrium position (after switching from 0 to 0.9 V(SCE)) becomes larger with increasing alkane chain length or with increasing alkanethiol concentration (see Figure 7.5). This observation can be attributed to the hydrophobic environment of the Fc groups. After switching from 0 to 0.9 V(SCE) the meniscus will attempt to find a new equilibrium position. This cycle is slow because charge can only be transferred when the meniscus has passed over the surface. In this process it is disadvantageous when the surface also contains hydrophobic groups.
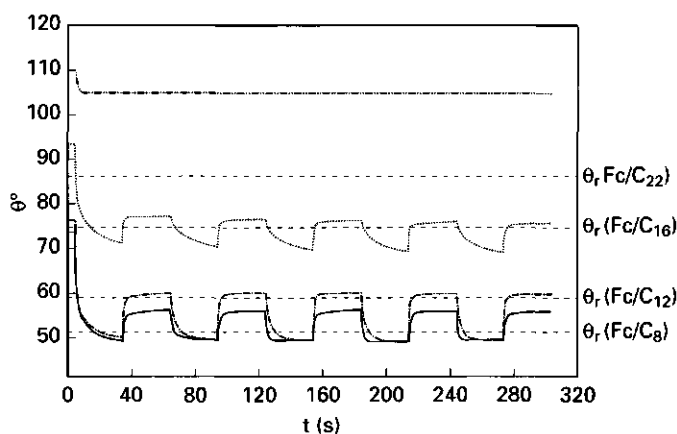
Figure 7.7: Change in contact angle for mixed monolayers of FcC_{11} thiol and C_8 (———), C_{12} (-·-·-), C_{16} (····) or C_{22} (-··-··) thiol, respectively, on gold (x_{Fc} = 0.6) while stepping the potential between 0 and 0.9 V(SCE). The description of the step procedure is given in the caption of Figure 7.3. The dashed horizontal lines (---) indicate the receding contact angle with water measured with the sessile drop method.

The hydrophobic molecules will interrupt the cycle of the ferrocene groups between charge transfer and meniscus movement and consequently the advance of the meniscus becomes slower.

The time to recede is hardly affected by the alkanethiol chain length. In this case there is no dynamic equilibrium between the charge transfer in the meniscus and the meniscus movement because all charge (including in the meniscus area) will be transferred as soon as the potential is switched from 0.9 to 0 V(SCE). At that time the surface becomes an uncharged ferrocene surface with poor wettability and the meniscus will drop instantaneously.

7.4. Conclusions

The electrochemical and electrowetting characteristics of mixed FcC_{11}/alkanethiol monolayers on gold have been studied. It is found that the Fc groups can be oxidized or reduced without desorbing from the gold substrate. On oxidizing the Fc group to the ferricinium cation Fc^+ in a monolayer of pure FcC_{11}, the advancing contact angle with 1 M $HClO_4$ changes from 74° (θ_a^{red}) to 49° (θ_a^{ox}). After renewed reduction the contact angle increases to 56° (θ_r^{red}) and can then be continuously stepped between about 56° and 49°. This partly irreversible wetting behaviour is shown to be caused by contact angle hysteresis of the monolayer. With the number of applied steps a decrease in θ_r^{red} is observed which is ascribed to disordering of the monolayer due to continuous oxidation and reduction. This disruptive effect of the oxidation/reduction on the ordering of the monolayer is prevented by mixing the FcC_{11} thiol with a C_8, C_{12}, or C_{16} thiol, respectively. No indications for clustering of the FcC_{11} thiol and the alkanethiol are found. The mixing has a positive effect on the stability of the FcC_{11} molecules due to a larger distance between the bulky Fc groups.

The contact angles of water with mixed FcC_{11}/C_n thiol (with $n = 8$ or 12) monolayers with relatively high FcC_{11} thiol concentration ($x_{Fc} \geq 0.66$) are similar to those of the pure FcC_{11} thiol monolayers due to shielding of the alkanethiol

by the bulky Fc groups. This shielding becomes less effective for longer alkanethiols (C_{16} or C_{22} thiol) and for lower FcC_{11} thiol concentrations in the monolayer.

Strong indications were found that the electrowettability is a result of ion pair formation with (hydrophilic) anions upon oxidation of the Fc groups to compensate the surface charge. These anions change the chemical component of the solid-liquid interfacial tension, γ_{SL}^{0}, and consequently the wettability. The absolute amount of Fc groups in the mixed monolayer hardly influences the potential-induced wettability change, as long as the chain length of the alkanethiol is shorter than the tail of the Fc thiol and as long as the mole fraction of FcC_{11} in the solution is above $x_{Fc}>0.3$. From this finding and from the fact that the wettability is smaller than expected on the basis of the change in the surface charge, we conclude that the electrical double layer charge compensation by the electrolyte is negligible as a result of the low net surface charge due to anion adsorption. Therefore, we conclude that the charge of the ferricinium cations formed after oxidation is completely compensated by ClO_4^- anions.

The largest reversible contact angle loop is observed when mixing the FcC_{11} thiol with C_{12} thiol (with $x_{Fc} = 0.6$). In this case θ can be switched between 49° (θ_a^{ox}) and 59° (θ_r^{red}).

The rate with which the wettability changes as a function of the potential is found to be influenced by the direction of the meniscus movement. Advance is always slower than recession due to the dynamic equilibrium between charge transfer and adjustment of the contact angle in the meniscus during the rise of the meniscus. This adjustment is hindered by the presence of hydrophobic molecules in the thiol layer, the advance becoming slower. The rate of meniscus movement is also influenced by the absolute change in contact angle before and after oxidation; the larger the difference, the faster the meniscus moves.

This study has shown that the oxidation/reduction of Fc–terminated thiol monolayers provide an elegant method to significantly alter the wettability of surfaces. The change in wettability is highly reversible. The reversibility is only

limited by contact angle hysteresis. Reduction of contact angle hysteresis in the present system will be difficult to achieve due to the large size of the Fc groups.

References

[1]   Stewart, K.R.; Whitesides, G.M.; Godfried, H.P.; Silvera, I.F. *Rev. Sci. Intrum.* **1986**, *57*, 1381–1383.
[2]   (a) Laibinis, P.E.; Whitesides, G.M. *J. Am. Chem. Soc.* **1992**, *114*, 9022–9028. (b) Michelhaugh, S.L.; Bhardwaj, C.; Cali, G.J.; Bravo, B.G.; Bothwell, M.E.; Berry, G.M., Soriaga, M.P. *Corrosion* **1991**, *47*, 322–328.
[3]   Bowden, F.P.; Tabor, D. *The Friction and Lubrication of Solids*, Oxford University Press: London, **1968**, and references cited therein.
[4]   Matsumoto, H.; Colgate, J.E. *IEEE Micro Electro Mechanical Systems*, Napa Valley, Feb. 11–14 **1990**, 105–110.
[5]   Verwey, E.J.; Overbeek, J.Th.G. *Theory of stability of lyophobic colloids*, Elsevier, Amsterdam, **1948**.
[6]   Hato, M. *J. Colloid Interface Sci.* **1989**, *30*, 130–136.
[7]   (a) Sondag–Huethorst, J.A.M.; Fokkink, L.G.J. *Langmuir* **1992**, *8*, 2560–2566 and chapter 4, this thesis.
        (b) Sondag–Huethorst, J.A.M.; Fokkink, L.G.J. *J. Electroanal. Chem.* **1994**, *367*, 49–57 and chapter 5, this thesis.
        (c) Chapter 6, this thesis.
[8]   (a) Abbott, N.L; Whitesides, G.M. *ECS Meeting, New Orleans*, Oct. 10–15, **1993**, extended abstract 594, (b) Abbott, N.L.; Whitesides, G.M. *Langmuir* **1994**, *10*, 1493-1497.
[9]   Collard, D.M.; Fox, M.A. *Langmuir* **1991**, *7*, 1192–1197.
[10]   Chidsey, C.E.D.; Bertozzi, C.R.; Putvinski, T.M.; Mujsce, A.M. *J. Am. Chem. Soc.* **1990**, *112*, 4301–4306.
[11]   Creager, S.E.; Rowe, G.K. *Anal. Chim. Acta* **1991**, *246*, 233–239.
[12]   Popenoe, D.D.; Deinhammer, R.S.; Porter, M.D. *Langmuir* **1992**, *8*, 2521–2530.
[13]   Shimazu, K.; Yagi, I.; Sato, Y.; Uosaki, K. *Langmuir* **1992**, *8*, 1385–1387.
[14]   Uosaki, K.; Sato, Y.; Kita, H. *Langmuir* **1991**, *7*, 1510–1514.
[15]   Walczak, M.M.; Popenoe, D.D.; Deinhammer, R.S.; Lamp, B.D.; Chung, C.; Porter, M.D. *Langmuir* **1991**, *7*, 2687–2693.

[16]   Rowe, G.K.; Creager, S.E. *Langmuir* **1994**, *10*, 1186–1192.

[17]   Inzelt, G.; Szabo, L. *Electrochemica Acta* **1986**, *31*, 1381–1387.

[18]   De Long, H.C.; Donohue, J.J.; Buttry, D.A. *Langmuir* **1991**, *7*, 2196–2202.

[19]   Bain, C.D.; Troughton, E.B.; Tao, Y.–T.; Evall, J.; Whitesides, G.M.; Nuzzo, R.G. *J. Am. Chem. Soc.* **1989**, *11*, 321–335.

[20]   Bard, A.J.; Faulkner, L.R. *Electrochemical Methods: Fundamentals and Applications*; Wiley: New York, 1980, p. 522.

[21]   Porter, M.D.; Bright, T.B.; Allara, D.L.; Chidsey, C.E.D. *J. Am. Chem. Soc.* **1987**, *109*, 3559–3568.

[22]   Israelachvili, J.N.; Gee, M.L. *Langmuir* **1989**, *5*, 288–289.

[23]   Ulman, A.; Evans, S.D.; Shidman, Y.; Sharma, R.: Eilers, J.E. *Adv. Colloid Interface Sci.* **1992**, *39*, 175–224.

[24]   Morrison, R.T.; Boyd, R.N. *Organic Chemistry*; Allyn and Bacon: Boston, MA, 1973; pp. 677–682.

[25]   Bain, C.D.; Whitesides, G.M. *J. Am. Chem. Soc.* **1989**, *111*, 7164–7175.

[26]   Bain, C.D.; Evall, J.; Whitesides, G.M. *J. Am. Chem. Soc.* **1989**, *111*, 7155–7164.

[27]   Bertilsson, L.; Liedberg, B. *Langmuir* **1993**, *9*, 141–149.

Chapter 8

Galvanic copper deposition on thiol–modified gold electrodes[1]

Abstract: Galvanic deposition of copper from 10^{-2} M $CuSO_4$ on self–assembled X–terminated alkanethiol monolayers ($HS(CH_2)_{n-1}X$) on gold is studied. The influence of the chain length ($X = CH_3$, $n = 12, 18, 22$) and of the type of terminal group ($X = OH$, Cl, CN ($n = 12$), COOH ($n = 11$)) on the deposition process is determined using cyclovoltammetry and optical and scanning electron microscopy. The presence of a thiol layer on gold, independent of the terminal group or thiol chain length, results in deposition of hemispherical nuclei whereas deposition on bare gold gives rather homogeneous flat copper films. The difference in morphology is ascribed to the difference in surface tension between copper and the substrate. Nucleation occurs on top of the thiol layer when the self-assembled monolayer is highly ordered. For nucleation to occur, an overpotential is required due to the potential drop across the dielectric of the thiol layer. As a consequence, the overpotential is found to increase with increasing thiol chain length: it is about -210 mV for a $HS(CH_2)_{17}CH_3$ layer and -270 mV for a $HS(CH_2)_{21}CH_3$ layer. The structure of the monolayer affects the potential drop across the thiol layer, and therefore the magnitude of the deposition overpotential. This makes cyclovoltammetry to a very sensitive method to test the quality of self-assembly. Although the overpotential for nucleation on OH–terminated thiol is about the same as for CH_3–terminated thiol, about 100 times more particles are deposited on the OH–terminated thiol. This is ascribed to a combination of a smaller potential drop across the OH–thiol layer and a higher chemical affinity of Cu ad–atoms for OH–groups. The cyclovoltammograms of the short chain CH_3–, CN–, and Cl–terminated thiols do not show a distinct overpotential. We believe that this is related to the occurrence of defects in the thiol monolayer.

8.1. Introduction

Metal/metal and metal/organic interfaces play an important role in many areas
of technology. These interfaces are relevant both on a macroscopic scale, like in
the plating industry [1], and on a microscopic scale as in lithographic
applications [2,3]. An understanding of the factors governing the morphology of
a metal deposit on solid substrates is vital in order to be able to control the
morphology of these deposits. Usually smooth and homogeneous metal deposits
are required. One of the many factors determining the morphology of metal
deposits is the substrate on which the metal is deposited. For example, galvanic
deposition of PbO_2 on platinum results in a homogeneous and dense film
whereas deposition of PbO_2 on carbon (under the same plating conditions) results
in hemispherical PbO_2 particles [4]. Similarly, the nature of the substrate plays
an important role when metal is vapour–deposited on, e.g., polymer surfaces [5].

The purpose of this study is to investigate the influence of the wettability of the
substrate on the morphology of metal deposits. For this purpose we use a model
system for the interface between a metal and an organic material: galvanically
deposited metal on self–assembled X–terminated alkanethiol ($HS(CH_2)_{n-1}X$)
monolayers adsorbed on polycrystalline gold. The structure and properties of
thiol monolayers on gold have been studied extensively [6]. These monolayers
are known to be highly ordered and densely packed for $n>9$ [7,8]. The sulphurs
form a chemical bond with the gold and have a $(\sqrt{3}\times\sqrt{3})R30°$ commensurate
overlayer structure on Au(111) [9,10]. The ordering of the monolayers is found
to be unaffected by the type of terminal group as long as the cross-sectional area
of this group is comparable to or smaller than that of the polymethylene spacer
group [11,12]. This is for example the case for $X = CH_3$, CN, Cl or OH [13,14].
These monolayers are found to be highly stable under electrochemical conditions
in an indifferent electrolyte as long as only double layer charging occurs. Even
for a relatively large terminal group like COOH we found the monolayer to be
stable [14].

One of the advantages of self–assembled monolayer–modified electrodes as

model systems over organic substrates such as polymers is that metal deposition on monolayer-modified surfaces can be studied in a well–controlled galvanic manner. Another advantage is that the type and concentration of surface functional groups can be controlled to test their reactivity with the metal deposit. A prerequisite for using such monolayers as model systems is that defects like pinholes are either absent or small enough to prevent penetration of metal (ions) into the monolayer. From atomically resolved Scanning Tunneling Microscopy (STM) measurements on thiol layers in air, we know that the monolayer contains defects on a microscopic scale [10,15]. The most pronounced defects are holes in the top gold layer with a depth corresponding to one unit cell. These holes are (partly) filled with ordered thiol [10,15]. Another defect observed with STM are missing rows of thiol molecules. Incidentally, ill–defined structures with an area of a few nm^2 are found in the STM–image. These are assumed to consist of disordered thiol molecules [16]. However, from extensive electrochemical measurements with thiol–modified gold electrodes we found that penetration of small ions like H^+ is largely blocked due to the shielding of defects by the long chain alkane chains [14,17]. Therefore, although defects may be present in air, they do not necessarily affect the (surface) properties of the thiol monolayer in a wet environment. In the present study we wish to address the question whether or not these layers are suitable model systems for studying metal/organic material interactions. In other words, does nucleation of the metal occur at the thiol/electrolyte interface or at the gold/thiol interface?

From a previous study [3] we know that it is possible to galvanically deposit a metal on the thiol layer. However, large overpotentials are required. In the present chapter we investigate systematically the effects of adsorbed organic monolayers on the morphology of the galvanically deposited copper. The influence of the alkanethiol chain length ($HS(CH_2)_{n-1}CH_3$, $n = 12, 18, 22$) and the role of the terminal group of the thiol molecule ($HS(CH_2)_{n-1}X$, $X = CH_3$, Cl, CN, OH with $n = 12$ and COOH with $n = 11$) on the deposition will be studied. The results are compared with copper deposited on bare gold.

8.2. Experimental

Materials. 1–Dodecanethiol $(HS(CH_2)_{11}CH_3)$ from Fluka and 1–octadecanethiol $(HS(CH_2)_{17}CH_3)$ from Janssen Chimica were used as received. 1–Docosanethiol $(HS(CH_2)_{21}CH_3)$, 11–mercapto–1–undecanol $(HS(CH_2)_{11}OH)$, 11–mercaptoundecanoic acid $(HS(CH_2)_{10}COOH)$, 11–chloroundecanethiol $(HS(CH_2)_{11}Cl)$, and 11–mercaptododecanitrile $(HS(CH_2)_{11}CN)$ were prepared according to procedures described in the literature [8,8,18,19,15]. The polycrystalline gold electrodes $(1 \times 1 \text{ cm}^2)$ were mechanically polished on one side. Subsequently, 100 nm of gold (99.999%) was evaporated onto the polished side of the gold substrate in a cryogenically pumped coating system [17].

Preparation of the monolayers. Detailed preparation procedures have been reported previously [17]. Before modification, the gold electrode was first cleaned with HNO_3 (65%) for 15 min, rinsed with water and ethanol, and then cleaned for 15 min in a UV–ozone reactor (UVP Inc., PR–100). Immediately afterwards the electrode was immersed in a 3.5 mM thiol solution in methanol. The adsorption time was at least 1 day. The monolayers were characterized by (advancing and receding) sessile–drop contact–angle measurements with water [17].

Electrochemical experiments. Cyclic voltammetry was performed with a potentiostat (Schlumberger 1186 EI/Hi–Tek instruments PP RI). The (modified) gold substrates were mounted horizontally in a conventional three–electrode cell with an exposed area of 0.74 cm^2. Platinum was used as the counter electrode and a saturated calomel electrode (SCE) served as the reference electrode. The electrolyte (10^{-2} M $CuSO_4$ in 10^{-2} M H_2SO_4) is deaerated in the cell. The potential was scanned in the cathodic direction from an initial potential of 0.5 V(SCE) with a scan rate of 10 mV s^{-1}. The final potential was varied between –0.15 V(SCE) and –0.35 V(SCE).

Measurements were done on both bare and modified surfaces of the gold working electrode. For measurements on bare gold, the substrates were treated

for 15 min in the UV/ozone reactor just prior to use. Experiments with the thiol/gold substrates were carried out on freshly deposited monolayers. Before and after recording of the cyclovoltammogram, the differential capacitance of the thiol layer in 10^{-2} M K_2SO_4 was measured with a frequency response analyzer (FRA, Schlumberger Solartron 1170). The FRA supplied an ac signal with a frequency of 10 Hz and an amplitude of 10 mV to the working electrode.

Incidentally, potential step measurements were carried out. To that end the potential was first scanned from 0.5 V(SCE) to –0.15 V(SCE) (or –0.3 V(SCE)) with a scan rate of 10 mV s^{-1}. At –0.15 (or –0.3) V(SCE) the potential was stepped to –0.1 V(SCE) and the charge passed during deposition was registered. After the potential step measurements the metal deposit was imaged with an optical microscope and an electron microscope (SEM, Philips 515) in order to count the number of particles and to determine the shape and size of the particles.

All experiments were carried out at 25°C. The reagents were analytical grade (Merck). The measurements were repeated at least three times. The results given in the cyclovoltammograms represent the average values obtained in these measurements.

8.3. Results and discussion

8.3.1. Comparison of Cu–deposition on bare and thiol–modified gold

The current density (I)–potential (E) curves for electrodeposition of copper on bare gold and on $HS(CH_2)_{21}CH_3$ ("C_{22} thiol") modified gold are shown in Figure 8.1. The deviation between the cyclovoltammograms of the individual modified electrodes is quite large ($\pm 30\%$) whereas the spread in results for the bare gold is much smaller ($\pm 5\%$). The cyclovoltammogram for Cu deposition on the C_{22} thiol monolayer differs slightly from the cyclovoltammogram for the same

monolayer shown in ref. 3. This is probably due to a difference in the quality of the thiol layer caused by the gold substrates: in ref. 3 Au sputtered on Si(111) was used whereas in the present case evaporated Au on Au substrates is used. Because the overpotential at the sputtered gold substrate was somewhat lower, we assume that the monolayer on this substrate contains more defects than on the evaporated substrates that are used in the present study.
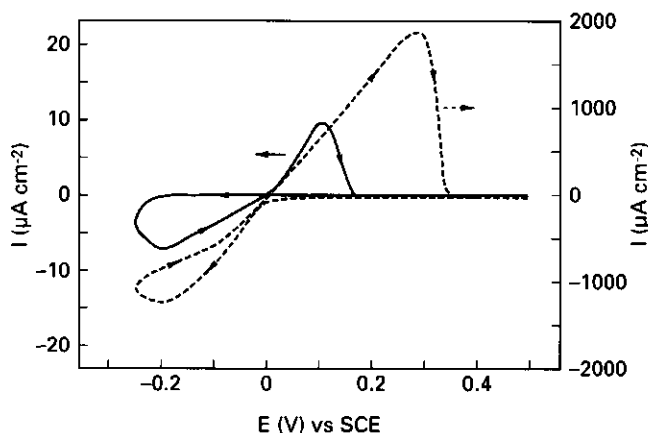

Figure 8.1: Cyclovoltammogram of a bare Au electrode (dashed curve, right hand axis) and of a HS(CH$_2$)$_{21}$CH$_3$–modified Au electrode (solid curve, left hand axis) in 10^{-2} M CuSO$_4$, 10^{-2} M H$_2$SO$_4$. The scan rate was 10 mV s^{-1}.

The equilibrium Cu^{2+}/Cu or Nernst–potential is 0.04 V(SCE) in 10^{-2} M CuSO$_4$. For the bare gold electrode in this electrolyte a monolayer of Cu is deposited at a potential positive of the Nernst potential. This phenomenon is referred to as under potential deposition (UPD). Bulk copper deposition occurs at potentials negative with respect to the Nernst potential and bulk Cu dissolves at potentials positive with respect to this potential. The presence of the thiol monolayer suppresses the UPD process. The occurrence or absence of UPD can not directly be deduced from Figure 8.1 because the currents involved are only small. Only at larger magnification the UPD peaks can be observed. The most important reason for the absence of UPD with monolayer-modified substrates is that the interaction between copper and the hydrophobic alkanethiol is much lower than the interaction between the individual copper atoms. Nucleation of copper on the

alkanethiol monolayers, which starts at about –0.23 V(SCE), occurs as three dimensional nuclei (Figure 8.2a) whereas for nucleation of Cu on bare gold rather homogeneous flat films are formed (Figure 8.2b). A detailed discussion on the cause of this pronounced difference in morphology of the copper deposit will be given later.
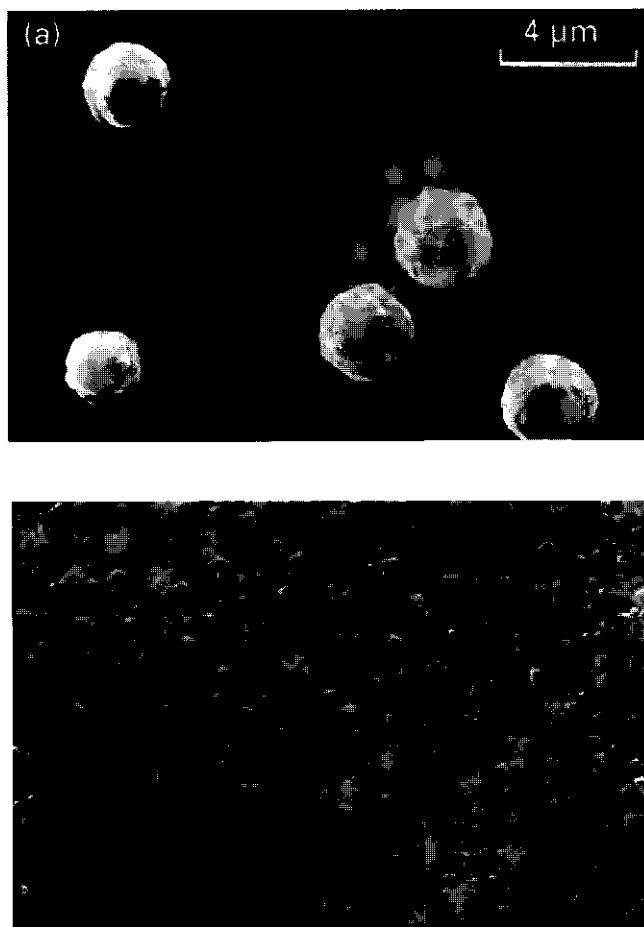
Figure 8.2: Scanning electron micrograph (under an angle of 0°) of galvanically deposited copper on a (a) $HS(CH_2)_{10}COOH$–modified gold electrode and (b) on bare gold from 10^{-2} M $CuSO_4$, 10^{-2} M H_2SO_4. Deposition conditions: (a) scanning from 0.5 V(SCE) to –0.35 V(SCE) at 10 mV s^{-1}, and subsequently a potential step to –0.1 V(SCE) and keeping the potential at this value for 3 min, (b) 2 min at –0.3 V(SCE).

The most striking difference between the two cyclovoltammograms is the overpotential η required for copper deposition on the modified gold electrode. This overpotential is defined as the difference between the potential where nucleation starts and the Nernst potential. In the present work we take η as the potential in the cyclovoltammogram where the cathodic current starts to increase very fast. The nature of this overpotential may be of different origins. First, it may be caused by the substantial potential drop across the dielectric of the thiol layer. Due to this potential drop, the potential remaining at the thiol/electrolyte interface and experienced by the Cu^{2+} ions, is only small. If this "potential–drop-mechanism" is effective, it is necessary for electrons to pass through the thiol layer in order to reduce the copper ions at the thiol/electrolyte interface. Copper will thus be formed on top of the thiol layer (see Figure 8.3a). A second possible reason for the overpotential may be due to a resistance for the Cu^{2+} ions to penetrate the thiol layer through pinholes ("penetration mechanism"). Once having penetrated, Cu^{2+} could than be reduced at the Au interface. Nucleation occurs through these defects, producing a mushroom–shaped particle (Figure 8.3b). For homogeneous, conducting surfaces, the overpotential is ascribed to the critical free energy required to form a thermodynamically stable nucleus on the surface [20,21]. As will be discussed in this chapter, we have strong indications that the first nucleation mechanism, i.e., phase formation at the thiol/electrolyte interface, is effective in the present systems.

The reproducibility of the cyclovoltammograms for copper deposition on thiol–modified gold electrodes is relatively poor. Between the cyclovoltammograms of the individual electrodes a relatively large deviation from the average of $\pm 30\%$ is found. This did not improve when the reaction conditions under which the thiol monolayers were formed were strictly controlled. Although this variation of the cyclovoltammograms was observed at any type of thiol–modified electrodes, the reproducibility was found to be good enough to differentiate between thiols of different chain length and, in most cases, with different terminal groups. The variation between the cyclovoltammograms is mainly due to the sensitivity of the current–potential measurements for small differences in the thiol monolayer. Especially at cathodic potentials with respect to the overpotential, the current is a very sensitive
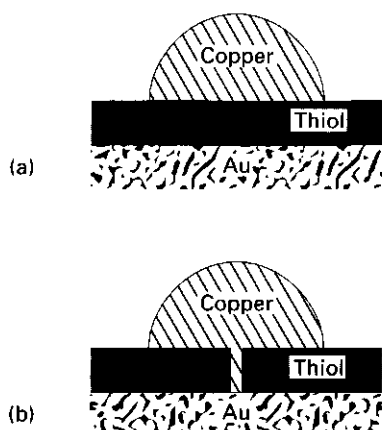
Figure 8.3: Schematic representation of galvanic copper deposition on gold modified with a monolayer alkanethiol. In (a) the copper is deposited on top of the thiol layer and electron transport occurs through the thiol layer. In (b) the copper makes electric contact with the gold via pinholes in the monolayer that are filled with copper.

parameter and may vary considerably. Small microscopic deviations in surface composition or ordering will then have large effects on the metallization behaviour.

The poor reproducibility is not observed with macroscopic characterization techniques like wetting and differential capacitance measurements. According to these measurements, the individual samples with the same thiols virtually behave identically. Apparently, these macroscopic measurements are not sensitive enough to detect microscopic differences in monolayer properties, whereas metallization does.

Adhesion between the Cu–particles and the thiol monolayer is poor, independent of the thiol chain length or type of terminal group X. Although no systematic adhesion measurements have been carried out yet it was found that, simply by touching the particles with a tissue or by rinsing the substrate with water, particles could be removed. The poor adhesion was also observed when the working electrode was placed vertically instead of horizontally. In that case the particles tended to move downwards along the electrode's surface under gravity. This poor adhesion points to small chemical interactions between the Cu deposit

and the thiol monolayer. In contrast, the adhesion between a copper film and bare gold was very good. In that case, we never observed any mechanical removal of copper.

8.3.2. Influence of thiol chain length

Some characteristics of the alkanethiol ($HS(CH_2)_{n-1}CH_3$ with $n = 12, 18, 22$) monolayers adsorbed on gold are given in Table 8.1. This table shows the advancing (θ_a) and receding (θ_r) contact angle measured with water and the total differential capacitance C_t. As we have shown in ref. 14, C_t is almost independent of the applied potential. In Table 8.1 the minimum C_t values are given. The total capacitance is almost equal to the capacitance of the thiol layer C_i [22]. The capacitance of the thiol layer is inversely proportional to the thickness δ of the thiol layer and directly proportional to the dielectric constant ε_r of the thiol layer: $C_i = \varepsilon_0\varepsilon_r/\delta$ [22]. The capacitance was measured at a frequency of 10 Hz but is almost frequency independent [22].

Table 8.1: Characteristics of thiol monolayers adsorbed on gold in 10^{-2} M K_2SO_4 [14,28]

| Thiol	θ_a (deg) [†]	θ_r (deg) [†]	C_t (μF cm^{-2})
$HS(CH_2)_{11}CH_3$	112	88	1.1
$HS(CH_2)_{17}CH_3$	117	90	0.7
$HS(CH_2)_{21}CH_3$	117	88	0.6
$HS(CH_2)_{11}Cl$	95	80	1.3
$HS(CH_2)_{11}OH$	24	<5	1.9
$HS(CH_2)_{11}CN$	69	51	2.1
$HS(CH_2)_{10}COOH$	45	<5	2.1

[†]measured with water; standard deviation ±3°

The cyclovoltammograms for Cu deposition on alkanethiol (abbreviated as C_n thiol) modified gold electrodes of different chain lengths are given in Figure 8.4. The scanning range was between 0.5 and –0.15 V(SCE) (Figure 8.4a) or between

0.5 and −0.3 V(SCE) (Figure 8.4b). In both figures a distinct but different influence of the chain length on the cyclovoltammograms can be observed. In Figure 8.4a the current density at a given potential is higher for shorter chains. This is also the case in Figure 8.4b in the potential range between 0.04 and about −0.2 V(SCE) but the sequence changes when the potential becomes more negative. The capacitance of the monolayers appeared to be unaffected after these scans.
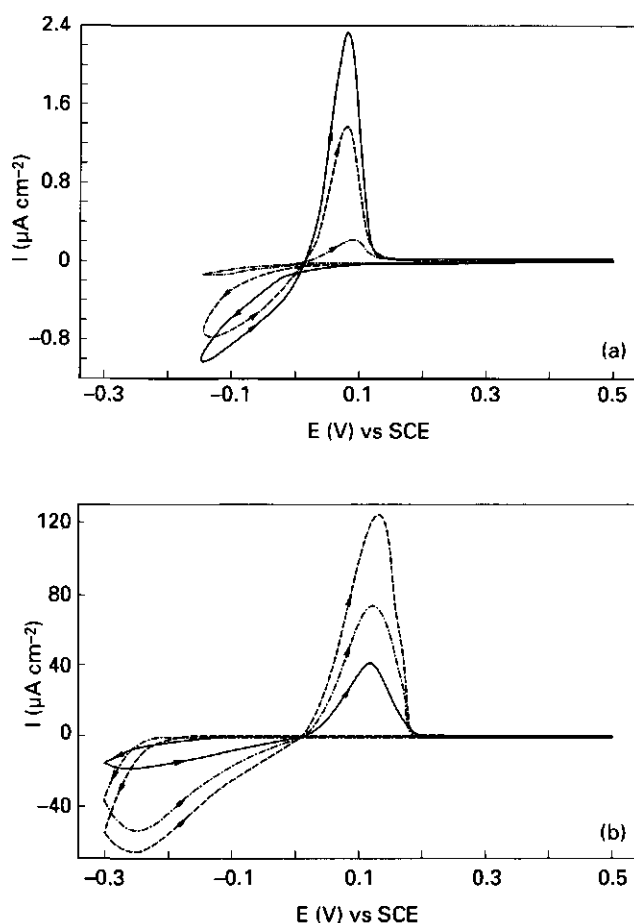
Figure 8.4: Cyclovoltammograms of gold electrodes modified with a monolayer of $HS(CH_2)_{11}CH_3$ (———), $HS(CH_2)_{17}CH_3$ (---), and $HS(CH_2)_{21}CH_3$ (−·−·−), respectively, in 10^{-2} M $CuSO_4$, 10^{-2} M H_2SO_4. The scan rate was 10 mV s^{-1}. (a) Cathodic scan limit −0.15 V(SCE), (b) cathodic scan limit −0.3 V(SCE).
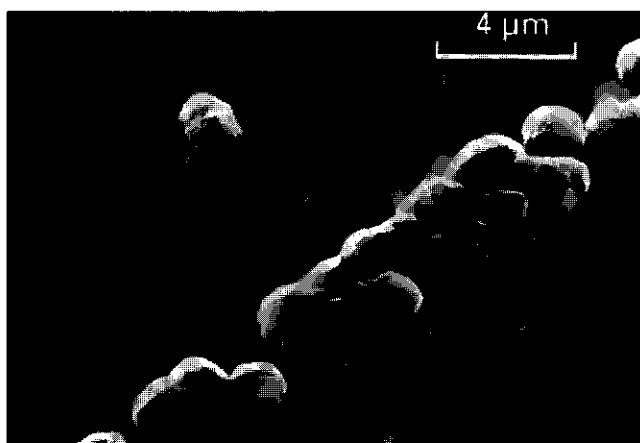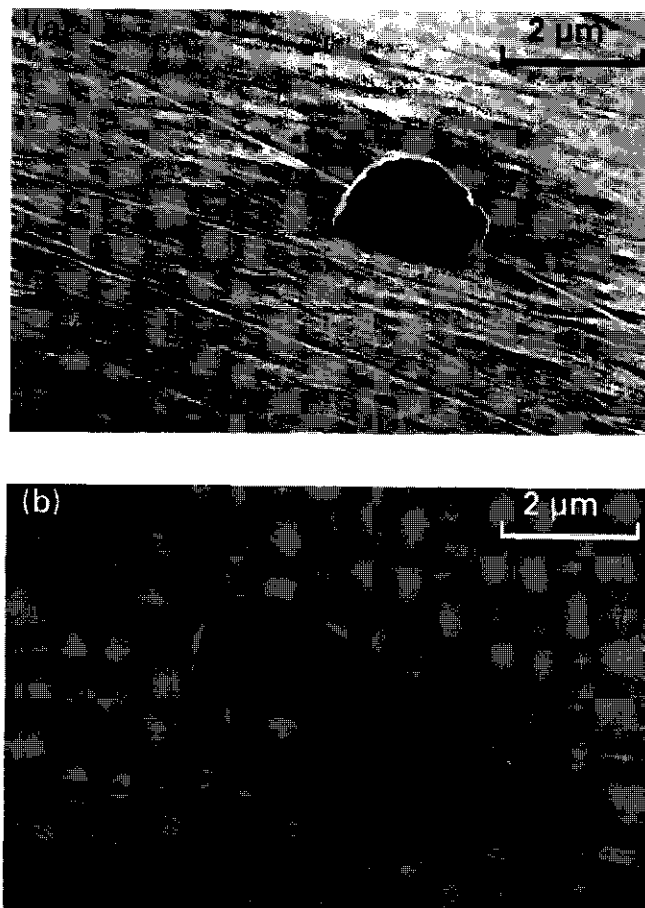
Figure 8.5: Scanning electron micrograph (under an angle of 45°) of galvanically deposited copper on a $HS(CH_2)_{11}CH_3$–modified gold electrode from 10^{-2} M $CuSO_4$, 10^{-2} M H_2SO_4. Deposition conditions: potential scan from 0.5 V(SCE) to –0.15 V(SCE) with a scan rate of 10 mV s^{-1} subsequently a potential step to –0.1 V(SCE) and keeping the potential at this value for 3 min. Under these conditions Cu deposition occurs on defects like scratches in the gold.

In Figure 8.4a it can be observed that for the C_{12} thiol monolayer a (small) cathodic current already flows at a potential just negative of the Nernst potential. In order to understand the differences between the curves, the following potential step experiment was carried out. First, the potential was scanned with a scan rate of 10 mV s^{-1} from 0.5 to –0.15 V(SCE). Then the potential was stepped to –0.1 V(SCE) and kept at that value for several minutes in order to allow growth of the nuclei formed during scanning. At –0.1 V(SCE) it is assumed that no new nuclei are formed and only existing nuclei grow. Afterwards the deposits were imaged by SEM. It was found that for the C_{12} thiol monolayer Cu had grown preferentially on a few defect sites, like scratches in the underlying gold. A typical example is shown in Figure 8.5. No Cu is found on other positions. On the C_{18} and C_{22} thiol layer hardly any copper could be found. Roughened gold, like the gold in the scratches, may induce disorder in the monolayer. Apparently, the relatively thin C_{12} thiol layer is not able to completely shield the underlying gold in these disordered areas. The copper will be deposited first on these defect sites. The current flow just negative of the Nernst potential indicates that defects

containing no or only small amounts of thiol are present in the C_{12} thiol monolayer: the electron transfer is not blocked. However, these currents are only small. The current density for C_{12} thiol-modified gold and bare gold differ by more than a factor of 100 at -0.1 V(SCE). Therefore, the number of defects is only small. The fact that on the C_{18} and C_{22} thiol monolayer hardly any copper could be found and that the current density is lower than for C_{12} thiol (see Figure 8.4a), indicates that these longer chains are better able to mask these defects. This shielding is more effective for longer alkane chains so that the current density is reduced, as is evident from Figure 8.4a. We like to emphasize that the defects present in the C_{12} thiol monolayer as discussed above are more or less macroscopic in nature. These defects should not be confused with the microscopic pinholes as discussed in the previous section and shown in Figure 8.3b.

The thickness of the monolayers also has its effect on the cyclovoltammograms when scanning between 0.5 and -0.3 V(SCE) (Figure 8.4b). The shape of the curve for the C_{12} thiol monolayer deviates from those of C_{18} and C_{22} thiol. According to our definition of the overpotential, a distinct overpotential can be determined for the C_{18} and C_{22} thiol layer, whereas for the C_{12} thiol layer it is very difficult to define an overpotential. For C_{18} thiol η is about -210 mV and for C_{22} thiol η is about -270 mV.

The differences between the cyclovoltammograms may be caused by differences in morphology of the Cu deposits. To check whether this is the case again an additional potential step experiment was carried out. For this purpose the potential was first scanned from 0.5 to -0.3 V(SCE) with a scan rate of 10 mV s^{-1}. Then the potential was stepped to -0.1 V(SCE) in order to allow growth of the nuclei formed in the scan during a period of 3 min without the possibility of new particles being formed. Afterwards the particle density and the shape and size of the particles was determined by optical and scanning electron microscopy. The amount of copper deposited as estimated from the SEM images always agreed with the amount of copper as determined from the charge passed during deposition.

Figure 8.6: Scanning electron micrographs (under an angle of 80°) of galvanically deposited copper from 10^{-2} M $CuSO_4$, 10^{-2} M H_2SO_4 on (a) a $HS(CH_2)_{11}CH_3$–modified gold electrode and (b) on a $HS(CH_2)_{21}CH_3$–modified electrode. Deposition conditions: potential scan from 0.5 to –0.3 V(SCE) with a scan rate of 10 mV s^{-1} and subsequently a potential step to –0.1 V(SCE) and keeping the potential at this value for 3 min.

We found that independent of the thiol chain length, hemispherical particles were formed. The diameter of the particles are about the same for every chain length tested. The results of the two extremes, the "short" C_{12} thiol and the "long" C_{22} thiol monolayers are given in Figure 8.6 and Table 8.2. The only difference between the copper deposits on the two monolayers is the particle density which

is determined with optical microscopy (Table 8.2): more particles are deposited on the C_{22} thiol than on the C_{12} thiol monolayer. In conclusion, the morphology of the Cu deposits does not account for the difference between the cyclovoltammograms.

Table 8.2: Characteristics of galvanically deposited copper particles on thiol–modified gold electrodes. The deposition conditions were scanning in 10^{-2} M $CuSO_4$, 10^{-2} M H_2SO_4 from 0.5 to –0.3 V(SCE) with a scan rate of 10 mV s^{-1}, subsequently a potential step to –0.1 V(SCE) and keeping the potential at this value for 3 min.

Thiol	Particle density (cm^{-2})	Particle diameter (µm)
$HS(CH_2)_{11}CH_3$	2×10^4	2.0–2.8
$HS(CH_2)_{21}CH_3$	5×10^4	2.4–2.8
$HS(CH_2)_{11}OH$	4×10^6	1.0–2.2

We ascribe the differences between the cyclovoltammograms to a difference in potential drop across the dielectric of the thiol layer as is schematically shown in Figure 8.7. Due to this potential drop, the potential at the thiol/electrolyte interface ϕ_d is much lower than the applied potential at the gold/thiol interface, ϕ_m. Let us first consider the cyclovoltammograms of the C_{22} and the C_{18} thiol monolayers where a distinct overpotential could be determined. For the C_{22} thiol layer the potential drop is larger than for the C_{18} thiol. This is caused by the fact that the capacitance of the C_{22} thiol is smaller than of the C_{18} thiol layer, because of the larger thickness of the self–assembled monolayer (Table 8.1). The dielectric constant of the alkanethiol monolayer is equal for the C_{12}, C_{18} and C_{22} thiol monolayers and is about 2 [22]. Hence, the potential drop per unit length is equal for both layers. At the same applied potential, the potential at the thiol/electrolyte interface (experienced by the Cu^{2+}–ions at that position) is smaller for longer thiol chain lengths. Consequently, a higher overpotential is required for deposition on a C_{22} as compared to a C_{18} thiol monolayer.

The critical potential η_d^c with respect to the Nernst potential at the thiol/electrolyte interface necessary for Cu deposition can be calculated following
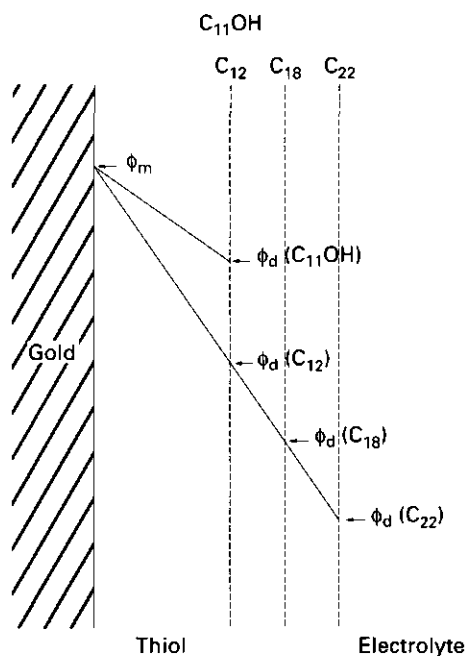
Figure 8.7: Schematic representation of the potential drop across a $HS(CH_2)_{11}CH_3$ (C_{12}), $HS(CH_2)_{17}SH$ (C_{18}), $HS(CH_2)_{21}CH_3$ (C_{22}) or $HS(CH_2)_{11}OH$ ($C_{11}OH$) *modified gold electrode in an electrolyte. The applied potential at the gold/thiol interface is* ϕ_m *and the potential at the thiol/electrolyte (——) interface is* ϕ_d *with respect to the Nernst potential. The potential drop depends on the thiol chain length and on the dielectric constant of the thiol layer.*

the procedure given in ref. 28. In summary, in this procedure the overall capacitance of the electrical double layer is integrated with respect to E resulting in the charge density of the diffuse double layer. Subsequently, the Poisson–Boltzmann equation is used to calculate the potential at the thiol/electrolyte interface. The potential at the thiol/electrolyte interface is about 2% of the applied potential for the C_{18} thiol and 1.5% for the C_{22} thiol [22]. Thus, η_d^c for the C_{18} thiol monolayer becomes $-210\times2\% = -4$ mV. For the C_{22} thiol monolayer the same value is found: $-270\times1.5\% = -4$ mV. Apparently, a critical overpotential of about -4 mV at the thiol/electrolyte interface is required for deposition of Cu to occur on top of the hydrophobic CH_3–terminated thiol.

From Figure 8.7 it can also be deduced that the quality of the self–assembled monolayer plays an important role in nucleation. At sites on the surface where the monolayer is less ordered or has a lower packing density, the capacitance is expected to be higher due to a higher dielectric constant or a lower thickness of the thiol layer. Hence, at these sites the potential at the thiol/electrolyte interface is higher than at non–defect sites. Consequently, the nucleation at these defect sites will occur at a lower overpotential. This makes the nucleation a very sensitive means to test the (microscopic) quality of the monolayer. The above may also account for the cyclovoltammogram of the C_{12} thiol monolayer. The C_{12} thiol is just long enough to produce an ordered monolayer. Hence, it is expected that relatively more defects such as disordered areas are present in this monolayer compared to the C_{18} and C_{22} thiol monolayers. These defect sites should be considered as areas where the monolayer is relatively "thin" (see Figure 8.7). At these defect sites nucleation will start at a lower overpotential than at non–defect sites. Once nuclei are present on these defects, most of the Cu^{2+} ions will be reduced here instead of on the hydrophobic thiol. Consequently, less particles are formed on the C_{12} thiol monolayer. Because the number of particles is less on this surface, the current density will also be less as is indeed observed in the cyclovoltammogram.

If Cu is not deposited in pinholes but rather on top of a thiol layer, electron transport through the monolayer is necessary for the reduction of Cu^{2+} to occur. One of the transport mechanisms may be electron tunneling. Whether this is possible depends on the alkane chain length [18]. From the oxidation/reduction of ferrocene(Fc)–terminated alkanethiol monolayers it is known that electrons are indeed able to pass through the alkane tail [23–25]. It is found, quite surprisingly, that even for the long Fc–terminated hexadecanethiol the Fc group can be reduced and oxidized [25]. Therefore, we believe that electrons do indeed pass through the thiol layer and reduce the Cu^{2+} ions at the thiol/electrolyte interface. The exact electron transport mechanism is unknown to us.

There is no conclusive indication that the overpotentials can also be ascribed to the "penetration mechanism". If penetration of Cu ions is required in order to reduce the ions at the Au/electrolyte interface (Figure 8.3b) one would expect

a destructive effect of the penetration into the monolayer. Then it would be expected that in a second scan the overpotential would have been strongly reduced. Such an effect was not observed as long as the total charge involved in deposition, Q_d, remained below 500 µC cm^{-2}. Moreover, if pinholes would be the preferred nucleation sites, a strong and specific effect of the chain length on the overpotential is to be expected. In that case the shape of the cyclovoltammograms for electrodeposition on the C_{18} and C_{22} thiol monolayer would not be similar. However, although we do not believe that the overpotential is determined by the "penetration–mechanism", we found that when larger amounts of Cu are deposited ($Q_d > 1000$ µC cm^{-2}, which corresponds to deposition of about 0.3 nm of Cu) Cu nuclei may penetrate the thiol layer. In that case it is found that Q_d is larger than the charge involved in stripping, Q_s. It is not possible to strip the relatively large amounts of copper instantaneously when scanning in the anodic direction. The copper which remains after stripping serves as growth nuclei in the second and following scans. Due to this residue of copper the overpotential becomes less and the current density increases. The reason that (some) copper remains at the electrode when relatively large amounts of copper have been deposited may be that the copper has then already penetrated the thiol layer. Such penetration was also found when metal is vapour–deposited on thiol monolayers [26–31]. For example, penetration of Cu into a $HS(CH_2)_{11}CN$ monolayer is found to occur when the thickness of the deposited layer is larger than about 0.1 nm [26]. Similarly, penetration into a $HS(CH_2)_{11}OH$ monolayer takes place when the thickness is larger than 0.5 nm [27]. In our case we find a comparable thickness where Cu starts to penetrate the monolayer (≈ 0.3 nm). Once Cu has penetrated the monolayer, it may be shielded by the thiol tails, and therefore it will be difficult to strip.

On the reverse scan in Figure 8.4b from –0.3 V(SCE) to the Nernst potential, the Cu–deposition continues. It is expected that in the potential range between the overpotential and Nernst potential no new nuclei are formed. Only existing nuclei grow. Apparently, no overpotential is required for growth on nuclei, even with a thiol layer between the copper deposit and the gold substrate. This is explained by the fact that the Cu deposition occurs on a Cu surface and thus continues until the equilibrium potential is reached. Scanning further in positive

direction with respect to the Nernst–potential, the copper is stripped. Because the copper is stripped from copper particles, no overpotential for stripping is required.

8.3.3. Influence of terminal group

The influence of the type of terminal group of a functionalized alkanethiol ($HS(CH_2)_{n-1}X$, with X = OH, CN, Cl, CH_3 and n = 12 or X = COOH with n = 11) adsorbed on gold on the galvanic copper deposition process was tested. Some relevant characteristics of the thiol layers are given in Table 8.1.

The cyclovoltammograms for Cu deposition on the functionalized alkanethiol monolayers are given in Figure 8.8. For ease of comparison, the cyclovoltammogram of the C_{12} thiol monolayer (X = CH_3, n = 12) is reproduced in this figure. Figure 8.8a shows scans between 0.5 and –0.15 V(SCE) and Figure 8.8b and c those between 0.5 and –0.30 V(SCE). The standard deviation is about 30%. When scanning to –0.15 V(SCE) (Figure 8.8a), it follows that the largest cathodic current flows when Cu is deposited on the OH–terminated thiol layer. This current flows at any potential negative of the Nernst potential for Cu deposition (at 40 mV(SCE)). The total anodic current involved in stripping the Cu from this substrate is much lower. Probably, a parasitic Faradaic current is included in the cyclovoltammogram. This effect is not observed for the other functionalized thiol layers. Apparently this Faradaic current is catalyzed by the OH–group. We assume that, despite that fact that we used deaerated electrolyte, the parasitic current is due to the reduction of oxygen taking place at a potential of about 0 V(SCE). The magnitude of charge involved in the anodic stripping of Cu is $Q_s^{CH3}>Q_s^{OH}>Q_s^{Cl}\approx Q_s^{COOH}\approx Q_s^{CN}$.

The deposition of Cu on the CH_3–thiol is compared with that on the OH–thiol by scanning from 0.5 to –0.15 V(SCE) and then stepping to –0.1 V(SCE) and keeping the potential at that value for several minutes. We observed that where Cu on CH_3–thiol is mainly deposited on (macroscopic) defects, the nucleation
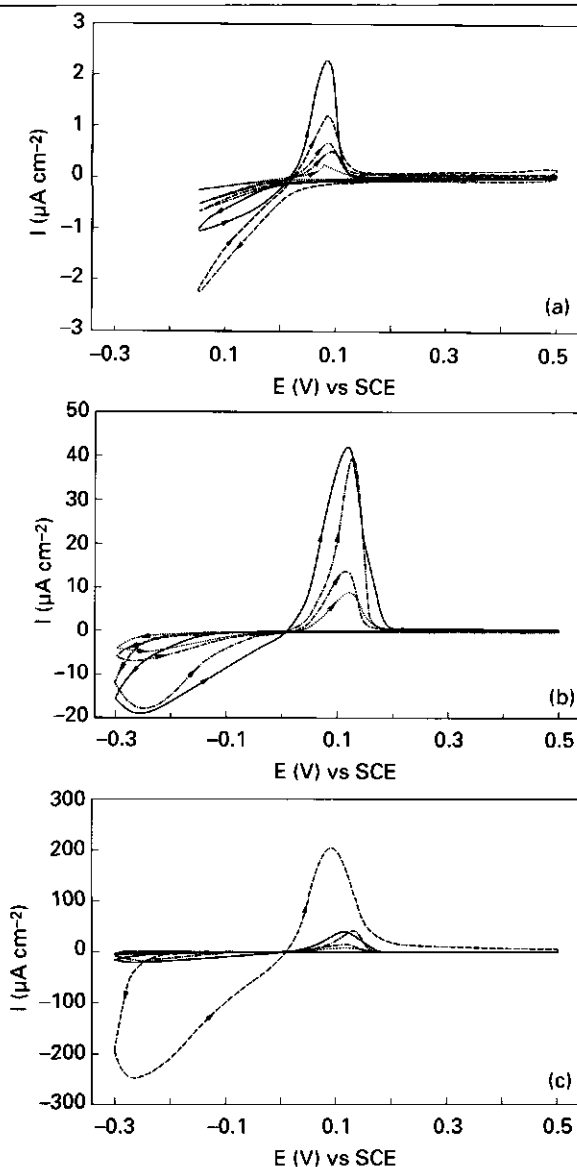
Figure 8.8: Cyclovoltammograms of gold electrodes modified with a monolayer of
$HS(CH_2)_{11}CH_3$ (———), $HS(CH_2)_{11}OH$ (---), $HS(CH_2)_{10}COOH$ (–·–·–), $HS(CH_2)_{11}Cl$
(····) and $HS(CH_2)_{11}CN$ (–··–··–), respectively in 10^{-2} M $CuSO_4$, 10^{-2} M H_2SO_4.
The scan rate was 10 mV s^{-1}. (a) Cathodic scan limit is –0.15 V(SCE), (b) and (c)
cathodic scan limit is –0.3 V(SCE). Figure (b) does not contain the cyclovoltammogram
for the OH–terminated monolayer.

on the OH–thiol is just beginning to occur as hemispherical particles in a few areas on the surface.

When scanning the potential to –0.3 V(SCE) (Figure 8.8b,c) we observed that the cyclovoltammogram of the OH–terminated thiol layer strongly deviates from the other groups. The OH–thiol monolayer has a definite overpotential for nucleation which is about –240 mV. At more negative potentials, the negative current increases very sharply (Figure 8.8c). Because the cyclovoltammogram of this monolayer strongly deviates from those of the other monolayers, a potential step measurement was carried out where the potential was first scanned from 0.5 to –0.3 V(SCE) and then stepped to –0.1 V(SCE) and kept there for 3 min. Two SEM images of the deposits after this experiment are shown in Figure 8.9. Figure 8.9a and 8.9b are images of the same sample. When these results are compared with the results obtained under the same conditions for the CH_3–terminated thiol layers (Figure 8.6), it is found that the shape of the particles on the two different types of monolayers are about the same. The number and size of the particles differ significantly, though. The particle density is about a factor of 100 larger than for the CH_3–terminated thiol (Table 8.2). This feature explains why the cyclovoltammogram for the OH–terminated monolayer deviates so strongly from that of the CH_3–thiol.

As discussed before, one of the factors governing the overpotential is the capacitance of the thiol layer, or in other words, the potential drop across this layer. Despite the similar chain lengths of the C_{12} thiol and the OH–terminated thiol, it is found that the capacitances of these layers differ by a factor of nearly 2 (Table 8.1) which is caused by a difference in ε_r of these layers [14]. Due to the higher capacitance of the OH–thiol, the potential drop across the monolayer is less for the OH–thiol. This is schematically illustrated in Figure 8.7. The potential remaining at the OH/electrolyte interface is about 5% of the applied potential. Hence, η_d^c follows as: $-240 \times 5\% = -12$ mV. For the C_{12} thiol no clear overpotential was found probably due to the role of defects as discussed before. However, on the other two CH_3–terminated surfaces the η_d^c value could be determined and was –4 mV. This is much lower than on the OH–terminated surface.
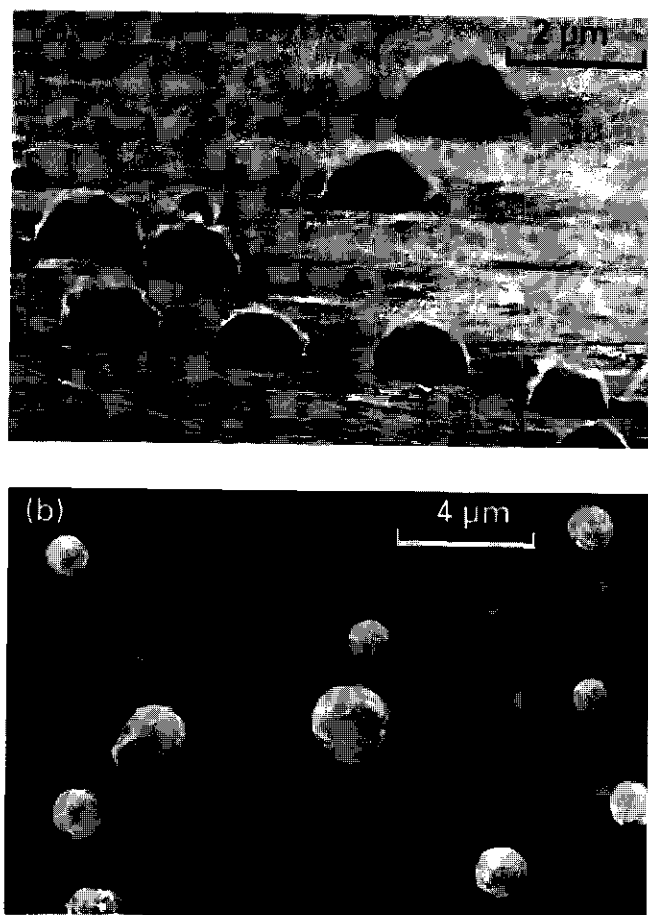
Figure 8.9: Scanning electron micrograph of galvanically deposited copper from 10^{-2} M $CuSO_4$, 10^{-2} M H_2SO_4 on a $HS(CH_2)_{11}OH$–modified gold electrode. Deposition conditions: scanning from 0.5 to –0.3 V(SCE) at a scan rate of 10 mV s^{-1}, subsequently a potential step to –0.1 V(SCE) and keeping the potential at this value for 3 min. (a) Side view taken under an angle of 80° and (b) top view taken under an angle of 0°.

The question is what factors cause the difference in particle density and η_d^c. In electrocrystallization, diffusion of ions to the electrodes and incorporation of ad–atoms (formed after the reduction of ions) at lattice sites are often considered to be crucial steps for growth [20]. Diffusion becomes the growth rate determining step when the number of nuclei is high and the electrolyte

concentration relatively low. This will be the case under many deposition conditions. In our case ion diffusion limitation is not very likely: the current–potential curves are all very steep at potentials negative of the overpotential. If diffusion limitation would occur, a plateau in the current would have been expected. Incorporation of ad–atoms at lattice sites may also influence the nucleation as is, for example, found for the nucleation of PbO_2 on C–microelectrodes [4]. If this were to be the most important step in our case, no effect of the thiol terminal group would be expected. Hence, neither explanation accounts satisfactorily for observation made in this study. We propose that surface diffusion of ad–atoms is an important factor in the nucleation on thiol-modified electrodes.

In vacuum deposition studies of Cu onto self–assembled thiol monolayers on gold it is deduced from X–ray photoelectron spectroscopy that Cu interacts with several terminal groups of the thiol layers [26–30]. Relatively strong interactions of Cu with the OH and COOH group are reported. Copper reacts with OH and COOH to give Cu–oxide [27] and Cu(II)carboxylate [28], respectively. For the Cu deposition on CH_3–terminated monolayers no reactions occur [32].

Due to the interactions of Cu with the monolayers, surface diffusion of ad–atoms will be hindered. When there is no interaction, as for Cu–CH_3, the surface diffusion is fast. The ad–atoms try to cluster in the form of nuclei in order to reduce the contact area with the CH_3 surface and to increase the favourable cohesive Cu–Cu interactions. Due to this fast surface diffusion, a relatively small number of large particles are formed. When the interaction between the terminal group and Cu is strong, as is apparently the case for OH–Cu, surface diffusion will be much slower. Since all the adsorbed Cu ad–atoms can in principle serve as nuclei, the particle density may become much larger on the OH–surface. This also affects the nucleation overpotential. At this potential the total free energy involved to form a bulk phase and a new surface has reached its maximum so that (thermodynamically) stable nuclei with a certain critical radius are formed on the surface [20,21]. Consequently, the growth will continue spontaneously at potentials negative of this overpotential. The critical radius depends on the interfacial tension γ of the three phases involved (Cu, thiol, and electrolyte (*el*)):

$\gamma_{thiol-Cu}$, $\gamma_{thiol-el}$, and γ_{Cu-el}. Because the interfacial tension γ_{Cu-el} of the newly formed interface is much larger than the interfacial tension $\gamma_{thiol-el}$ of the disappearing interface (independent of X, as will be discussed in the next section), the critical radius is mainly determined by γ_{Cu-el}. Hence, the critical radius is comparable for the nucleation on CH_3– and OH–terminated surfaces under the same nucleation conditions. Because for the CH_3 thiol layer critical nuclei are expected to be formed very easily due to the fast surface diffusion, nucleation on this thiol layer starts at a lower (critical) potential than at the OH–surface.

Apart from the chemical effect that influences the particle density, there is also an effect of the capacitance of the thiol layer. The number of particles is related to the applied overpotential [21]. At the same applied potential of –300 mV(SCE), for example for the C_{22} and OH–thiol monolayers η_d is about $(-300-40) \times 1.5\% = -5$ mV for the C_{22} thiol monolayer and about $(-300-40) \times 5\% = -17$ mV for the OH–thiol monolayer. Due to this larger potential at the thiol/electrolyte interface, the particle density will also be larger.
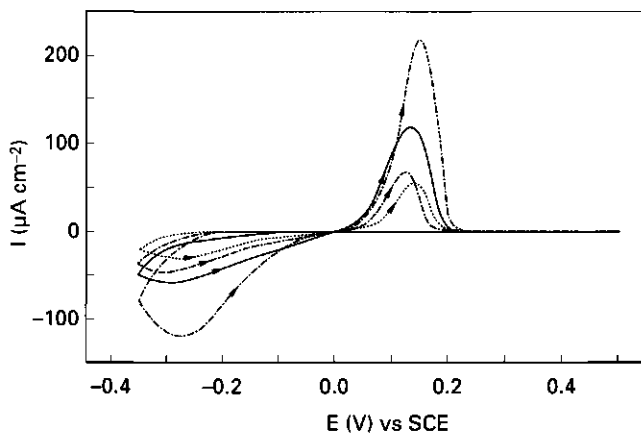
Figure 8.10: Cyclovoltammogram of gold electrodes modified with a monolayer of $HS(CH_2)_{11}CH_3$ (——), $HS(CH_2)_{10}COOH$ (–·–·–), $HS(CH_2)_{11}Cl$ (····) and $HS(CH_2)_{11}CN$ (-·--·-), respectively in 10^{-2}M $CuSO_4$, 10^{-2} M H_2SO_4. The scan rate was 10 mV s^{-1}. The cathodic scan limit is –0.35 V(SCE).

Although Cu is known to form strong bonds with the COOH–group, the cyclovoltammogram in Figure 8.8c does not differ strongly from the

cyclovoltammogram of the CH_3–group. However, when scanning the potential up to –0.35 V(SCE) the cyclovoltammogram of the COOH thiol starts to deviate from those of the Cl, CN and CH_3 terminated thiol. This is shown in Figure 8.10. In this figure the cyclovoltammogram of the OH–terminated thiol is not shown because of the relatively large current density. From the COOH–curve an overpotential for Cu deposition on a COOH thiol layer of about –260 mV can be deduced. For this thiol the potential at the thiol/electrolyte interface for this thiol is calculated [22] to be about 5.3% of the applied potential; η_d^c = –260×5.3% = –14 mV. It may also be that this relatively high value of η_d^c is due to a strong interaction of Cu with the COOH groups, which is likely to be even stronger than the interaction with the OH groups [27]. It may also be that this large η_d^c for Cu deposition is influenced by reduction of the COOH groups of the thiol layer. Earlier, we found that at pH≈6 COOH is cathodically reduced at about –0.2/–0.3 V(SCE), to give the aldehyde compound HC=O [14]. As a second step HC=O may be reduced at about –0.6/–0.7 V(SCE) to a methyl-hydroxy group. This reduction is only partial: about 5–10% of the carboxyl groups are reduced. In the present electrolyte solution, the pH is 1.7. The reduction potential thus shifts with respect to the reduction potentials at pH≈6 by about (6–1.7)×60 mV = +260 mV. Such a shift is indeed found for the reduction of COOH to HC=O (not shown). In the present system, reduction takes place at about 0/0.1 V(SCE). However, this reduction is not reversible. Apparently, the interaction of Cu with the carbonyl groups formed is strong enough to prevent oxidation of the HC=O to COOH. It may be that the second reduction step of HC=O to CH_2OH occurs at about –0.35/–0.45 V(SCE). This reduction is difficult to observe in the cyclovoltammogram because at this potential also the reduction of large amounts of copper starts. As for the pure OH–thiol monolayer it is expected that if COOH is (partly) reduced to CH_2OH, this formation of OH groups in the COOH monolayer enhances the formation of Cu nuclei on this surface.

In Figure 8.10 it can be observed that the differences between the cyclovoltammograms of the CH_3, Cl and CN thiol monolayers are not very large. It is difficult to define an overpotential for these layers because no potential can be found where the current density sharply increases. It might be that these

monolayers contain more defects, such as disordered areas, than the OH and COOH terminated monolayers. Nucleation will then preferentially occur on these defects. The effect of defects on the nucleation will probably be reduced when longer chain X–terminated thiol layers are used.

8.3.4. Morphology of deposited metal

The shape of the Cu–particles deposited on the hydrophobic CH_3–terminated thiol and on the hydrophilic OH–terminated thiol do not differ markedly (compare Figure 8.6 and 8.9), despite the higher affinity of Cu for the OH–group and despite the difference in wettability and therefore in surface tension [33] between the two surfaces. In order to understand this phenomenon, we use a model of the kinetics of the nucleation process developed by Volmer and Weber [34] and elaborated by Deutscher and Fletcher [21]. In this model it is assumed that the microscopic deposits have the same properties as the bulk material. Three phases are involved in the deposition: phase 1 is the nucleated phase, phase 2 is the electrode surface and phase 3 is the electrolyte from which deposition occurs (see Figure 8.11). According to this model interfacial tensions determine the shape of the deposit. The interfacial tensions are assumed to be independent of both the crystallographic orientation and the curvature. Phase 1 is treated as if it were a liquid drop. Any surface stress arising from incoherency
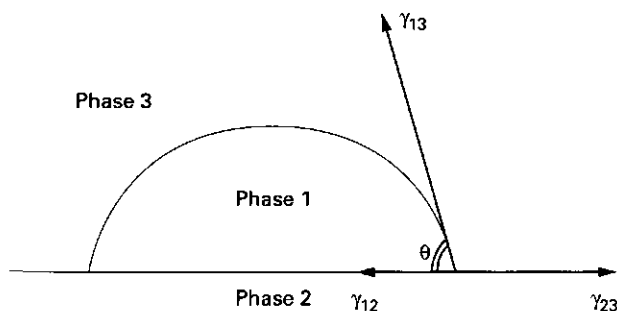
Figure 8.11: Nucleation of a solid (phase 1) on a solid electrode (phase 2) in an electrolyte solution (phase 3) [27]. Phase 1 makes an angle of $\theta°$ with the surface of phase 2. The symbols γ_{12}, γ_{13}, and γ_{23} are the interfacial tensions with respect to the 1/2, 1/3 and 2/3 interfaces, respectively.

of the two solid phases 1 and 2 is neglected. These assumptions result in the following equation [21]:

$$\cos\theta = \frac{\gamma_{23} - \gamma_{12}}{\gamma_{13}} \qquad (8.1)$$

where θ is the angle at the junction between the three phases as indicated in Figure 8.11. This equation is the Young equation which is normally only applied to liquid drops on solid surfaces. For our situation, where Cu is deposited on the thiol–modified electrode from an electrolyte (*el*), equation 1 becomes:

$$\cos\theta = \frac{\gamma_{thiol-el} - \gamma_{thiol-Cu}}{\gamma_{Cu-el}} \qquad (8.2)$$

The surface tension of the thiol/electrolyte interface is known for the CH_3–terminated thiol: $\gamma_{thiol-el} \approx 50$ mN m^{-1} [17]. For the OH–terminated thiol $\gamma_{thiol-el}$ is unknown, but following the procedure in [33] where γ of the solid/liquid interface is deduced from θ, $\gamma_{thiol-el} = 0.54$ mN m^{-1}. The surface tension of the thiol/Cu interface is expected to be of the same order of magnitude as the thiol/electrolyte interface. The surface tension of the copper/electrolyte interface is taken to be comparable to the surface tension of the copper/vapour interface. The latter is relatively large (>1000 mN m^{-1} [35]). Consequently, θ is largely determined by γ_{Cu-el}. Due to the fact that γ_{Cu-el} is very large, $\cos\theta$ is close to zero, and thus $\theta \approx 90°$, largely independent of the terminal group of the thiol layer. Such an angle of about 90° is indeed observed for both the OH– and the CH_3–terminated thiol layer.

Generally, equation 1 suggests that only on surfaces with a very high surface tension (comparable with the surface tension of the metal deposit), flat and homogeneous metal films can be deposited [21]. In that case $\gamma_{23} \approx \gamma_{13}$ resulting in $\cos\theta \approx 1$ and $\theta \approx 0°$, and hence a flat metal film is obtained. This is indeed observed for many metal deposits on other metal substrates like Cu on Au. In the latter case even UPD occurs. For metal deposition on plastics, such a situation can be obtained by pretreating the surface with oxygen or nitrogen plasmas [36].

8.4. Conclusions

The presence of a self–assembled thiol monolayer ($HS(CH_2)_{n-1}X$ with $X = CH_3$ and $n = 12, 18, 22, X = OH, CN, Cl$ and $n = 12$ or $X = COOH$ and $n = 11$) on a gold electrode strongly affects the morphology of galvanically deposited copper. On the thiol–modified gold copper is deposited as hemispherical particles whereas on bare gold, copper is deposited as a rather homogeneous flat film. The morphology of the particles is nearly independent of the type of terminal group of the thiol. The difference in morphology of the copper deposit is a result of the difference between the surface tension of the Cu and the Au or thiol monolayer, respectively. For Cu deposition on the thiol–modified electrode, the interfacial tension of the copper in contact with electrolyte γ_{Cu-el} is much larger than the interfacial tension of the thiol/electrolyte interface $\gamma_{thiol-el}$. This is true for all terminal groups of the thiol tested. The fact that $\gamma_{Cu-el} \gg \gamma_{thiol-el}$ results in Cu particles exhibiting a contact angle of about 90° with the thiol–surface regardless of the type of functional group. For copper deposition on bare gold, the interfacial tension of both the Au and the Cu with electrolyte are high and of comparable magnitude. In that case flat and homogeneous films are formed. The general conclusion is that when a metal is deposited onto another material, two–dimensional films can be obtained only when the surface tension of that material is high. This conclusion is relevant for many industrial applications.

The chain length of the adsorbed alkanethiol largely determines the overpotential required for Cu deposition on the thiol as long as the monolayer is ordered and free of defects. Nucleation is believed to occur on top of the thiol layer. The overpotential increases with increasing thiol chain length and is about –210 mV for C_{18} thiol and –270 mV for C_{22} thiol. The influence of the chain length on the overpotential is ascribed to the substantial potential drop across the dielectric of the thiol layer. The potential remaining at the thiol/electrolyte interface as experienced by the Cu^{2+} ions is only small. This potential drop increases with increasing thiol chain length. Consequently, larger potentials have to be applied in order to obtain the same potential at the thiol/electrolyte interface. The potential at the thiol/electrolyte interface with respect to the Nernst potential

where nucleation on top of the CH_3–terminated thiol monolayer starts, η_d^c, is calculated to be –4 mV and is found to be independent of the chain length. The mechanism responsible for the electron transport through the thiol layer is presently unknown to us. For nucleation on the short chain C_{12} thiol layer no distinct overpotential could be determined. This is ascribed to the presence of defects like disordered areas, that may be present in this relatively thin layer.

The reproducibility of the cyclovoltammograms of copper deposition on the thiol layers is only moderate. This is very likely to be due to the fact that the current–potential measurements are extremely sensitive for small microscopic differences in the quality of the thiol monolayer: small deviations in structure of the monolayer cause considerable differences in the potential drop across the thiol layer and thus in the overpotential. Additional measurements such as in–situ electrochemical STM are required to confirm this hypothesis. Despite variations in the cyclovoltammograms, the reproducibility of macroscopic characterization techniques like wetting and differential capacitance measurements is good. Hence, galvanic copper deposition is a very sensitive method to monitor the quality of the self–assembled thiol monolayer.

The terminal group strongly influences the characteristics of galvanic copper deposition. This is evidenced most pronouncedly for the OH–terminal group. The overpotential is about the same as for the CH_3–terminated thiol ($\approx$–240 mV). However, due to a higher dielectric constant of the thiol layer, this overpotential corresponds to a higher η_d^c value (–12 mV). The reason for this higher η_d^c is likely due to the higher affinity of Cu for OH. This leads to a slower surface diffusion of Cu ad–atoms formed after reduction of Cu^{2+}. Consequently, relatively small (but numerous) Cu clusters are formed on the OH–surface whereas on the CH_3–surface much larger (and fewer) clusters are obtained. Hence, at the OH–surface higher overpotentials are required to obtain nuclei with a critical size which are (thermodynamically) stable. A secondary effect of the difference in affinity is that the number of particles on OH–terminated thiol is larger than on CH_3–terminated thiol. Upon scanning from 0.5 V(SCE) to –0.3 V(SCE) in 10^{-2} M $CuSO_4$, about 100 times more particles are formed on OH–terminated thiol as compared to CH_3–terminated thiol.

As for the C_{12} thiol, no clear overpotential could be defined for Cu deposition on CN– and Cl–terminated thiols ($n = 12$), which is believed to be due to the presence of defects in these monolayers. In order to concentrate on the effect of the terminal groups on metallization, it is advisable to use well–ordered longer chain thiol monolayers.

References

[1]   Gabe, D. *Principles of metal surface treatment and protection*; Pergamon Press, 1978.
[2]   Marrian, C.R.K.;Perkins, F.K.; Brandow, S.L.; Koloski, T.S.; Dobisz, E.A.; Calvert, J.M. *Appl. Phys. Lett.* **1994**, *64*, 390–392.
[3]   Sondag–Huethorst, J.A.M.; van Helleputte, H.R.J.; Fokkink, L.G.J. *Appl. Phys. Lett.*, **1994**, *63*, 285–287 and references therein and chapter 9, this thesis.
[4]   Li, L.J.; Fleischmann, M.; Peter, L.M. *Electrochim. Acta*, **1989**, *34*, 459–474.
[5]   *Metallization of Polymers*; Sacher, E.; Pireaux, J.J.; Kowalczyk, S.P., Eds; ACS Symposium Series; Washington DC, 1990, Vol 40.
[6]   For an overview see: Ulman, A. *An introduction to ultrathin organic films from Languir–Blodgett to Self–assembly*; Academic Press, San Diego, 1991, Ch. 3.
[7]   Porter, M.D.; Bright, T.B.; Allara, D.L.; Chidsey, C.E.D. *J. Am. Chem. Soc.* **1987**, *109*, 3559–3568.
[8]   Bain, C.D.; Throughton, E.B.; Tao, Y.–T.; Evall, J.; Whitesides, G.M.; Nuzzo, R.G. *J. Am. Chem. Soc.* **1989**, *111*, 321–335.
[9]   Dubois, L.H.; Zegarski, B.R.; Nuzzo, R.G. *J. Chem. Phys.*, **1993**, *98*, 678–688.
[10]   Schönenberger, C.; Sondag–Huethorst, J.A.M.; Jorritsma, J,; Fokkink, L.G.J. *Langmuir* **1994**, *10*, 611–614.
[11]   Nuzzo, R.G.; Dubois, L.H.; Allara, D.L. *J. Am. Chem. Soc.* **1990**, *112*, 558–569.

[12]   Dubois, L.H.; Zegarski, B.R.; Nuzzo, R.G. *J. Am. Chem. Soc.* **1990**, *112*, 570–579.
[13]   Chidsey, C.E.D.; Loiacono, D.N. *Langmuir* **1990**, *6*, 682–691.
[14]   Sondag–Huethorst, J.A.M.; Fokkink, L.G.J. manuscript submitted to Langmuir and chapter 6, this thesis.
[15]   Sondag–Huethorst, J.A.M.; Schönenberger, C.; Fokkink, L.G.J. *J. Phys. Chem.* **1994**, *98*, 6826–6834, and chapter 3, this thesis.
[16]   Schönenberger, C.; Jorritsma, J.; Sondag–Huethorst, J.A.M.; Fokkink, L.G.J. submitted to J. Phys. Chem.
[17]   Sondag–Huethorst, J.A.M.; Fokkink, L.G.J. *Langmuir* **1992**, *8*, 2560–2566, and chapter 4, this thesis.
[18]   Miller, C.; Cuendet, P.; Grätzel, M. *J. Phys. Chem.* **1991**, *95*, 877–886.
[19]   Throughton, E.B.; Bain, C.D.; Whitesides, G.M.; Nuzzo, R.G.; Allara, D.L.; Porter, M.D. *Langmuir* **1988**, *4*, 365–385.
[20]   For an overview see: *Intrumental methods in electrochemistry*; Kemp, T.J. Ed.; Ellis Horwood, Chichester, 1990.
[21]   Deutscher, R.L.; Fletcher, S. *J. Electroanal. Chem.* **1990**, *277*, 1–18.
[22]   Sondag–Huethorst, J.A.M.; Fokkink, L.G.J. *J. Electroanal. Chem.* **1994**, *367*, 49–57, and chapter 5, this thesis.
[23]   Collard, D.M.; Fox, M.A. *Langmuir* **1991**, *7*, 1192–1197.
[24]   Chidsey, C.E.D.; Bertozzi, C.R.; Putvinski, T.M.; Mujsce, A.M. *J. Am. Chem. Soc.* **1990**, *112*, 4301–4306.
[25]   Sondag–Huethorst, J.A.M.; Fokkink, L.G.J. *Langmuir*, **1994**, *10 (12)* (in press) and references therein, and chapter 7, this thesis.
[26]   Jung, D.R.; King, D.E.; Czanderna, A.W. *J. Vac. Sci. Technol. A* **1993**, *11*, 2382–2386.
[27]   Jung, D.R.; King, D.E.; Czanderna, A.W. *Appl. Surf. Sci.* **1993**, *70/71*, 127–132.
[28]   Czanderna, A.W.; King, D.E.; Spaulding, D. *J. Vac. Sci. Technol. A* **1991**, *9*, 2607–2613.
[29]   Herdt, G.C.; Czanderna, A.W. *Surf. Sci. Lett.* **1993**, *297*, L109–L112.
[30]   Smith, E.L.; Alves, C.A.; Anderegg, J.W.; Porter, M.D.; Siperko, L.M. *Langmuir* **1992**, *8*, 2707–2714.
[31]   Tarlov, M.J. *Langmuir* **1992**, *8*, 80–89.
[32]   Spaulding, D.; Master's thesis., U. Denver, CO, 1989.
[33]   Neumann, A.W.; Absolom, D.R.; Francis, D.W.; van Oss, C.J. *Sep. Purif. Sci.* **1980**, *9*, 69.
[34]   Volmer, M.; Weber, A. *Z. Phys. Chem. (Leipzig)* **1926**, *119*, 277–301.
[35]   *Handbook of Chemistry and Physics*; Lide, D.R., Ed.; CRC Press, USA, 71st edition, 1990.
[36]   Gerenser, L.J. *J. Vac. Sci. Technol. A* **1988**, *6*, 2897–2903.

Chapter 9

Generation of electrochemically deposited metal patterns by means of electron beam (nano)lithography of self-assembled monolayer resists[1]

Abstract: Submicron metal patterns have been produced by galvanic deposition in openings in a monolayer resist generated by electron beam (e–beam) lithography. The monolayer resist is a self-assembled docosanethiol ($C_{22}H_{45}SH$) layer adsorbed on gold. Proper removal of the thiol requires an e–beam dose of 10–100 mC cm^{-2}. The positive resist pattern was used to selectively deposit galvanic copper. The size of the Cu patterns is affected by the galvanic deposition time and the $CuSO_4$ concentration in the electrolyte solution. The smallest Cu patterns produced were about 75 nm in width.


9.1. Introduction

Recently, self-assembled monolayers (SAMs) have been applied for the generation of patterns with different structures or surface properties. There are a number of techniques to generate such patterns: laser-desorption [1], micromachining [2], microwriting [3], scanning probe lithography [4], and electron-beam (*e*–beam) lithography [5]. For submicron patterns, *e*–beam lithography forms a very promising technique. The ultimate resolution is limited by the spot diameter of the *e*–beam, the forward scattering of electrons in the resist and backward scattering from the substrate. The forward scattering may be reduced by using ultrathin resist layers [5]. We used self-assembled thiol monolayers adsorbed on gold as positive or negative resists in *e*–beam lithography. These thiol layers are known to be very densely packed and ordered [6,7].

To obtain information about the line width of the patterns after *e*–beam
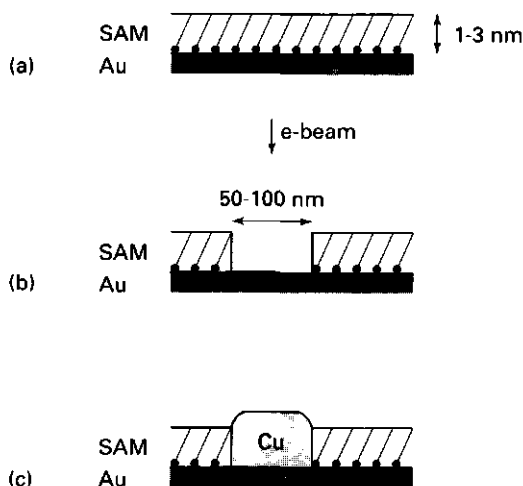
Figure 9.1: Schematic illustration of the formation of metal patterns in a self-assembled monolayer resist structure on gold. The lithographic process sequence is: (a) deposition of the self-assembled monolayer, (b) exposure by a scanning *e*–beam, (c) galvanic metal deposition in the openings in the monolayer.

exposure, we used a Scanning Electron Microscope (SEM). Due to the contrast difference between the exposed and unexposed area, the line width in the SAM can be determined [8]. However, this contrast difference can not be taken as a prove for the complete removal of the thiol. Additional information on removal can be obtained by etching the patterns [5] or by galvanic deposition of metal on the uncovered gold. In general, both techniques are also applicable for SAMs on substrates other than Au, for example Si, Al or GaAs. In the present work we used a galvanic metal deposition technique to demonstrate the successful resist removal by *e*–beam exposure. Figure 9.1 describes the process. Combining galvanic deposition and *e*–beam lithography offers the possibility to selectively produce metal structures. These small metal structures may offer interesting applications in technologies such as ultra high density recording or disk mastering.

9.2. Experimental

Materials. Docosanethiol ($C_{22}H_{45}SH$) and nonadecenethiol ($CH_2=CHC_{17}H_{34}SH$) were prepared following literature procedures (supplementary material to ref. 9). The gold films were prepared by evaporation of gold (99.999%) onto single crystal silicon(111) wafers that had been precoated by a 5 nm chromium adhesion layer. After evaporation, the wafers were broken into samples of about 1×1 cm^2. Detailed information about the preparation of the monolayers is given in chapter 2.

E–beam. Within 1 day after adsorption of a thiol monolayer on gold, the samples were exposed to the *e*–beam. Equidistantly spaced lines with four different design widths (10 nm, 100 nm, 400 nm and 1 µm) were delineated in the thiol using a Gaussian spot, vector–scan *e*–beam exposure system (Cambridge Instr. EBPG 4V–HR). Exposure was carried out at an accelerating voltage of 50 keV using a pixel grid of 5 nm for the 10 and 100 nm design widths, corresponding to patterns of 2 and 20 pixels wide. Typical beam current was 52 pA, corresponding to a 50 nm calculated spot size implying that the width of the

smallest line in the thiol will not be determined by the design but by the spot size. For the 400 nm design width a 50 nm pixel grid was used with a beam current of 820 pA (65 nm diameter spot size) and for the 1 μm design width the pixel grid was 250 nm and the beam current 16 nA (280 nm diameter spot size). The e–beam exposure dose was varied between 0.1 and 10^5 mC cm^{-2}.

Electrochemistry. Electrochemical experiments were carried out in a single-compartment three–electrode glass cell containing a saturated calomel reference electrode (SCE), a Pt counter electrode and the thiol-modified gold working electrode. The deoxygenated electrolyte consisted of 10^{-2} or 10^{-3} M CuSO$_4$ in 10^{-2} M H$_2$SO$_4$. The copper deposition was controlled with a potentiostat (Schlumberger 1186 EI/Hi–Tek Instruments PP RI potentiostat) by pulsing from 0.5 V(SCE) to a potential negative to the equilibrium potential during t min. After deposition, the sample was rinsed with water. Due to the hydrophobic character of the sample, it was immediately dry after rinsing.

Microscopy. The e–beam exposed and the Cu patterns were imaged by optical microscopy and by Scanning Electron Microscopy (SEM, Philips SEM 515).

9.3. Results and discussion

9.3.1. SEM images of patterns in the monolayers

The SEM appeared to be very sensitive to differences in contrast between the e–beam exposed and unexposed areas. The exposed areas (where the thiol monolayer is removed), were always darker than the unexposed areas. A typical SEM image showing the contrast between exposed and unexposed areas is shown in Figure 9.2. The 10 nm e–beam design width exposed with a dose of 10 mC cm^{-2} results in a 40 nm line width whereas 100 mC cm^{-2} yields a 60 nm line width, in good agreement with the spot size of 50 nm.

Whitesides and coworkers [8] showed that the brightness of the SEM images is also a function of the thiol chain length: the longer the chain the brighter the
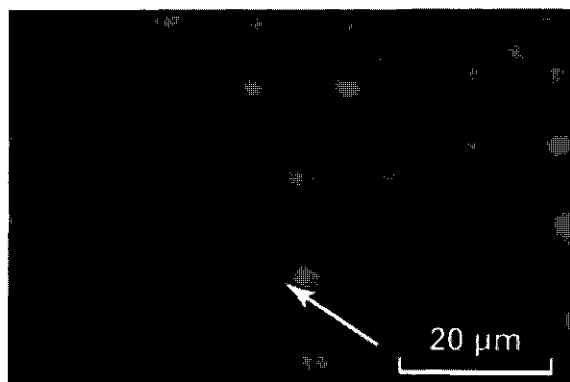
Figure 9.2: Scanning electron micrograph of patterns generated with *e*–beam on a $C_{22}H_{45}SH$-modified Au electrode. The *e*–beam dose was 100 mC cm^{-2} and the design widths were 1 µm (left and right patterns), 100 nm (middle-top patterns) and 10 nm (middle-bottom patterns, indicated with a white arrow), respectively.

image. This is in agreement with our results: the longer the thiol chain the better the shielding of the underlying gold surface.

9.3.2. Negative resist pattern

By using $CH_2=CHC_{17}H_{34}SH$ as a monolayer resist, we tried to polymerize the double bond of the thiol with the *e*–beam so as to use the thiol layer as a negative resist. The polymerized thiol should remain after removal of the non-polymerized thiol. However, after exposing the alkenethiol layer to different *e*–beam doses, the same behaviour as for the $C_{22}H_{45}SH$ monolayer was observed: they both behave as positive resists. The double bonds do not seem to polymerize, but rather complete thiol molecules are removed upon exposure.

9.3.3. Selective galvanic metallization

Selective galvanic metallization of the uncovered Au features is only possible if *(i)* the thiol layer is stable under the applied electrochemical conditions, *(ii)* the

exposed pattern remains unchanged for sufficient long periods of time, and *(iii)* no metal deposition occurs on the thiol covered surface.

(i) From electrochemical studies it has been determined that the self-assembled thiol layer is stable in a large electric potential region between hydrogen and oxygen evolution [6]. Electrochemical desorption of the layer is only found at extreme potentials [6,11].

(ii) The Cu patterns deposited immediately after *e*–beam exposure were identical to those deposited 2 days after exposure, indicating that lateral diffusion of thiol into the *e*–beam pattern (which would block the Cu deposition) is slow.

(iii) Galvanic metal deposition is possible on top of the thiol layers. However, a large overpotential with respect to the bare Au is required. Figure 9.3 shows a cyclic voltammogram where the current density *I* is shown as a function of the scanning potential *E*. Cu deposition occurs when *I*<0 and Cu stripping occurs when *I*>0. Scanning in negative potential direction, bulk Cu is deposited on Au at a potential negative of about 0 V (SCE) while a potential negative of about –0.2 V(SCE) is required for the deposition on a docosanethiol covered gold surface. Therefore, in the potential window between 0 and –0.2 V(SCE) Cu deposition occurs on the clean Au only.
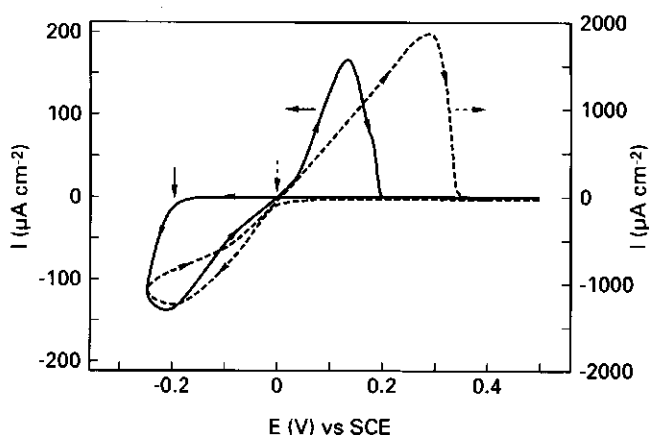
Figure 9.3: Cyclic voltammograms of a bare Au electrode (dashed curve, right hand axis) and of a $C_{22}H_{45}SH$-modified Au electrode (solid curve, left hand axis) in 10^{-2} M $CuSO_4$, 10^{-2} M H_2SO_4. The scan rate was 10 mV s^{-1}. Galvanic deposition starts for potentials *E* negative than indicated by the vertical arrows (where the current *I* becomes negative).

9.3.4. E–beam dose

On substrates exposed to an *e*–beam dose of 10 or 100 mC cm^{-2} well-defined Cu patterns could be deposited, except for the smallest (10 nm) designed pattern, where a minimum dose of 100 mC cm^{-2} was required. A dose of 10 mC cm^{-2} equals about 100 electrons per removed thiol molecule. The dose is about a factor 100–1000 larger than the dose required to remove self-assembled octadecanethiol molecules from a GaAs(100) substrate [5]. The difference is presumably due to the relative instability of the As–S bond. Oxidation of the GaAs underneath the thiol layer occurs over the course of hours [5] whereas the thiol layers on gold remain stable in air for periods of at least one weak. Apparently, the bonding between the As–S is relatively weak compared to the Au–S bond and the dose required to remove thiol from GaAs is lower.
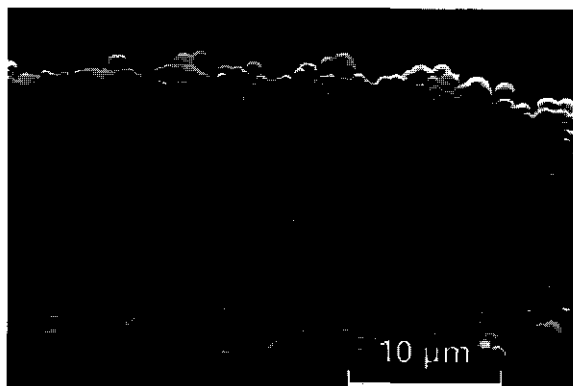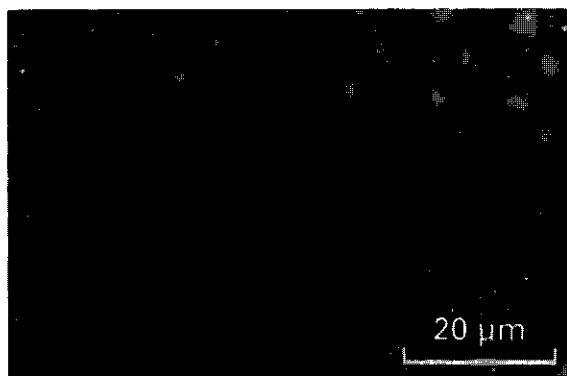

Figure 9.4: Scanning electron micrograph of Cu deposited after exposure of the C$_{22}$H$_{45}$SH thiol layer on gold to a high dose *e*–beam (1 C cm^{-2}). The Cu was deposited from a 10^{-2} M CuSO$_4$ (in 10^{-2} M H$_2$SO$_4$) solution at –0.2 V(SCE) during 3 min. The design width of the lines was 500 nm, the length was 10 μm, and the period of the grating was 5 μm. Due to the scattering of the electrons, a much larger area is exposed to the *e*–beam.

A dose smaller than 10 mC cm^{-2} did not remove sufficient thiol to allow proper Cu deposition. A dose higher than 100 mC cm^{-2} resulted in very broad patterns, as is shown in Figure 9.4. In this image 7 lines were exposed to the *e*–beam. The Cu is deposited everywhere except for on the exposed lines. Due to the

scattering of the electrons, effectively a much larger area is exposed to the *e*–beam. Consequently, the thiol is removed from a much larger area. However, no Cu growth is observed on the lines where the *e*–beam was focused on. Apparently, due to the exposure of the high dose *e*–beam, some insulating material is deposited preventing the Cu to be deposited. This may be carbon–like material which is left after decomposition of the thiol.


Figure 9.5: Scanning electron micrograph of a clean Au substrate after *e*–beam exposure with dose 1 C cm^{-2}. The design width was 500 nm (upper patterns) and 10 nm (lower patterns), respectively. After Cu deposition from a 10^{-2} M CuSO$_4$ (in 10^{-2} M H$_2$SO$_4$) solution (–0.025 V(SCE), 1 min), no Cu was observed near these patterns. Only in a larger area around the patterns Cu was deposited (some white spots (i.e. Cu particles) can be observed).

The remaining material after high dose *e*–beam exposure could also be observed when a clean gold substrate was exposed to the *e*–beam (see Figure 9.5). After exposure, dark lines were observed with SEM. Cu deposition hardly occurred in the area close to the exposed area but only in a larger area surrounding the exposed area. Clearly some material is deposited after the exposure preventing Cu deposition. Because no thiol was present on the substrate, the deposited material will be a result from the (very small) amount of organics present in the vacuum chamber of the *e*–beam system. Although the high *e*–beam dose in fact produces negative resist patterns, these patterns are not useful as resists because they are very wide (> 1 μm) and ill-defined.

9.3.5. Electrochemical deposition conditions

Patterns made with doses of 10 and 100 mC cm^{-2} were used to study the influence of the electrochemical deposition conditions (i.e. the electrical deposition potential, the deposition time and the $CuSO_4$ concentration) on the quality and the width of the resulting Cu patterns. Cu patterns were successfully grown at potentials ranging from −0.15 to −0.2 V(SCE). Potentials between 0 and −0.15 V(SCE) only incidently resulted in deposition of Cu on the exposed *e*−beam pattern. Often an incomplete Cu pattern was observed (see Figure 9.6). This is probably due to contaminations on the clean Au pattern that to some degree block the Cu deposition. The contaminants may be airborne or may consist of incompletely removed thiol. As expected from the cyclic voltammogram (Figure 9.3), potentials lower than −0.2 V(SCE) resulted in Cu deposition on both the exposed pattern and the thiol layer, albeit that the structure of the deposits differs markedly for both types of surface (chapter 8).
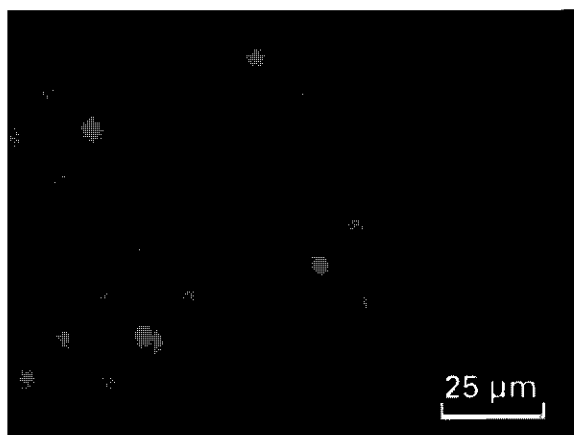
Figure 9.6: Optical micrograph of Cu deposited from a 10^{-2} M $CuSO_4$ (in 10^{-2} M H_2SO_4) solution at −0.1 V(SCE) during 10 min. The *e*−beam dose was 10 mC cm^{-2}, design width of the two patterns was 1 μm and the length 50 μm. Due to the small overpotential, the deposition is not complete.

The degree of overgrowth of the original line width can be controlled by the Cu deposition time. Figure 9.7 shows an overgrown Cu pattern deposited from a
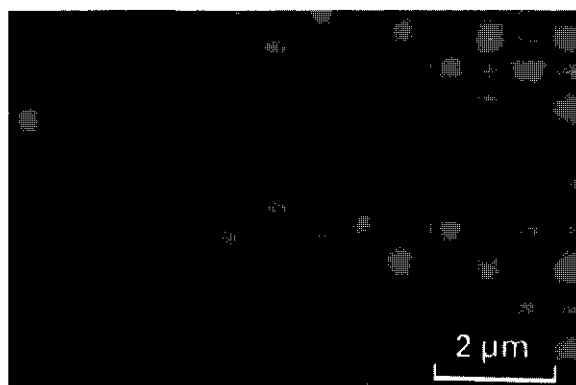
Figure 9.7: Scanning electron micrograph of an overgrown Cu pattern deposited from a 10^{-2} M CuSO$_4$ (in 10^{-2} M H$_2$SO$_4$) solution at –0.2 V(SCE) during 3 min. The substrate was a C$_{22}$H$_{45}$SH-modified Au electrode. The *e*–beam dose was 100 mC cm^{-2} and the design width was 400 nm. The width of the Cu pattern is almost twice the height plus the design width (400 nm), indicating that the Cu growth is isotropic.

10^{-2} M CuSO$_4$ solution on a 400 nm *e*–beam design width. The growth of the Cu is isotropic: the width of the Cu pattern (≈ 2.5 μm) is about twice the height (≈ 1.1 μm) plus the design width (400 nm). Shorter deposition times indeed reduced the width and height of the Cu lines. However, even for short deposition times like 15 s overgrowth of the patterns occurred.

Smaller Cu patterns were deposited by reducing the CuSO$_4$ concentration to 10^{-3} M. Typical examples of the resulting Cu deposits are shown in Figure 9.8. In order to prove the presence of Cu, several samples were treated in a UV/ozone reactor which removes the organic thiol monolayer [6]: the SEM showed almost identical images before and after removal. The somewhat irregular shape of the Cu patterns is characteristic for galvanic Cu deposition from the present solution. Figures 9.8a and 9.8b show the same samples, before and after evaporation of a thin Au layer (15 nm) for better conductivity. In Figure 9.8a the SEM contrast is given by the material contrast. After Au evaporation the topographic contrast becomes more pronounced (Figure 9.8b) with respect to the material contrast. Figure 9.8c shows a 75 nm Cu pattern before evaporation of gold. After evaporation the pattern disappeared into the bulk Au film, illustrating the
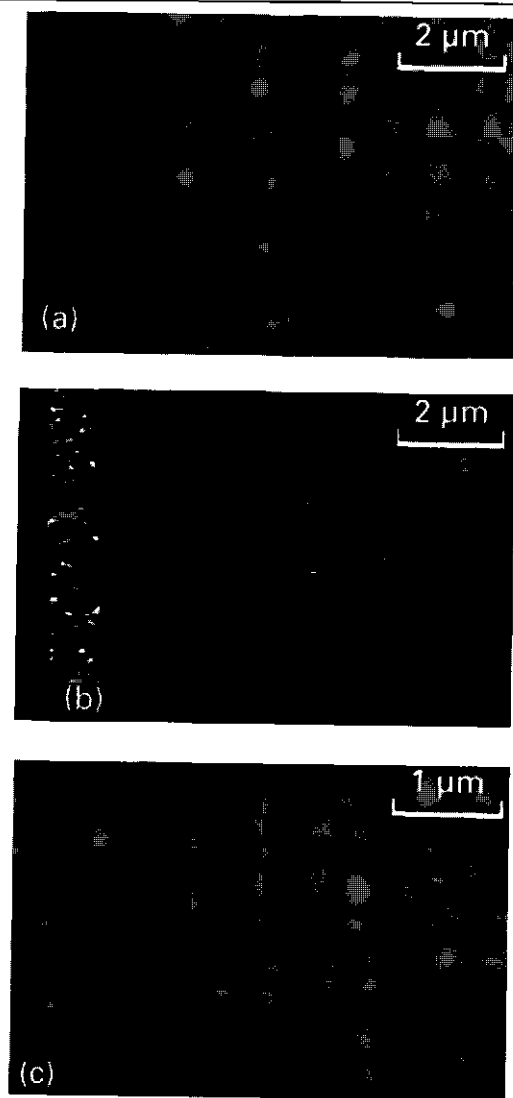
Figure 9.8: Scanning electron micrographs of Cu patterns deposited from a 10^{-3} M CuSO$_4$ (in 10^{-2} M H$_2$SO$_4$) solution at a potential of –0.2 V(SCE) during 1 min (a,b) and 30 sec (c). The *e*–beam dose was 100 mC cm^{-2}. The design width was for (a,b) 1 μm (left) and 10 nm (right) and for (c) 10 nm. Image (b) shows the same sample as (a) after evaporation of a thin Au layer (15 nm).

thinness of the pattern. The width of the Cu pattern is almost as small as the original line width observed by SEM (60 nm). The ultimate resolution of the Cu

patterns in our experiments is determined by the spot size of the *e*–beam and not by the galvanic deposition conditions.

9.4. Conclusions

The work presented in this chapter demonstrates that self-assembled monolayers can be used as a positive resist for producing well-defined metal patterns. The docosanethiol monolayer adsorbed on gold can be selectively removed with an *e*–beam with a dose of 10–100 mC cm^{-2}. The SEM appeared to be a very useful tool in imaging the *e*–beam exposed patterns before and after Cu deposition. The smallest width of the Cu patterns deposited galvanically after removal of the thiol with the *e*–beam was about 75 nm. This width is determined by the spot size of the *e*–beam. We believe that smaller patterns are possible by optimizing the *e*–beam exposure. Further work should be carried out to evaluate the ultimate limit for galvanic deposition of metal patterns by *e*–beam lithography.

References

[1]   Takehara, K.; Yamada, S.; Ide, Y. *J. Electroanal. Chem.* **1992**, *333*, 339–344.

[2]   Abbott, N.L.; Folkers, J.P.; Whitesides, G.M. *Science* **1992**, *257*, 1380–1382.

[3]   Kumar, A.; Biebuyck, H.A.; Abbott, N.L.; Whitesides, G.M. *J. Am. Chem. Soc.* **1992**, *114*, 9188–9189.

[4]   Ross, C.B.; Sun, L.; Crooks, R.M. *Langmuir* **1993**, *9*, 632–636.

[5]   Tiberio, R.C.; Craighead, H.G.; Lercel, M.; Lau, T.; Sheen, C.W.; Allara, D.L. *Appl. Phys. Lett.* **1993**, *62*, 476–478.

[6]   *(a)* Sondag–Huethorst, J.A.M.; Fokkink, L.G.J. *Langmuir*, **1992**, *8*, 2560–2566 and chapter 4, this thesis. *(b)* Sondag–Huethorst, J.A.M.; Fokkink, L.G.J. *J. Electroanal. Chem.* **1994**, *367*, 49-57 and chapter 5, this thesis.

[7]   *(a)* Porter, M.D.; Bright, T.B.; Allara, D.L.; Chidsey, C.E.D. *J. Am. Chem. Soc.* **1987**, *109*, 3559–3568. *(b)* Ulman, A. *An introduction to ultrathin organic*

films; Academic Press, 1991, and references cited in there.

[8] López, G.P.; Biebuyck, H.A.; Whitesides, G.M. *Langmuir* **1993**, *9*, 1513–1516.

[9] Bain, C.D; Troughton, E.B.; Tao, Y.–T.; Evall, J.; Whitesides, G.M.; Nuzzo, R.G. *J. Am Chem. Soc.* **1989**, *111*, 321–335.

[10] Kim, Y.–T.; McCarley, R.L.; Bard, A.J. *Langmuir* **1993**, *9*, 1941–1944.

[11] Widrig, C.A.; Chung, C.; Porter, M.D. *J. Electroanal. Chem.* **1991**, *310*, 335–359.

Chapter 10

Conclusions and outlook

Abstract: In this chapter a discussion is given of the work described in the previous chapters about self–assembled thiol monolayers on gold electrodes. The conclusions on the experimental chapters are split into two parts. First, the most pertinent results of the subsequent chapters will be discussed and compared with the current status of knowledge in the literature. Subsequently, new insights into the structure of the monolayer will be discussed. This chapter ends with some suggestions for further research.

10.1. New insights

10.1.1. General

In this thesis, the application of STM with atomic resolution using extremely high tunnel resistances ($\approx T\Omega$) is described. Using these high tunnel resistances, we were able to elucidate the nature of the mysterious holes observed in self-assembled monolayers in previous STM studies. In those studies the holes were proposed to be either empty holes in the monolayer, areas with disordered thiol molecules or holes in the underlying gold layer. Our STM images, obtained at ultrahigh resistance, revealed that the molecules on Au(111) arrange themselves in ($\sqrt{3}\times\sqrt{3}$)R30° domains which is in agreement with earlier results from electron diffraction and helium diffraction. However, these domains are separated by different type of rows with molecules missing from the ordered structure. The ordered structure is maintained in the holes. Hence, it was concluded that the holes are depressions due to holes in the underlying Au. The presence of gold in the thiol solution led to the conclusion that the latter holes are mainly caused by an etching process. We systematically studied this erosive behaviour and found that there is a direct correlation between the number of holes and the amount of gold measured in the thiol solution after adsorption. The fact that the

holes are due to the underlying gold is important for applications of the thiol monolayer in fundamental studies and in technology: if these holes, which occupy 5–40% of the surface, would have been genuine defects in the thiol layer, this layer would be useless for many applications. Further details on the structure of self-assembled monolayers will be presented in paragraph 10.1.2.

Next, we focused on the effect of the electrical potential on the wettability of the self-assembled monolayers. The earliest comprehensive investigation of potential–dependent wetting or electrowetting is that by Lippmann for mercury in contact with an electrolyte solution. Scattered data are available for other liquid metal phases, like various amalgams or liquid gallium. Measuring the electrowettability of solid metals is, in principle, also possible by using a Wilhelmy plate technique as presented in chapter 4. However, almost all clean metals are hydrophilic so that no differences in electrowettability can be observed. By modifying a metal with an organic monolayer or even by thicker layers, the metal can be made hydrophobic and the electrowettability effect can be determined. We reported results for the potential–dependent wetting of gold electrodes modified with a self–assembled thiol monolayer. The electrowetting is due to changes in the electrical double layer. Experimental electrowetting effects could be conveniently described by (classical) interfacial thermodynamics. Understanding electrowetting is not only interesting from a fundamental point of view. By variation of the potential, the wettability of a surface can be controlled which is of potential interest for many technological applications.

A second method to change the wettability is by oxidation/reduction of the surface. The oxidation and reduction of a terminal group of a self–assembled ferrocene-terminated monolayer was described in the literature several years ago. Recently, Whitesides et al. showed that oxidation/reduction also has consequences for the wettability of this system. We elaborated this idea in some detail and concluded that the electrowetting effect is large and (partly) reversible. The reversibility is limited by contact angle hysteresis. The change in wetting was shown not to be caused by changes in the electrical double layer, like is the case for alkanethiols ($HS(CH_2)_{n-1}CH_3$), but by specific interactions of the oxidized ferrocene ion with anions from the electrolyte. The stability of the

monolayer upon continuous oxidation/reduction is considerably improved by mixing the ferrocenethiol with an unsubstituted alkanethiol of about the same chain length. This feature could be used to increase the electrowetting effects even more.

We have shown that metals can be galvanically deposited onto a self–assembled monolayer. This may seem strange in view of the numerous publications about the ability of monolayers to block the oxidation/reduction of redox couples present in solution. However, we found that metal deposition does occur, provided a sufficiently high potential, which should exceed a certain overpotential, is applied.

The electrodeposition of copper on self–assembled thiol monolayers provided new insights into the role of the substrate on the morphology of the deposited metal. It was concluded that only when the surface tension of the substrate is high, flat and homogeneously deposited films can be obtained. For metal deposition on plastics this situation may be achieved by pretreating the surface with an oxygen or nitrogen plasma. When the surface tension of the substrate is relatively low, the metal is deposited as individual particles.

10.1.2. Structure of the self–assembled monolayer

The present study provided new insights into the structure of self–assembled thiol monolayers on gold. As discussed in the previous section, STM with high tunnel resistances showed that the observed holes are depressions in the underlying gold. The sulphur atoms of the thiol molecules arrange themselves in $\sqrt{3} \times \sqrt{3}$ domains, separated by different rows of missing molecules. These microscopic measurements provide only information about the ordering of the sulphur atoms, and (unfortunately) not of the tails.

The ordering of the tails is important in (wet) electrochemical measurements where electrolyte may penetrate the thiol layer. With macroscopic

electrochemical measurements like cyclovoltammetry and differential capacitance measurements in an indifferent electrolyte with thiol–modified electrodes, information about the resistance of the thiol layer against penetration can be obtained. It was found that the dielectric constant, as determined from differential capacitance measurements, was low ($\varepsilon_r \approx 2$) and independent of the applied potential and the thiol chain length (provided $n > 10$). For short chains ($n \leq 10$), it was found that the monolayer is disordered. The penetration of water and ions like H^+ and K^+ in the ordered monolayers was shown to be largely blocked. The low capacitance and the strong resistance against ion penetration are due to the shielding of defects (like missing rows as found by STM) by the long alkane chains. Therefore, although defects may be present in air, they do not necessarily affect the (surface) properties of the thiol monolayer in an electrochemical environment. The combination of cyclovoltammetry, differential capacitance measurements and potential-dependent wetting measurements revealed that the structure of an alkanethiol monolayer is not affected when applying an electric field across the thiol layer, as long as only double layer currents flow. The stability of the monolayer is not affected when the thiol molecules are functionalized with small terminal groups like OH, COOH, CN or Cl. However, there are some indications that the orientation of these molecules changes when an electric field is applied across the layers.

According to the above measurements, the individual thiol layers behaved comparably. Nevertheless, the reproducibility of the cyclovoltammograms of galvanic metal deposition on top of the thiol layers was poor. We suggest that differences in the structure of the monolayer cause local differences in the potential drop across this layer and, consequently, in the overpotential. This makes cyclovoltammetry a very sensitive method for monitoring local microscopic differences in the structure of the monolayer. Analysis of the amount of gold in the thiol solution after immersion of the gold electrode also showed considerable scatter. The dissolved gold is released during an etching process related to thiol adsorption, leaving holes in the gold substrate.

Having obtained this structural information from macroscopic and microscopic measurements, we are now in the position to revisit the question stated in the

introduction of this thesis: are thiol layers suitable model systems? From the results of the electrochemical and wetting experiments in this thesis and from many other studies published in the literature, it may be safely concluded that self–assembled thiol monolayers are ordered and densely packed on the macroscopic scale. However, with atomically resolved STM in air and from galvanic metal deposition measurements, it was found that the local microscopic structure deviated. Hence, an unequivocal answer to the question cannot be given.

In our potential–dependent wetting measurements, the monolayer behaved highly ideal and the electrowetting effect could be described by a simple theoretical model. The monolayer is not perfect when used as a model system for studying the influence of the surface energy on galvanic metal deposition. Here, deviations in the local structure of the monolayer produce large differences in metallization behaviour, which makes the interpretation of these measurements rather complicated.

10.2. Suggestions for further research

It is often assumed that the preparation of high quality thiol monolayers is very simple. However, we found that even under strict control of the reaction conditions, the galvanic copper deposition on the individual samples showed considerable variations. Hence, there are some, as yet uncontrolled, parameters that influence the structure. A systematic investigation of the parameters affecting the structure of the monolayer, such as the temperature during and after adsorption, the solvent for the thiol, and the detailed structure of the gold substrate, would be useful to better control the structure of the monolayer. A simple method to test the quality of the monolayer is galvanic metal deposition on the monolayer.

The etching mechanism involved in the formation of holes in the top gold layer underneath the thiol monolayer needs to be verified in detail. In the mechanism

proposed in chapter 3, the holes were associated with the mobility of gold atoms, whereby we assumed that gold dissolves in the form of a gold–thiolate complex. The latter might be verified by analysing the thiol solution after adsorption with a technique like infrared spectroscopy. An understanding of the mechanism of the formation of such holes may give the possibility to minimize their occurrence, so that more perfect layers will be produced.

Furthermore, it is interesting to study the first stages of nucleation of galvanically deposited metal on a thiol monolayer in–situ using an electrochemical STM with atomic resolution. This would help to reveal the role of the defects in the molecular structure of the thiol layer in the nucleation process. If metal is preferentially deposited in such defects, this may offer interesting applications for the production of nanometer–sized patterns.

Summary

Self–assembled alkanethiol monolayers on gold are used as model systems in a fundamental study of the potential–dependent wetting and of the galvanic metal deposition. For using such monolayers as model systems, well–defined and ordered monolayers are required. In order to control the quality of the monolayer, its structure was studied on a microscopic and a macroscopic scale. The experimental methods were scanning tunneling microscopy (STM), wetting and electrochemical measurements. The chain length and the type of terminal group of the monolayer molecules were varied systematically.

The microscopic structure of monolayers of alkanethiol ($HS(CH_2)_{n-1}CH_3$ with n = 3, 8, 12, 18, and 22) on Au(111) is the subject of chapter 3. This structure is investigated with atomically resolved STM and wetting measurements. The characteristic depressions in these monolayers as observed with STM are proven to be holes in the underlying top gold surface layer. These depressions are filled with thiol. The holes originate from an etching process of the gold during the adsorption of the thiol. A distinct correlation is found between the number of holes and the amount of gold in the thiol solution after adsorption, as measured with atomic absorption spectroscopy. The etching which generates these holes is believed to be related to the mobility of the gold–thiolate molecules during the adsorption process, prior to self–assembly.

In chapter 4, the potential–dependent wetting of thiol–modified gold electrodes is for the first time presented. A Wilhelmy plate technique is used to determine the potential–dependent wetting of the modified electrodes. These measurements are carried out simultaneously with differential capacitance measurements and cyclovoltammetry. For alkanethiols with $n>10$, the monolayer is very stable in the potential range where only double layer charging occurs. The extreme hydrophobicity, the low dielectric constant (≈ 2 for $n>10$), and the low double layer current (about a factor of 100 less than for clean gold) are all indicative of the dielectric character of these monolayers.

Chapter 5 reports on the influence of the alkanethiol chain length on the electrowetting effect of the self-assembled monolayer. It is found that the shorter the chain the stronger the wettability changes as a function of the potential. A simple representation of the electrical double layer as a dielectric thiol layer in series with a diffuse double layer in the electrolyte accounts well for the observed chain length effect. The effect of the salt concentration can be qualitatively understood with the model. It is concluded that the potential–dependent wetting finds it origin in the formation of an electrical double layer and that potential–induced conformational changes within the thiol layer are insignificant.

Functionalizing the alkanethiols with a terminal group ($HS(CH_2)_{n-1}X$, X = OH, CN, Cl and COOH) is found not to affect the stability of the monolayer, as follows from chapter 6. All thiols used are electroinactive except for the COOH group which can in part (5–10%) be reduced to the aldehyde compound. The difference in the capacitance of these thiol layers is determined by the different dielectric properties of the terminal group. The capacitance increases according to the sequence $CH_3<Cl<OH<CN$. The potential in the electrocapillary maximum as determined from the electrowetting measurements also depends on the terminal group; this potential increases according to the sequence $CH_3<Cl<CN<OH$. There are some indications that the orientation of the molecules changes with applied potential for thiols with CN, OH, and Cl as terminal group.

Larger electrowetting effects are obtained by oxidation/reduction of a ferrocene–terminated alkanethiol monolayer, as described in chapter 7. Strong indications were found that the electrowettability is a result of specific anion binding upon oxidation of the ferrocene groups. This ion binding occurs to compensate the surface charge. The monolayers are not stable upon continuous oxidation/reduction of the ferrocene groups. The stability is strongly increased by mixing the ferrocenethiol with an alkanethiol of about the same chain length. The reversibility of the electrowetting is limited by contact angle hysteresis.

The presence of a self–assembled thiol monolayer on a gold electrode strongly

influences the morphology of galvanically deposited copper. This topic is discussed in chapter 8. On bare gold, copper is deposited as a rather homogeneous flat film, whereas on thiol–modified gold, independent of the type of terminal group, copper is deposited as hemispherical particles. The difference in morphology is ascribed to the difference between the surface energies of copper and the solid substrate. Generally, when a metal is deposited onto a solid material, flat films can only be obtained when the surface tension of the solid is high. Nucleation occurs on top of the thiol layer as long as the self–assembled monolayer is highly ordered. An overpotential is required to overcome the potential drop across the dielectric of the thiol layer. This potential drop increases with increasing thiol chain length and hence, the overpotential increases likewise. The influence of the terminal group of the thiol layer on galvanic copper deposition shows up most pronouncedly for the OH terminal group. About 100 times more particles are deposited on OH–terminated thiol compared to CH_3–thiol. This is explained by a combination of a smaller potential drop across the thiol layer and a high chemical affinity of Cu atoms for the OH–group, thus decreasing surface diffusion.

In the potential range between the equilibrium Nernst potential and the overpotential, no copper is deposited onto the monolayer. This makes the layers suitable as monolayer resists. In chapter 9 we focus on possible applications in this area. First, a thiol monolayer is treated by electron beam lithography to give very narrow patterns where the thiol has been removed. Subsequently, submicron metallized patterns can be produced by galvanic copper deposition in the openings. The smallest width of the copper patterns produced is about 75 nm. The width is determined by the spot size of the electron beam. By optimizing the electron exposure, we expect that even finer patterns can be produced. Such fine metal structures may offer interesting applications in technologies such as ultra–high–density recording or disk mastering.

This thesis concludes with an overview of this study and a comparison of our results with the current status of knowledge in the literature. In chapter 10, the information on the structure of the thiol monolayer as obtained with the various techniques is summarized. We conclude that methods like STM and metallization

indicate the presence of small microscopic defects in the self-assembled monolayers. However, with electrochemical techniques like cyclovoltammetry and differential capacitance measurements it was shown that on a macroscopic scale the monolayers are ordered and densely packed. From the macroscopic point of view, the minor defects are shielded by the long chain alkane tails. Therefore, we have to conclude that the question whether a thiol monolayer can be considered as a model system depends on the particular type of goal one has in mind. In this thesis, we have demonstrated that thiol monolayers behaved as genuine model systems in the areas of electrowetting and monolayer lithography.

Samenvatting

Heel dunne laagjes materiaal die zich op het oppervlak van een ander materiaal bevinden kunnen de oppervlakte-eigenschappen drastisch veranderen. Een dergelijk dun laagje hoeft niet dikker te zijn dan één miljoenste van een millimeter. Als het laagje slechts één molecule dik is, praten we over een monolaag. Monolagen spelen een rol in ons dagelijks bestaan, ook al realiseren de meeste mensen zich dat niet. Een voorbeeld: ruiten in huizen en auto's blijken na een wasbeurt goed te worden bevochtigd door water. Onder bevochtiging wordt verstaan dat een vloeistof, in dit geval water, spreidt over het oppervlak. Het oppervlak wordt hydrofiel genoemd (letterlijk, uit het Grieks: "waterminnend"), als het goed door water bevochtigd wordt. Echter, na verloop van tijd worden de ruiten meestal vanzelf weer vettig ofwel hydrofoob ("watervrezend") zodat het water niet meer over het oppervlak spreidt maar als druppeltjes blijft liggen of hangen. Het vettig worden van de ruit is een gevolg van het blijven kleven van vetachtige moleculen. Dit blijven kleven van moleculen aan een oppervlak heet adsorptie. Adsorptie kan plaatsvinden vanuit lucht, zoals in het voorbeeld van de ruiten, maar ook vanuit een vloeistof zoals in dit proefschrift het geval is. De mate van bevochtiging hangt onder andere af van de zogenaamde grensvlakspanning van het onderliggende materiaal, in dit geval de al dan niet vervuilde ruit. Hoe hoger de grensvlakspanning hoe beter de bevochtiging. Kennelijk verlagen vetmoleculen op een ruit de grensvlakspanning. Dit is een algemeen verschijnsel en zelfs een belangrijke natuurwet: door adsorptie wordt de grensvlakspanning lager. Ook vloeistoffen hebben een grensvlakspanning. Door deze grensvlakspanning kan bijvoorbeeld een schaatsenrijdertje (*Gerris lacustris*) op water "lopen" en blijft een eend drijven.

In dit onderzoek adsorberen we met een bedoeling en goed gecontroleerd een monolaag van thiolmoleculen op een goudoppervlak. Deze moleculen bevatten een zwavel–kopgroep die met goud een chemische binding vormt. Hun chemische formule kan geschreven worden als $HS(CH_2)_{n-1}CH_3$. We varieerden

de ketenlengte *n* van 3 tot 22. We hebben ook thiolen gebruikt, waarin de CH_3 groep vervangen is door *X*. Voor substituent *X* hebben we gekozen voor een hydroxyl– (OH), chloor– (Cl), cyanide– (CN) of carboxylgroep (COOH). Als thiolmoleculen in contact gebracht worden met goud, adsorberen ze spontaan en vormen daarbij onder bepaalde condities een geordende dichtgepakte monolaag. Dit proces heet "zelf–ordening" of in het Engels "self–assembly". Onze interesse in deze lagen komt voort uit het feit dat deze monolagen zeer stabiel zijn en daardoor geschikt zijn als modelsysteem in verschillende onderzoeken. Tevens zijn deze lagen interessant omdat slechts één monolaag nodig is om het goud te maskeren. De oppervlakte-eigenschappen van het bedekte goud, zoals de bevochtiging, worden nu volledig bepaald door de geadsorbeerde moleculen. Door de eindgroep *X* van het thiolmolecuul te variëren, kan een goed of een slecht bevochtigend oppervlak worden gemaakt.

In dit proefschrift zijn thiolmonolagen op goud gebruikt als een modelsysteem voor het bestuderen van *a*) het elektrisch beïnvloeden van de mate van bevochtiging (elektrobevochtiging) en *b*) het langs elektrolytische weg verkrijgen van een metaalafzetting (elektrodepositie). Op beide aspecten wordt hierna teruggekomen.

Om zelf–ordenende thiollagen als modelsysteem te kunnen gebruiken, is het noodzakelijk dat de lagen dichtgepakt en geordend zijn. Een zeer nauwkeurige microscopische techniek (STM), bevochtigingseigenschappen en elektrochemische metingen zijn in dit proefschrift gebruikt om te controleren of dit inderdaad het geval is. De informatie die uit de verschillende methodes verkregen wordt, is verschillend van aard. De techniek STM is door ons onder zeer uitzonderlijke condities gebruikt, waardoor voor het eerst groepen individuele moleculen waargenomen konden worden. Deze techniek verschaft dus informatie over de moleculaire structuur van de laag. De monolagen blijken een zeer regelmatig geordende structuur te hebben. Op sommige plaatsen op het oppervlak worden defecten in de monolaag waargenomen, zoals rijen ontbrekende moleculen. In het onderliggende goud kunnen gaten gezien worden. Deze zijn net zo diep als de dikte van één goudatoom en gevuld met thiol. Deze gaten blijken het gevolg te zijn van de etsende werking van thiol tijdens de

adsorptie: er lost een heel klein beetje goud op tijdens de adsorptie dat kan worden aangetoond in de thioloplossing van waaruit de monolaag is aangebracht. Kennelijk vinden er twee processen tegelijkertijd plaats: adsorptie en oplossen van het goudoppervlak.

Bevochtigingseigenschappen en elektrochemische metingen geven informatie over de macroscopische eigenschappen van de lagen maar geen direct inzicht in het gedrag van individuele moleculen. Bij de elektrochemische metingen bevindt het thiol-bedekte goud zich in een zoutoplossing die positieve en negatieve ionen bevat. Uit elektrochemische metingen blijkt dat de defecten in de monolaag zoals gevonden met STM bij deze "macroscopische" metingen nauwelijks een rol spelen: de ionen die in de oplossing aanwezig zijn, dringen de thiollaag niet binnen. De monolagen zijn macroscopisch gezien dichtgepakt en geordend.

De resultaten voor de structuur van de thiolmonolaag beschouwende, kunnen we dus concluderen dat op macroscopische schaal de monolaag dichtgepakt en geordend is, terwijl toch op moleculaire schaal defecten in de laag worden gevonden. Of een dergelijke thiollaag gebruikt kan worden als een geschikt modelsysteem hangt af van het beoogde doel. In ons geval zijn de monolagen zeer geschikt gebleken bij elektrobevochtiging en lithografie. Beide termen zullen hierna worden toegelicht.

Elektrobevochtiging aan geadsorbeerde monolagen wordt in dit proefschrift voor het eerst beschreven. Om deze elektrobevochtiging te kunnen meten is gebruik gemaakt van een goudplaatje bedekt met thiol. Het goudplaatje staat in contact met een zoutoplossing. Door de elektrische spanning te variëren verandert de bevochtiging van het thiol-bedekte goudplaatje door de zoutoplossing. We hebben de invloed van de thiolketenlengte, zoutconcentratie van de oplossing en eindgroep X van het thiol molecuul op de elektrobevochtiging bestudeerd. Om de metingen te interpreteren hebben we het effect beschreven met behulp van thermodynamische berekeningen. Er werd gevonden dat de gemeten en de berekende waarden goed overeenstemden.

Voor praktische toepassing van dit elektrobevochtigingseffect kan men

bijvoorbeeld denken aan het vullen en ledigen van smalle capillaire buisjes. Bij goede bevochtiging van de wanden van het capillair zal de vloeistof in het buisje opstijgen, bij slechte bevochtiging niet. Door met behulp van elektrisch spanningsverschillen de bevochtiging van de wand te sturen, kan men er voor zorgen dat vloeistof in het capillair stijgt of juist daalt. Op deze manier is al eens een soort micropompje gemaakt. Dit zou bijvoorbeeld gebruikt kunnen worden als koelsysteem in microelektronica.

Het tweede thema in dit proefschrift heeft betrekking op het langs elektrolytische weg afzetten van koper op met thiol bedekt goud. Hierbij hebben we de rol van het grensvlak thiol/zoutoplossing op de metallisatie bestudeerd. Voor industriële toepassingen worden meestal gladde en vlakke metaallagen vereist. Of dergelijke lagen inderdaad gevormd worden hangt onder andere af van de grensvlakspanning. In dit onderzoek hebben we de eindgroep X van het thiol (en daarmee de grensvlakspanning) gevarieerd en het metallisatiegedrag op zulke thiollagen op goud vergeleken met de metallisatie op een schoon goudoppervlak.

We hebben gevonden dat koper op schoon goud wordt afgezet als een vlakke homogene laag, terwijl koper op thiol–bedekt goud leidt tot afzetting van halfronde deeltjes. Dit gedrag hangt niet meetbaar af van de soort eindgroep. Dit verschil wordt toegeschreven aan een verschil in grensvlakspanning tussen het koper en het materiaal waarop het koper wordt afgezet. Alleen als de grensvlakspanning van dat materiaal hoog en vergelijkbaar met die van koper is, worden vlakke films gevormd.

Voor het afzetten van koper op het thiol blijkt een hogere elektrische spanning nodig te zijn dan op schoon goud. Hiervan hebben we gebruik gemaakt bij het maken van fijne metaalspoortjes. Dit is gedaan door met een elektronenbundel selectief thiolmoleculen uit een monolaag te verwijderen. Op deze plaatsen komt het onderliggende goud weer bloot te liggen. Vervolgens is koper elektrolytisch afgezet. Door de juiste elektrische spanning te kiezen wordt koper alleen afgezet in de openingen in de thiollaag. Deze manier van selectief metaal afzetten wordt lithografie genoemd. Er zijn zeer smalle spoortjes gemaakt met een breedte van

75 nanometer. Deze smalle metaalstructuren zijn potentieel uiterst interessant voor toepassingen bij het opslaan van informatie in zeer hoge dichtheden.

In dit onderzoek hebben we veel geleerd over thiolmonolagen op goud. Vele stukjes van de puzzel zijn samengevallen en we hebben een goed beeld gekregen van de eigenschappen van deze monolagen. Nu moet er nog hard gewerkt worden aan de industriële toepassingen voortvloeiend uit dit onderzoek.

$$\Delta F_d = \Delta\gamma_{SL}^{el} = -\iint C_t[d(E-E_e)]^2$$
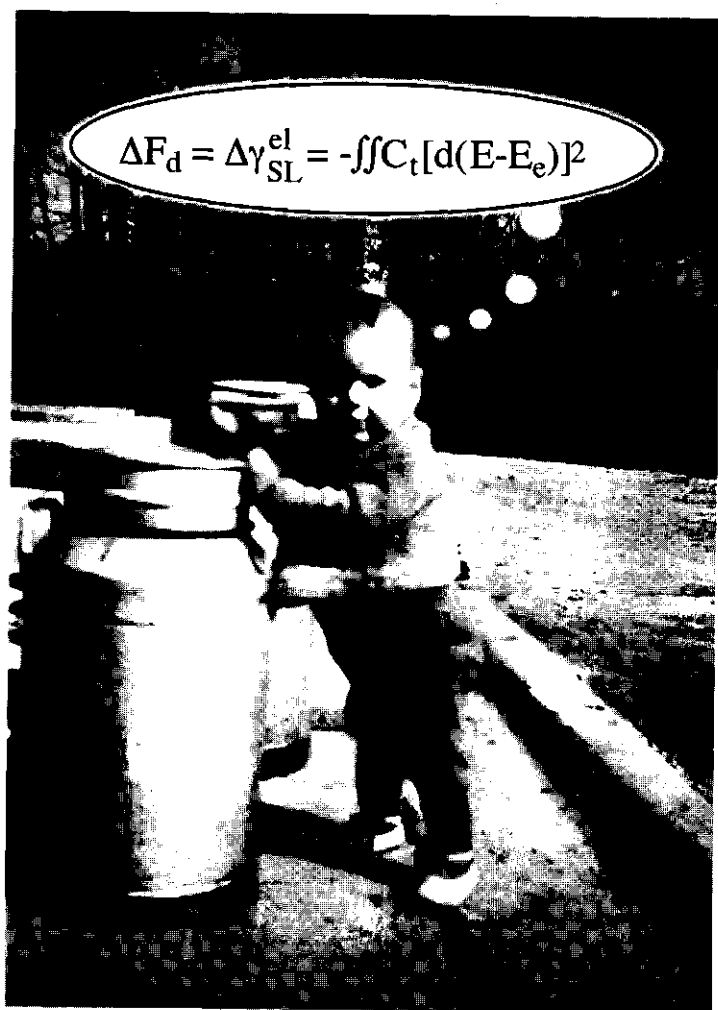
.....of hoe een boerendochter toch weer in de landbouw terechtkomt.

Levensloop

Jeannet Sondag-Huethorst werd geboren op 26 maart 1964 te Groenlo. In 1982 werd het VWO diploma behaald aan de r.k. scholengemeenschap het Marianum te Groenlo. In datzelfde jaar begon zij met een studie Chemische Technologie, differentiatie Produktkunde, aan de Hogere Technische School te Hengelo (O) en behaalde in 1986 het HTS diploma. In september 1986 kwam zij in dienst van het Philips Natuurkundig Laboratorium te Eindhoven op de afdeling Grensvlakchemie. In de daarop volgende jaren werden diverse opleidingen aan verschillende universiteiten en instellingen met goed gevolg afgesloten: college Colloïdchemie (1988) en college Oppervlaktechemie (1989) aan de Technische Universiteit Eindhoven en Philips Hogere Technische Opleiding "Vaste Stoffen" (1988). Verder werd deelgenomen aan de Summerschools "Technologically Important Aspects of Interface Science" (1989) aan het Imperial College te Londen en "Instrumental Methods in Electrochemistry" (1991) aan de universiteit van Southampton. Van 1986 tot en met 1990 was zij werkzaam in het vakgebied colloïdchemie en hield zich bezig met onderzoek naar verwijdering van submicrondeeltjes van vaste substraten, bevochtiging van deeltjes en Marangoni-drogen. Sinds 1991 is zij werkzaam in het vakgebied elektrochemie en hield zich bezig met het onderzoek dat leidde tot dit proefschrift.

Dankwoord

De tijd waarin dit werk tot stand is gekomen heb ik ervaren als een zeer leerzame en uitdagende maar vooral ook plezierige periode. Bijna vier jaar werken aan één onderwerp is bijna een unicum geworden in de industriële research. In deze vier jaar zagen we langzaam de stukjes van de thiol-puzzel in elkaar vallen wat uiteindelijk ook leidde tot een veelbelovende toepassing. Zonder hulp van vele mensen was dit allemaal niet gelukt. Hiervoor wil ik iedereen hartelijk bedanken!!!

De directie van het Nat. Lab. en Ties van Maaren bedank ik voor de kans die ze mij gegeven hebben om dit boeiende werk te doen en het te mogen vastleggen in een proefschrift. De vele faciliteiten die er op het lab. zijn hebben het mogelijk gemaakt het onderwerp vanuit vele invalshoeken te bestuderen. De werkplaatsen hebben geholpen bij het bouwen van de opstelling en het polijsten en opdampen van metalen. De groep Chemische Analyse heeft vele nauwkeurige analyses uitgevoerd. De glasinstrumentmakerij heeft glaswerk gemaakt en bewerkt. Chris Geenen heeft vele prachtige SEM-foto's gemaakt en Wilma Gijsbers heeft geholpen bij het polijsten en het maken van microscoopfoto's. Johan Lub voerde een aantal syntheses uit van speciale thiolen. De Audiovisuele Dienst maakte dit boekje tot een mooi boekje: Henny Alblas maakte alle tekeningen, Sam Bazelmans drukte de foto's af en Mieke Spaan, Henny Herps en Achil Janssen hielpen bij het in de juiste lay-out gieten van dit proefschrift. Alle mensen heel hartelijk dank.

Mijn collega's ben ik erkentelijk voor hun hulp, adviezen, vele discussies en de prettige werksfeer. Met name mijn kamergenotes en mijn oude en nieuwe maatjes wil ik hier bedanken. Ook wil ik de studentes Marice van Deurzen (die vrijwel alle metingen in hoofdstuk 8 heeft uitgevoerd) en Wendy van Ansem bedanken voor hun inbreng.

Daarnaast wil ik de mensen bedanken waarmee ik intensief heb samengewerkt: Henri van Helleputte voor de samenwerking op het gebied van e-beam